Nonlinear stochastic dynamics of detuned bladed-disks with uncertain mistuning and detuning optimization using a probabilistic machine learning tool

Evangéline Capiez-Lernout, Christian Soize

Nonlinear stochastic dynamics of detuned bladed-disks with uncertain mistuning and detuning optimization using a probabilistic machine learning tool

Evangéline Capiez-Lernout[a], Christian Soize[*,a]

[a] *Université Gustave Eiffel, MSME UMR 8208 CNRS, 5 bd Descartes, 77454 Marne-la-Vallée, France*

Abstract

The paper deals with the nonlinear stochastic dynamics concerning the detuning optimization in presence of random mistuning of bladed-disks with geometrical nonlinearities. We present an efficient computational methodology for reducing the computational cost, an analysis of the detuning, and the detuning optimization, based on the use of a high-fidelity computational model. A deep computational analysis is presented for a 12-bladed-disk structure that is representative of industrial turbomachines in order to understand the role played by the geometrical nonlinearities on the dynamical behavior and to exhibit the consequences on the detuning effects. For the detuning optimization with a very large number of possible detuned configurations, we propose a reformulation of the combinatorial optimization problem in a probabilistic framework, which is adapted to a probabilistic machine learning tool in order to limit the number of evaluations of the cost function with the high-fidelity computational model. The methodology proposed is validated for the 12-bladed-disk structure for which the exact optimal detuned configuration has been identified. A very good prediction is obtained.

Key words: nonlinear stochastic dynamics, bladed-disk, detuning, mistuning, reduced-order model, uncertainty quantification, combinatorial optimization, machine learning, probabilistic learning, PLoM

1. Introduction

The vibrational behavior of turbomachines is known to be particularly complex, requiring the construction of predictive computational models that have also to be efficient in terms of numerical costs. One of the issues concerns the mistuning caused by the small variations of the mechanical properties from one sector to another one, induced by the manufacturing tolerances or by the wear and tear of the structure. Such phenomenon can generate strong localization effects yielding larger dynamical amplifications of the forced response with respect to the perfect cyclic symmetry case [1, 2, 3]. This amplification strongly affects the fatigue life of the blades,

[*]Corresponding author: Christian Soize, christian.soize@univ-eiffel.fr

Email addresses: evangeline.capiez-lernout@univ-eiffel.fr (Evangéline Capiez-Lernout), christian.soize@univ-eiffel.fr (Christian Soize)

Preprint of the published paper in International Journal of Non-Linear Mechanics, 2022.

which can cause safety problems and impair the proper operation of turbomachines. Many research have been carried out on this subject, requiring the use of probabilistic approaches for modeling the random character of the mistuning combined to the construction of reduced-order models [4, 5, 6, 7, 8, 9, 10, 11] when linear assumption is considered. There also exist other phenomena that can strongly affect the vibrational behavior of the bladed-disk and that have to be the subject of a dedicated modeling. The presence of nonlinearities increases the complexity of the forced response analysis because couplings and energy transfers can strongly modify the position and the nature of the resonances of the bladed-disk. Contact nonlinearities occur for fan-type bladed-disks for which the disk and the blades are manufactured independently and for which the blade assembly is mounted on the disk with "fir-tree" or dovetail fixings. Such local nonlinearities although occur through rotor/stator interaction between the blade tip and the stator casing or when using under-platform dampers yielding blade to blade contact (see e.g. [12, 13, 14, 15, 16, 17, 18]). A research effort has also been made for the construction of nonlinear reduced-order models allowing for the mistuning analysis of bladed-disk in presence of contact nonlinearities [19, 20, 21, 22, 23, 24, 25]. Moreover, due to technological evolutions that involve lighter materials and thinner blades, the nonlinear geometrical effects induced by finite displacements cannot longer be neglected. The main difficulties concerning the modeling of these nonlinear geometrical effects concern the construction of adapted nonlinear reduced-order models that have to be efficient not only in terms of computational costs but also in terms of predictability. These aspects have also been investigated in the more general context of thin and slender structures [26, 27, 28, 29, 30, 31]. Concerning the context of turbomachines, various research can be found for the deterministic case [32, 33, 34], but also in presence of contact nonlinearities [35] or in presence of mistuning [36].

The intentional mistuning, also called detuning, consists in voluntarily breaking the cyclic symmetry of the structure by using partial or alternating patterns of different sector types. The detuning allows for spreading the frequencies of adjacent blades and thus for reducing the interaction between them. As a consequence, the drastic amplification and localization effects caused by the random mistuning can be greatly reduced. Such technology is particularly relevant because it is a way for reducing the response amplification levels that are induced by the unavoidable random mistuning while increasing its robustness. It has been thoroughly studied in the framework of linear dynamics [37, 38, 39, 40, 41, 42, 43, 44, 45, 46].

In a context of sustainable development, technological innovations have to be compatible with energy and environmental issues. This gives rise to the development and to the use of lighter materials, that have to be capable of high thermo-mechanical resistance and of long durability, so that it may be possible that the blade displacements respond in its nonlinear vibration range. In this context, a computational methodology and a robust analysis of the geometrical nonlinear effects on several detuned configurations of mistuned bladed-disk have been proposed in [47]. The results underline a complex nonlinear dynamical behavior and highlight a sensitivity of the nonlinear response to the detuning in presence of mistuning. Nevertheless, a too few number of detuned configurations is available and is not sufficient to perform a full optimization analysis with respect to the set of all possible detuned configurations of mistuned structures. This latter one has a huge dimension that increases exponentially with respect to the number of blades.

Novelties of the paper. The first novelty is the development of an efficient computational methodology in nonlinear stochastic dynamics for reducing the computational cost using a high-fidelity computational model (HFCM), and a deep computational analysis of a 12-bladed-disk structure that is representative of industrial turbomachines in order (i) to understand the role played by the

geometrical nonlinearities on the dynamical behavior and (ii) to construct the solution of the detuning optimization problem and to analyze the optimization results. For the case for which the set of all the possible detuned configurations cannot be computed with the HFCM, we propose a novel probabilistic approach consisting in estimating a small subset (a few units) of detuned configurations that improve the dynamical responses with respect to the configuration without detuning in presence of random mistuning. This approach is based on a probabilistic formulation of the combinatorial optimization problem and on the use of a probabilistic learning tool for estimating the cost function without using the HFCM.

Organization of the paper. Section 2 is devoted to the formulation, the methodology, the computational model, and the algorithms for the nonlinear stochastic dynamics analysis of rotating detuned bladed-disks with geometrical nonlinearity in presence of random mistuning. The chosen formulation is compatible with the use of the nonparametric probabilistic approach of uncertainties for modeling the random character of the mistuning. We describe in details the specific numerical difficulties encountered (i) in the computation of the nonlinear internal forces and its related tangent stiffness matrix, and (ii) in the use of the nonlinear solver. In Section 3, we present a full analysis of a representative computational model of the 12-bladed-disk structure and the analysis of the detuned configurations. All the numerical parameters involved in the computational process are carefully optimized in order to be able to generate a full data basis for constructing the exact solution of the detuning optimization problem. In Section 4, for the general case for which the number of detuned configurations is very large, we present a probabilistic formulation of the combinatorial optimization problem and a probabilistic learning tool for constructing a surrogate model of the cost function. This formulation is able to capture the amplification level of a detuned configuration of the mistuned structure with respect to the configuration without detuning in presence of random mistuning (pure mistuned configuration). The statistics post-processing of the computational results yields a small subset of optimized configurations whose characteristics are analyzed in details. The proposed approach is validated using the computational analysis performed in Section 3 for the 12-bladed-disk structure.

Notations

Lower-case letters such as q or η are deterministic real variables.
Boldface lower-case letters such as $\mathbf{q}$ or $\boldsymbol{\eta}$ are deterministic vectors.
Upper-case letters such as X or H are real-valued random variables.
Boldface upper-case letters such as $\mathbf{X}$ or $\mathbf{H}$ are vector-valued random variables.
Lower-case letters between brackets such as $[x]$ or $[\eta]$ are deterministic matrices.
Boldface upper-case letters between brackets such as $[\mathbf{X}]$ or $[\mathbf{H}]$ are matrix-valued random variables.

δ_K: hyperparameter controlling the mistuning rate.
δu: displacement field $\mathbf{x} \mapsto \delta u(\mathbf{x})$.
$\delta_{\alpha\beta}$: Kronecker's symbol.
f_{HFCM}: mapping on $\mathcal{N}_c$ defined by HFCM.
$\imath$: imaginary unit such that $\imath^2 = -1$.
n: number of dof in the computational model.
nb_1: number of blades of type 1.
nb_2: number of blades of type 2.

n_c: number of all the possible configurations.
n_{sim}: number of Monte Carlo realizations.
n_w: number of blades.
q^c: amplification dynamic factor (QoI).
$q^{c,\ell}$: Qoi computed with HFCM from $\mathbf{w}^{c,\ell}$.
q^{ℓ}_{ar}: learned realization of Q.
$\mathbf{u}$: vector of the M generalized coordinates.
w^c_j: component j of $\mathbf{w}^c$ for blade number j.
$\mathbf{w}^c$: vector in $\mathcal{N}_c$ defining a configuration.
$w^{c,\ell}_j$: = 0 if j of type 1, = 1 if j of type 2.
$\mathbf{w}^{c,\ell}$: $\mathcal{N}_c$-valued vector of C_c(given configuration).
$\mathbf{w}^{\ell}_{\text{ar}}$: learned realization of $\mathbf{W}$.
$\mathbf{w}^{\text{opt}}$: optimal solution.
$\mathbf{w}^{c,\text{opt}}_{\text{un}}$: unachievable optimal solution.
$\mathbf{x} = (x_1, x_2, x_3)$: point in $\mathbb{R}^3$.
$\mathbb{x}(t)$: displacement field at time t.
C_c: discrete set of all the $n_c = 216$ configurations.
C_{ad}: admissible set of displacement fields.
$\mathbb{C}$: set of all the complex numbers.
$\mathbb{C}^n$: Hermitian vector space on $\mathbb{C}$ of dimension n.
$\mathcal{D}_d$: training set made up of N_d points $(q^{c,\ell}, \mathbf{w}^{c,\ell})$.
$\mathcal{D}_{\text{ar}}$: learned set made up of N_{ar} points $(q^{\ell}_{\text{ar}}, \mathbf{w}^{\ell}_{\text{ar}})$.
E: mathematical expectation.
$[I_n]$: identity matrix in $\mathbb{M}_n$.
J_c: cost function derived from $\mathcal{J}_c$.
J_{ar}: learned cost function.
$\mathcal{J}_c$: cost function.
M: order of the reduced-order model.
$\mathbb{M}_{n,N}$: set of $(n \times N)$ real matrices.
$\mathbb{M}_N$: set of square $(n \times n)$ real matrices.
$\mathbb{M}^{+0}_n$: set of positive symmetric $(n \times n)$ real matrices.
$\mathbb{M}^{+}_n$: set positive-definite symmetric $(n \times n)$ matrices.
N: order of the blisk equal to n_w.
N_{ar}: number of points in the learned set.
N_d: number of points in the training set.
$\mathcal{N}_c$: discrete set $\{0, 1\}^{n_w}$.
$\mathbb{N}$: set of all the integers.
Q: random QoI constructed with PLoM.
Q^c: random QoI such that $Q_c = f_{\text{HFCM}}(\mathbf{W}^c)$.
Q: dimension of matrix $[\mathbf{G}(\delta_K)]$.
$\mathbb{R}$: set of all the real numbers.
$\mathbb{R}^n$: Euclidean vector space on $\mathbb{R}$ of dimension n.
$\mathbf{U}(t)$: $\mathbf{u}(t)$ in the finite element approximation.
$\mathbf{U}^{\ell}$(t): $\mathbf{U}(t)$ for detuned configuration ℓ.
$\mathbf{W}$: $\mathbb{R}^{n_w}$-valued random variable associated with $\mathbf{W}^c$.
W^c_k component k of $\mathbf{W}^c$.

$\mathbf{W}^c$: random variable with values in $\mathcal{N}_c$.
$\mathcal{W}_{n_s}^{\text{opt}}$: subset of optimal solutions.
$\mathbb{X}(t)$: finite element discretization of $\mathbb{x}(t)$.
$\mathbb{X}^\ell(t)$: $\mathbb{X}(t)$ for detuned configuration ℓ.
$[x]_{kj}$: entry of matrix $[x]$.
$[x]^T$: transpose of matrix $[x]$.
$<\mathbf{x}\,,\mathbf{y}>$: Euclidean or Hermitian inner product.
$\|\mathbf{x}\|$: Euclidean or Hermitian norm $<\mathbf{x}\,,\mathbf{x}>^{1/2}$.
blisk: turbomachine component comprising both rotor disk and blades.
dof: degree of freedom.
pdf: probability density function.
ANN: artificial neural network.
FFT: Fast Fourier Transform.
HFCM: high-fidelity computational model.
KDE: kernel density estimation.
MCMC: Markov chain Monte Carlo.
NL-ROM: nonlinear reduced-order model.
NL-SROM: nonlinear stochastic reduced-order model.
PCA: principal component analysis.
PLoM: probabilistic learning on manifolds.
QoI: quantity of interest.
ROB: reduced-order diffusion-maps basis.

2. Stochastic computational model for dynamic analysis of rotating bladed-disks with geometrical nonlinearities: formulation, methodology, and algorithms

2.1. Assumptions

In the present work, the detuned bladed-disk structure has N blades and is assumed (1) to be made up of a linear elastic material, (2) to be submitted to external forces whose amplitude is sufficiently large so that the structure undergoes geometrical nonlinear effects induced by large displacement, (3) to rotate at a constant velocity Ω around the rotation axis defined by $(0, \mathbf{Z})$, (4) to be constituted of different types of blades whose spatial distribution characterizes a detuned configuration. In this work, two different sector types are considered. These two types have an identical geometry but the blades have different material properties.

We have then to distinguish the tuned configuration from the detuned configurations. The tuned structure is related to the conceptual structure that has a perfect N-order cyclic symmetry. In consequence, the geometrical domain, the constitutive equations and the boundary conditions related to the generating sector are invariant under the $2\pi/N$ rotation around the symmetry axis $(0, \mathbf{Z})$. A detuned configuration corresponds to a modification of the tuned structure for which there is a spatial distribution of different types of sectors. For instance, if $N = 12$ and if there are two different types of sectors A or B, a pattern denoted by $3A4B3A2B$ is constituted of 3 consecutive blades with type A, 4 with type B, 3 with type A and 2 with type B. The tuned configuration can also be viewed as a particular detuning case. It should be also noted that detuned configurations can also be sub-cyclic which means that they present a cyclic symmetry with order $\mathbb{n} < N$, where $\mathbb{n}$ is a divisor of N. All these detuned configurations are characterized by the superscript ℓ.

The real systems that are related to these detuned structures are modeled by introducing mistuning (unintentional mistuning) that is modeled by using the nonparametric probabilistic approach of uncertainties [48, 49]. We then can distinguish the pure mistuning situation, from which the conceptual system is modeled with the tuned structure from the detuned structures that are considered in presence of mistuning.

2.2. Description of the geometric nonlinear boundary value problem of a detuned configuration

The superscript ℓ is omitted in this Section. Let $\mathbf{\Omega}$ be the three-dimensional bounded domain of the physical space $\mathbb{R}^3$ corresponding to the steady configuration of a detuned structure observed in the rotating frame that is defined as the reference configuration of the boundary value problem [50]. The boundary $\partial\mathbf{\Omega}$ is such that $\partial\mathbf{\Omega} = \mathbf{\Gamma_0} \cup \mathbf{\Gamma_E}$ with $\mathbf{\Gamma_0} \cap \mathbf{\Gamma_E} = \emptyset$ and the external unit normal to boundary $\partial\mathbf{\Omega}$ is denoted by $\mathbf{n} = (n_1, n_2, n_3)$ (see Fig. 1). The boundary part $\mathbf{\Gamma_0}$ corresponds to the fixed part (in the rotating frame) of the structure whereas the boundary part $\mathbf{\Gamma_E}$ is submitted to an external surface force field. A total Lagrangian formulation is chosen. Consequently, the mechanical equations are written with respect to the reference configuration in the rotating frame. Let $\mathbf{x} = (x_1, x_2, x_3)$ be the position of a point belonging to domain $\mathbf{\Omega}$. The displacement field expressed with respect to the reference configuration is denoted as $\mathbb{x}(\mathbf{x}, t) = (\mathbb{x}_1(\mathbf{x}, t), \mathbb{x}_2(\mathbf{x}, t), \mathbb{x}_3(\mathbf{x}, t))$. It should be noted that the surface force field $\mathbf{G}(\mathbf{x}, t)) = (G_1(\mathbf{x}, t)), G_2(\mathbf{x}, t)), G_3(\mathbf{x}, t))$ acting on boundary $\mathbf{\Gamma_E}$ and the body force field $\mathbf{g}(\mathbf{x}, t)) = (g_1(\mathbf{x}, t)), g_2(\mathbf{x}, t)), g_3(\mathbf{x}, t))$ acting on domain $\mathbf{\Omega}$ correspond to the Lagrangian transport into the reference configuration of the physical surface force field and to the physical body force field applied on the deformed configuration. The nonlinear boundary value problem is written,

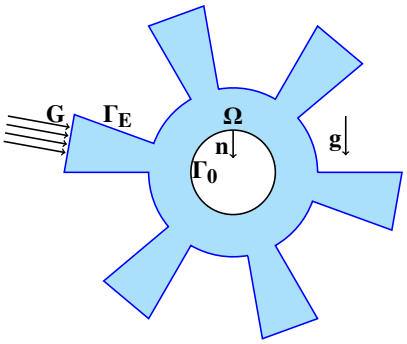

Figure 1: Reference configuration

for $i = 1, 2, 3$ and using the classical convention for summations over repeated indices, as

$$\rho \frac{\partial^2 \mathbb{x}_i}{\partial t^2} + 2\rho\, r_{ik} \frac{\partial \mathbb{x}_k}{\partial t} + \rho\, r_{ik}\, r_{k\ell}(x_\ell + \mathbb{x}_\ell) = \frac{\partial \left(F_{ij} S_{jk}\right)}{\partial x_k} + g_i(t) \quad \text{in} \quad \mathbf{\Omega}\,, \tag{1}$$

$$\mathbb{x}_i = 0 \quad \text{on} \quad \mathbf{\Gamma_0}\,, \tag{2}$$

$$F_{ij} S_{jk} n_k = G_i(t) \quad \text{on} \quad \mathbf{\Gamma_E}\,, \tag{3}$$

in which $\rho > 0$ is the mass density expressed in the reference configuration, where the (3×3) matrix $[\mathbf{r}(\Omega)]$ whose component $[\mathbf{r}(\Omega)]_{ij}$ is denoted as r_{ij} for the sake of clarity, is such that

$$[\mathbf{r}(\Omega)]_{ij} = r_{ij} = -\Omega\, \varepsilon_{ij3}\,, \tag{4}$$

where ε_{ijk} is the Levi-Civita symbol such that $\varepsilon_{ijk} = \pm 1$ for an even or odd permutation and $\varepsilon_{ijk} = 0$ otherwise. In Eq. (17), $\{F_{ij}\}_{ij}$ is the deformation gradient tensor whose components F_{ij} are defined by

$$F_{ij} = \mathbb{x}_{i,j} + \delta_{ij}\,, \tag{5}$$

in which δ_{ij} is the Kronecker symbol such that $\delta_{ij} = 1$ if $i = j$ and $\delta_{ij} = 0$ otherwise. In Eq. (5), $\mathbb{x}_{i,j}$ denotes the partial derivative $\partial \mathbb{x}_i / \partial x_j$. For a linear elastic material, the second Piola-Kirchoff symmetric stress tensor $\{S_{ij}\}_{ij}$ is written as

$$S_{ij} = \sigma^{(g)}_{ij} + a_{ijk\ell}\, E_{k\ell}\,, \tag{6}$$

in which $\{\sigma^{(g)}_{ij}\}_{ij}$ is the symmetric Cauchy stress tensor acting on the reference configuration observed in the rotating frame. In Eq. (6), the fourth-order elasticity tensor $\{a_{ijk\ell}\}_{ijk\ell}$ satisfies the usual symmetry and positive-definiteness properties. The Green strain tensor $\{E_{ij}\}_{ij}$ is written as the sum of linear and nonlinear terms such that

$$E_{ij} = \varepsilon_{ij} + \eta_{ij}\,, \tag{7}$$

in which $\varepsilon_{ij} = (\mathbb{x}_{i,j} + \mathbb{x}_{j,i})/2$ and where $\eta_{ij} = \mathbb{x}_{s,i}\,\mathbb{x}_{s,j}/2$. In the following, when no confusion is possible, symbol t denoting time is removed from the equations. Note that the first and the second partial derivatives of the displacement field with respect to t are denoted by $\dot{\mathbb{x}}$ and $\ddot{\mathbb{x}}$. In the rotating frame, we define the admissible space C_{ad} of the displacements as the set of all the sufficiently differentiable functions $\mathbf{x} \mapsto \delta\mathbb{x}(\mathbf{x})$ from $\mathbf{\Omega}$ in $\mathbb{R}^3$ such that $\delta\mathbb{x} = 0$ on $\mathbf{\Gamma_0}$ (in the rotating frame). For all fixed t, the weak formulation of the geometric nonlinear boundary value problem consists in finding the unknown displacement field $\mathbb{x}(t)$ in C_{ad} such that, for all $\delta\mathbb{x}$ in C_{ad},

$$m(\ddot{\mathbb{x}}, \delta\mathbb{x}) + \big(c(\dot{\mathbb{x}}, \delta\mathbb{x}) + d(\dot{\mathbb{x}}, \delta\mathbb{x})\big) + k^{(1)}(\mathbb{x}, \delta\mathbb{x}) + k^{(2)}(\mathbb{x}, \mathbb{x}, \delta\mathbb{x}) + k^{(3)}(\mathbb{x}, \mathbb{x}, \mathbb{x}, \delta\mathbb{x}) = f(\delta\mathbb{x})\,, \tag{8}$$

in which

$$f(\delta\mathbb{x}) = \int_{\mathbf{\Omega}} \delta\mathbb{x}_i\, g_i\, d\mathbf{x} + \int_{\mathbf{\Gamma_E}} \delta\mathbb{x}_i\, G_i\, ds\,, \tag{9}$$

with ds the surface element and where

$$m(\mathbb{x}, \delta\mathbb{x}) = \int_{\mathbf{\Omega}} \rho\, \mathbb{x}_i \delta\mathbb{x}_i\, d\mathbf{x}\ ,\ \ m(\mathbb{x}, \mathbb{x}) > 0\,, \tag{10}$$

$$c(\mathbb{x}, \delta\mathbb{x}) = \int_{\mathbf{\Omega}} 2\,\rho\, r_{ij} \mathbb{x}_j\, \delta\mathbb{x}_i\, \mathrm{d}\mathbf{x}\ ,\ \ c(\mathbb{x}, \mathbb{x}) = 0\,. \tag{11}$$

The bilinear form $k^{(1)}$ is written as

$$k^{(1)}(\mathbb{x}, \delta\mathbb{x}) = k^{(e)}(\mathbb{x}, \delta\mathbb{x}) + k^{(c)}(\mathbb{x}, \delta\mathbb{x}) + k^{(g)}(\mathbb{x}, \delta\mathbb{x})\,,$$

in which the positive-definite bilinear form $k^{(e)}$, the negative-definite bilinear form $k^{(c)}$, and the bilinear form $k^{(g)}$ are written as

$$k^{(e)}(\mathbb{x}, \delta\mathbb{x}) = \int_{\mathbf{\Omega}} a_{jk\ell m}\, \varepsilon_{\ell m}(\mathbb{x})\, \varepsilon_{jk}(\delta\mathbb{x})\, d\mathbf{x}\,, \tag{12}$$

$$k^{(c)}(\mathbb{x},\delta\mathbb{x}) = \int_{\Omega} \rho\, r_{ik}\, r_{k\ell}\, \mathbb{x}_{\ell}\, \delta\mathbb{x}_i \, d\mathbf{x}\,, \tag{13}$$

$$k^{(g)}(\mathbb{x},\delta\mathbb{x}) = \int_{\Omega} \sigma^{(g)}_{ij}\, \mathbb{x}_{s,i}\, \delta\mathbb{x}_{s,j} \, d\mathbf{x}\,, \tag{14}$$

The multilinear forms $k^{(2)}$ and $k^{(3)}$ are such that

$$k^{(2)}(\mathbb{x},\mathbb{x},\delta\mathbb{x}) = \int_{\Omega} a_{jk\ell m}\eta_{\ell m}(\mathbb{x})\varepsilon_{jk}(\delta\mathbb{x})\, d\mathbf{x} + \int_{\Omega} a_{jk\ell m}\mathbb{x}_{s,j}\delta\mathbb{x}_{s,k}\varepsilon_{\ell m}(\mathbb{x}) d\mathbf{x}\,, \tag{15}$$

$$k^{(3)}(\mathbb{x},\mathbb{x},\mathbb{x},\delta\mathbb{x}) = \int_{\Omega} a_{jk\ell m}\mathbb{x}_{s,j}\, \delta\mathbb{x}_{s,k}\, \eta_{\ell m}(\mathbb{x})\, d\mathbf{x}. \tag{16}$$

In Eq. (8), the damping bilinear form is modeled with a Rayleigh model such that

$$d(\mathbb{x},\delta\mathbb{x}) = \mathbb{\alpha}\, m(\mathbb{x},\delta\mathbb{x}) + \mathbb{\beta}\, k^{(1)}(\mathbb{x},\delta\mathbb{x})\,, \tag{17}$$

in which $\mathbb{\alpha}$ and $\mathbb{\beta}$ are two given positive or zero real numbers, not equal to zero simultaneously. The multilinear form $k^{(2)}(\mathbb{x},\mathbb{x},\delta\mathbb{x})$ can be written as

$$k^{(2)}(\mathbb{x},\mathbb{x},\delta\mathbb{x}) = \frac{1}{2}(\widehat{k}^{(2)}(\mathbb{x},\mathbb{x},\delta\mathbb{x}) + \widehat{k}^{(2)}(\mathbb{x},\delta\mathbb{x},\mathbb{x}) + \widehat{k}^{(2)}(\delta\mathbb{x},\mathbb{x},\mathbb{x}))\,, \tag{18}$$

in which the multilinear form $\widehat{k}^{(2)}$ is defined by

$$\widehat{k}^{(2)}(\mathbb{x},\delta\mathbb{x},\mathbb{z}) = \int_{\Omega} a_{jk\ell m}\, \mathbb{x}_{s,\ell}\, \delta\mathbb{x}_{s,m}\, \mathbb{z}_{j,k}\, d\mathbf{x}\,, \tag{19}$$

and satisfies the following symmetry property, $\widehat{k}^{(2)}(\mathbb{x},\delta\mathbb{x},\mathbb{z}) = \widehat{k}^{(2)}(\delta\mathbb{x},\mathbb{x},\mathbb{z})$ for all $\mathbb{z}$ in C_{ad}. Finally, using the symmetry and the positive-definiteness property of elasticity tensor $\mathbb{c}$ allows for rewriting the multilinear form $k^{(3)}(\mathbb{x},\delta\mathbb{x},\mathbb{z},\delta\mathbb{z})$ as

$$k^{(3)}(\mathbb{x},\delta\mathbb{x},\mathbb{z},\delta\mathbb{z}) = \frac{1}{2}\int_{\Omega} a_{jk\ell m}\, \mathbb{x}_{\alpha,\ell}\, \delta\mathbb{x}_{\alpha,m}\, \mathbb{z}_{\beta,j}\, \delta\mathbb{z}_{\beta,k}\, d\mathbf{x}\,, \tag{20}$$

which shows that $k^{(3)}(\mathbb{x},\delta\mathbb{x},\mathbb{x},\delta\mathbb{x}) > 0$.

2.3. Construction of the NL-ROM related to a detuned configuration

The computational model is constructed by discretizing Eq. (8) by the finite element method and is referred as the high-fidelity computational model (HFCM). Such a nonlinear computational model is not explicitly constructed because of the large number of degrees of freedom occurring in industrial finite element models. This Section is devoted to the construction of the nonlinear reduced-order model (NL-ROM) of a detuned configuration without mistuning of the rotating structure. The superscript ℓ characterizing the detuned configuration is omitted for clarity.

Let $\{\boldsymbol{\varphi}^1,\ldots,\boldsymbol{\varphi}^M\}$ be a given finite family of algebraically independent vectors in C_{ad}. We introduce the notation $\mathcal{A}_{\alpha\beta} = a(\boldsymbol{\varphi}^{\beta},\boldsymbol{\varphi}^{\alpha})$ in which $a(\mathbb{x},\delta\mathbb{x})$ is one of the bilinear forms defined by Eqs. (10) to (14). Similarly, we introduce the notations $\mathcal{K}^{(2)}_{\alpha\beta\gamma} = k^{(2)}(\boldsymbol{\varphi}^{\gamma},\boldsymbol{\varphi}^{\beta},\boldsymbol{\varphi}^{\alpha})$, $\widehat{\mathcal{K}}^{(2)}_{\alpha\beta\gamma} = \widehat{k}^{(2)}(\boldsymbol{\varphi}^{\gamma},\boldsymbol{\varphi}^{\beta},\boldsymbol{\varphi}^{\alpha})$, $\mathcal{K}^{(3)}_{\alpha\beta\gamma\delta} = k^{(3)}(\boldsymbol{\varphi}^{\delta},\boldsymbol{\varphi}^{\gamma},\boldsymbol{\varphi}^{\beta},\boldsymbol{\varphi}^{\alpha})$, and $\mathcal{F}_{\alpha} = f(\boldsymbol{\varphi}^{\alpha})$. We define the vector $\mathbf{u} = (u_1,\ldots,u_M)$

of the generalized coordinates as a new set of unknowns obtained by projecting the reference nonlinear response $\mathbb{x}(\mathbf{x},t)$ on the vector space spanned by the finite family $\{\boldsymbol{\varphi}^1,\ldots,\boldsymbol{\varphi}^M\}$,

$$\mathbb{x}(\mathbf{x},t) \;=\; \sum_{\beta=1}^{M} \boldsymbol{\varphi}^{\beta}(\mathbf{x})\, u_{\beta}(t)\,. \tag{21}$$

Let $\delta\mathbb{x}(\mathbf{x}) = \boldsymbol{\varphi}^{\alpha}(\mathbf{x})$ be a test function in C_{ad}. Substituting $\mathbb{x}(\mathbf{x},t)$ and $\delta\mathbb{x}(\mathbf{x})$ into Eq. (8), and using Eqs. (9) to (20) yields the following set of M nonlinear coupled differential equations such that, for $\alpha \in \{1,\ldots,M\}$,

$$\mathcal{M}_{\alpha\beta}\,\ddot{u}_{\beta} + (\mathcal{C}_{\alpha\beta} + \mathcal{D}_{\alpha\beta})\,\dot{u}_{\beta} + (\mathcal{K}^{(e)}_{\alpha\beta} + \mathcal{K}^{(c)}_{\alpha\beta} + \mathcal{K}^{(g)}_{\alpha\beta})\,u_{\beta} + \mathcal{F}^{\text{NL}}_{\alpha}(\mathbf{u}) = \mathcal{F}_{\alpha}\,, \tag{22}$$

in which $\boldsymbol{\mathcal{F}}^{\text{NL}}(\mathbf{u}) = (\mathcal{F}^{\text{NL}}_1(\mathbf{u}),\ldots,\mathcal{F}^{\text{NL}}_M(\mathbf{u}))$ is the $\mathbb{R}^M$-vector of the reduced nonlinear internal forces whose component α is written as

$$\mathcal{F}^{\text{NL}}_{\alpha}(\mathbf{u}) = \mathcal{K}^{(2)}_{\alpha\beta\gamma}\,u_{\beta}\,u_{\gamma} + \mathcal{K}^{(3)}_{\alpha\beta\gamma\delta}\,u_{\beta}\,u_{\gamma}\,u_{\delta}\,, \tag{23}$$

in which

$$\mathcal{K}^{(2)}_{\alpha\beta\gamma} \;=\; \frac{1}{2}\Big(\widehat{\mathcal{K}}^{(2)}_{\alpha\beta\gamma} + \widehat{\mathcal{K}}^{(2)}_{\beta\gamma\alpha} + \widehat{\mathcal{K}}^{(2)}_{\gamma\alpha\beta}\Big)\,, \tag{24}$$

and where $\boldsymbol{\mathcal{F}} = (\mathcal{F}_1,\ldots,\mathcal{F}_M)$ is the $\mathbb{R}^M$-vector of the reduced external forces whose component α is $\mathcal{F}_{\alpha} = f(\boldsymbol{\varphi}^{\alpha})$. The computational procedure concerning the computation of $\boldsymbol{\mathcal{F}}^{\text{NL}}(\mathbf{u})$ requires to use the finite element method in order (1) to construct the quadratic stiffness contribution $\widehat{\mathcal{K}}^{(2)}_{\alpha\beta\gamma}$, to retrieve the quadratic stiffness contribution $\mathcal{K}^{(2)}_{\alpha\beta\gamma}$ according to Eq.(24), to construct the cubic stiffness contribution $\mathcal{K}^{(3)}_{\alpha\beta\gamma\delta}$ and to compute the vector of the nonlinear reduced internal forces $\boldsymbol{\mathcal{F}}^{\text{NL}}(\mathbf{u})$. The choice of such computational procedure is required by the choice of modeling the mistuning phenomenon through the nonparametric probabilistic approach [51]. All the details concerning the computation of the nonlinear internal reduced force vector can be found in [52].

The projection basis can be constructed as the linear elastic modes of the rotating structure associated with its first eigenfrequencies ordered in ascending order. It should be noted that in the case of a rotating structure, the generalized eigenvalue problem allowing such a computation is a nonsymmetric eigenvalue problem yielding a complex projection basis, due to the presence of the gyroscopic coupling term. Another projection basis can be chosen as the family of linear elastic modes constructed without considering the gyroscopic coupling term. With such a choice, the speed of convergence with respect to M of the projection remains fast enough for bladed-disks whose blades have a reasonable slenderness. When the gyroscopic coupling term is kept, an alternative method avoiding the calculation of complex modes can be used as proposed in [47]. It consists in using the proper orthogonal decomposition method (POD) applied to the nonlinear dynamical response of the rotating structure (including all the coupling terms) issued from a first nonlinear reduced-order model obtained with the linear elastic modes calculated without the gyroscopic coupling term.

Let n be the number of dofs of the HFCM. Let $[\Phi]$ be the $(n \times M)$ matrix whose columns are the vector of the projection basis (in the finite element discretization). At time t, the physical response of the detuned bladed-disk, constructed using the HFCM, is written as

$$\mathbb{X}(t) = [\Phi]\,\mathbf{U}(t)\,, \tag{25}$$

in which $\mathbb{X}(t)$ is the $\mathbb{R}^n$-vector of the physical displacements and $\mathbf{U}(t)$ is the $\mathbb{R}^M$ vectors of the generalized coordinates $U_1(t),\ldots,U_M(t)$.

2.4. Construction of the NL-SROM related to a detuned configuration in presence of mistuning

In this paragraph, we are interested in constructing the nonlinear stochastic reduced-order model (NL-SROM) related to a detuned configuration of the bladed-disk in presence of random mistuning. It is assumed that the mistuning only affects the linear elastic internal force and the nonlinear forces, which are therefore uncertain. Such mistuning is modeled through the nonparametric probabilistic approach [49] for geometric nonlinearities [51], which is briefly summarized below. A global stiffness ($P\times P$) real symmetric matrix $[\mathcal{K}^{\rm NL}]$, with $P = M(M+1)$, containing all the linear, quadratic, and cubic elastic stiffness contributions, is constructed such that

$$[\mathcal{K}^{\rm NL}] = \begin{bmatrix} [\mathcal{K}^{(e)}] & [\widehat{\mathcal{K}}^{(2)}] \\ [\widehat{\mathcal{K}}^{(2)}]^T & 2\,[\mathcal{K}^{(3)}] \end{bmatrix}, \tag{26}$$

in which $[\mathcal{K}^{(e)}]$ is the $(M\times M)$ matrix defined by $[\mathcal{K}^{(e)}]_{\alpha\beta} = \mathcal{K}^{(e)}_{\alpha\beta}$ and where the block matrices $[\widehat{\mathcal{K}}^{(2)}]$ and $[\mathcal{K}^{(3)}]$ are the $(M\times M^2)$ and the $(M^2\times M^2)$ real matrices resulting from the following reshaping operation,

$$[\widehat{\mathcal{K}}^{(2)}]_{\alpha J} = \widehat{\mathcal{K}}^{(2)}_{\alpha\beta\gamma}\,,\; J = (\beta-1)M+\gamma\,, \tag{27}$$

$$[\mathcal{K}^{(3)}]_{IJ} = \mathcal{K}^{(3)}_{\alpha\beta\gamma\delta}\,,\; I = (\alpha-1)M+\beta\,,\; J = (\gamma-1)M+\delta\,. \tag{28}$$

In [51], it is proven that $[\mathcal{K}^{\rm NL}]$ is a positive-definite matrix that is modeled by a random matrix $[\boldsymbol{\mathcal{K}}^{\rm NL}]$. In this work, we use the nonparametric probabilistic modeling proposed in [53] for random matrix $[\boldsymbol{\mathcal{K}}^{\rm NL}]$,

$$[\boldsymbol{\mathcal{K}}^{\rm NL}] = [L_K]^T\,[\mathbf{G}(\delta_K)]\,[L_K] + [\Delta\mathcal{K}] \text{with} \quad [\Delta\mathcal{K}] = [\mathcal{K}^{\rm NL}] - [L_K]^T\,[L_K]\,. \tag{29}$$

The matrix $[L_K]$ is a full $(\mathrm{Q}\times P)$ matrix for which $\mathrm{Q} \ll P$, defined by $[L_K] = [\Lambda^{\mathrm{Q}}]^{\frac{1}{2}}\,[\Psi^{\mathrm{Q}}]^T$. The columns of $[\Psi^{\mathrm{Q}}]$ are the Q eigenvectors of matrix $[\mathcal{K}^{\rm NL}]$ related to its first Q largest eigenvalues that are stored in the diagonal matrix $[\Lambda^{\mathrm{Q}}]$. The full $(\mathrm{Q}\times\mathrm{Q})$ random matrix $[\mathbf{G}(\delta_K)]$ is then constructed according to the nonparametric probabilistic approach [54, 49] for which the uncertainty level is controlled by a scalar hyperparameter δ_K. The random matrix $[\boldsymbol{\mathcal{K}}^{\rm NL}]$ is block-decomposed similarly to Eq. (26), which allows for extracting the random stiffness terms $\boldsymbol{\mathcal{K}}^{(e)}_{\alpha\beta}$, $\widehat{\boldsymbol{\mathcal{K}}}^{(2)}_{\alpha\beta\gamma}$, and $\boldsymbol{\mathcal{K}}^{(3)}_{\alpha\beta\gamma\delta}$. The random quadratic term $\boldsymbol{\mathcal{K}}^{(2)}_{\alpha\beta\gamma}$ is then reconstructed according to Eq. (18) by using the formula

$$\boldsymbol{\mathcal{K}}^{(2)}_{\alpha\beta\gamma} \;=\; \frac{1}{2}\Big(\widehat{\boldsymbol{\mathcal{K}}}^{(2)}_{\alpha\beta\gamma} \;+\; \widehat{\boldsymbol{\mathcal{K}}}^{(2)}_{\beta\gamma\alpha} \;+\; \widehat{\boldsymbol{\mathcal{K}}}^{(2)}_{\gamma\alpha\beta}\Big). \tag{30}$$

The NL-SROM of a detuned configuration ℓ of the rotating bladed-disk in presence of mistuning is then written (see Eq. (25)) as

$$\mathbb{X}^{\ell}(t) = [\Phi^{\ell}]\,\mathbf{U}^{\ell}(t)\,, \tag{31}$$

in which $\mathbb{X}^{\ell}(t)$ is the $\mathbb{R}^n$-valued random vector corresponding to the nonlinear random displacements at time t of the HFCM for the detuned configuration ℓ in presence of mistuning. At time t, the $\mathbb{R}^n$-valued random vector $\mathbf{U}^{\ell}(t)$ of the generalized coordinates is then solution of the random nonlinear coupled differential equations, which are written, for $\alpha \in \{1,\ldots,M\}$, as

$$\mathcal{M}^{\ell}_{\alpha\beta}\,\ddot{U}^{\ell}_{\beta} + (C^{\ell}_{\alpha\beta} + \mathcal{D}^{\ell}_{\alpha\beta})\,\dot{U}^{\ell}_{\beta} + (\boldsymbol{\mathcal{K}}^{(e),\ell}_{\alpha\beta} + \boldsymbol{\mathcal{K}}^{(c),\ell}_{\alpha\beta} + \boldsymbol{\mathcal{K}}^{(g),\ell}_{\alpha\beta})\,U^{\ell}_{\beta} + \boldsymbol{\mathcal{F}}^{\mathrm{NL},\ell}_{\alpha}(U^{\ell}) \;=\; \mathcal{F}^{\ell}_{\alpha}\,, \tag{32}$$

in which the component α of the $\mathbb{R}^M$-valued random vector $\boldsymbol{\mathcal{F}}^{\mathrm{NL},\ell}(\mathbf{U})$ is

$$\boldsymbol{\mathcal{F}}^{\mathrm{NL},\ell}_{\alpha}(\mathbf{U}^{\ell}) = \boldsymbol{\mathcal{K}}^{(2),\ell}_{\alpha\beta\gamma}\,U^{\ell}_{\beta}\,U^{\ell}_{\gamma} + \boldsymbol{\mathcal{K}}^{(3),\ell}_{\alpha\beta\gamma\delta}\,U^{\ell}_{\beta}\,U^{\ell}_{\gamma}\,U^{\ell}_{\delta}\,. \tag{33}$$

The observation (quantity of interest) that is adapted to the detuning context in presence of random mistuning and that allows to quantify the dynamical amplification of the detuned configuration with random mistuning with respect to the configuration without detuning in presence of random mistuning, is defined in Section 3 (see Eq. (38)).

2.5. Numerical aspects related to the algorithms

This section is devoted to the computational strategy used for solving the NL-SROM. In the detuning context, the number n_c of distinct detuned configurations rapidly increases with the number N of blades of the bladed-disk as $n_c \simeq 2^N/N$. Furthermore, the NL-SROM is solved with the Monte-Carlo numerical simulation using $n_{\rm sim}$ realizations for which the numerical convergence has to be achieved in order to perform statistics post-processing. This means that there is a large number $n_c \times n_{\rm sim}$ of nonlinear differential equations with order M to be solved. Note that, in general for industrial bladed-disks, n_c is very large and it is impossible to solve $n_c \times n_{\rm sim}$ times the nonlinear reduced-order computational model, even with an efficient algorithm. Only a small number $N_d \ll n_c$ of detuned configurations in presence of mistuning can be computed. This is the reason why a surrogate model will be constructed in Section 4 with a probabilistic learning tool in order to solve the probabilistic-based combinatorial optimization problem and which will allow an optimal detuned configuration to be identified. In consequence, the computational algorithms require to be efficient in terms of computational costs. A careful attention has been paid in order to be able to browse the set of all the possible detuned configurations in presence of mistuning using the HFCM, when n_c is not to large. This approach is presented and analyzed in Section 3 and the obtained results will be used for validating the solving method of the probabilistic-based combinatorial optimization problem using a probabilistic learning tool, presented in Section 4.

2.5.1. Computational strategy for dealing with geometrical nonlinearities

In a deterministic finite element context, it should be noted that the construction of the linear reduced operators in Eq. (22) is usual and can easily be extracted using commercial softwares. From a computational point of view, the vector of the nonlinear reduced internal forces $\boldsymbol{\mathcal{F}}^{\rm NL}(\mathbf{U})$ and the tangential matrix, for which the nonlinear stiffness contribution is written as

$$[\mathcal{K}_{\rm T}^{\rm NL}(\mathbf{U})]_{\alpha\beta}\,\delta U_\beta = \frac{\partial \mathcal{F}_\alpha^{\rm NL}(\mathbf{U})}{\partial U_\beta}\,\delta U_\beta\,,$$

can also be extracted. Nevertheless, vector $\boldsymbol{\mathcal{F}}^{\rm NL}(\mathbf{U})$ is usually constructed by directly computing the contribution related to each finite element, without distinguishing the quadratic stiffness entries from the cubic stiffness entries. In such a case, the assemblage is quickly performed as a simple summation. In general, tangential matrix $[\mathcal{K}_{\rm T}^{\rm NL}(\mathbf{U})]$ is deduced from finite differences techniques. The present methodology requires the knowledge of entries $\widehat{\mathcal{K}}^{(2),\ell}_{\alpha\beta\gamma}$ and $\mathcal{K}^{(3),\ell}_{\alpha\beta\gamma\delta}$. Its detailed construction can be found in [52]. In the detuning context in presence of random mistuning, the computational procedure allowing for computing the random quantities $\boldsymbol{\mathcal{F}}^{\rm NL}(\mathbf{U})$ and $[\mathcal{K}_{\rm T}^{\rm NL}(\mathbf{U})]$ issued from the NL-SROM is summarized hereinafter.

1. Commercial software extraction or direct construction of the reduced linear elastic stiffness $\mathcal{K}^{(e)}_{\alpha\beta} = k^{(e)}(\boldsymbol{\varphi}^\beta, \boldsymbol{\varphi}^\alpha)$ according to Eq. (12).
2. Construction of the quadratic stiffness contribution $\widehat{\mathcal{K}}^{(2)}_{\alpha\beta\gamma} = \widehat{k}^{(2)}(\boldsymbol{\varphi}^\gamma, \boldsymbol{\varphi}^\beta, \boldsymbol{\varphi}^\alpha)$ and of the cubic stiffness contribution $\mathcal{K}^{(3)}_{\alpha\beta\gamma\delta} = k^{(3)}(\boldsymbol{\varphi}^\delta, \boldsymbol{\varphi}^\gamma, \boldsymbol{\varphi}^\beta, \boldsymbol{\varphi}^\alpha)$ according to Eqs. (19) and (20),

3. Construction of the global stiffness matrix $[\mathcal{K}^{\mathrm{NL}}]$ according to Eq. (26),
4. Construction of the random global stiffness matrix $[\mathcal{K}^{\mathrm{NL}}]$ according to Eq. (29), by optimizing the size Q of random matrix $[\mathbf{G}(\delta_K)]$.
5. Extraction from random matrix $[\mathcal{K}^{\mathrm{NL}}]$ of random quantities $\mathcal{K}^{(e)}_{\alpha\beta}$, $\widehat{\mathcal{K}}^{(2)}_{\alpha\beta\gamma}$, and $\mathcal{K}^{(3)}_{\alpha\beta\gamma\delta}$ and retrieving random stiffness $\mathcal{K}^{(2)}_{\alpha\beta\gamma}$ according to Eq. (30)
6. Computational evaluation of random nonlinear internal reduced force vector $\mathcal{F}^{\mathrm{NL}}(\mathbf{U})$ according to Eq. (33)
7. Depending on the computational algorithms used for solving nonlinear equations, computing the tangential matrix related to the nonlinear contribution $[\mathcal{K}^{\mathrm{NL}}_{\mathrm{T}}(\mathbf{U})]$ such that $[\mathcal{K}^{\mathrm{NL}}_{\mathrm{T}}(\mathbf{U})]_{\alpha\beta} = \mathcal{K}^{(2)}_{\alpha\beta\gamma}U_\gamma + \mathcal{K}^{(2)}_{\alpha\gamma\beta}U_\gamma + \mathcal{K}^{(3)}_{\alpha\beta\gamma\delta}U_\gamma U_\delta + \mathcal{K}^{(3)}_{\alpha\delta\beta\gamma}U_\gamma U_\delta + \mathcal{K}^{(3)}_{\alpha\delta\gamma\beta}U_\gamma U_\delta$.

2.5.2. Computational strategy for the nonlinear solver

The problem investigated concerns the forced regime of the bladed-disk, that is to say the nonlinear forced response that does not depend on initial conditions. The external excitation is thus a square integrable real-valued function on $\mathbb{R}$ whose Fourier transform has a compact support (see Section 3.3). For a given detuned configuration ℓ with random mistuning, the NL-SROM is solved in the time domain. An implicit unconditionally stable integration scheme corresponding to the Newmark method with an averaging acceleration scheme is chosen. With such integration scheme, for a given sampling time t_i, we then have to solve the following set of nonlinear coupled equations such that, for $\alpha = 1, \ldots, M$,

$$[\mathcal{K}^{\mathrm{eff}}]_{\alpha\beta}U_\beta(t_i) + \mathcal{F}^{\mathrm{NL}}_\alpha(\mathbf{U}(t_i)) = \mathcal{F}^{\mathrm{eff}}_\alpha(t_i)\,. \tag{34}$$

In Eq. (34), the random matrix $[\mathcal{K}^{\mathrm{eff}}]$ is the reduced effective stiffness matrix that is independent from sampling time. Note that $[\mathcal{K}^{\mathrm{eff}}]$ is positive definite almost surely for a fixed structure and is without signature for a rotating structure due to the antisymmetric gyroscopic coupling term. The random vector $\mathcal{F}^{\mathrm{eff}}(t_i)$ models the effective external load that has to be updated at each sampling time t_i.

There are several ways to solve iteratively such nonlinear coupled equation. The simplest method that is used is the fixed point method. The main advantage is that this iterative scheme is computationally expedient because it does not require the evaluation of the tangential matrix. Nevertheless, the algorithm does not necessarily converge. When the fixed-point algorithm does not converge, it can be replaced by a Newton-Raphson algorithm [55]. It should be noted that such algorithm requires the computation of the tangential matrix that is particularly time consuming. Furthermore, for nonlinear computations corresponding to a snap-back or snap-through behavior, the Newton algorithm does not converge beyond the critical limit corresponding to a null tangential stiffness matrix. In this case, the arc-length algorithm appears to be efficient for computing the solution. Nevertheless, such algorithm introduces a new additional scalar parameter $\zeta(t_i)$ that multiplies the right-hand side member of the nonlinear equation. In this case, we then introduce the residual random vector $\mathcal{R}(\mathbf{U}(t_i), \zeta(t_i))$ whose component α is defined by

$$\mathcal{R}_\alpha(\mathbf{U}(t_i), \zeta(t_i)) = \zeta(t_i)\mathcal{F}^{\mathrm{eff}}_\alpha(t_i) - [\mathcal{K}^{\mathrm{eff}}]_{\alpha\beta}U_\beta(t_i) - \mathcal{F}^{\mathrm{NL}}_\alpha(U(t_i))\,. \tag{35}$$

The algorithm is iterative. Several numerical approximations can be made. The first one consists in keeping the same tangential matrix $[\mathcal{K}^{\mathrm{NL}}_{\mathrm{T}}(\mathbf{U}(t_i))]$ along the successive iterations. The second one concerns the computation of the increment related to parameter $\zeta(t_i)$. The pure spherical

arc-length method is based on the fact that there always exists a hypersphere that intersects the load curve [56]. It then requires to solve a quadratic equation and to select amongst the two solutions the physical root. Improvements have been proposed based on linearization methods, for which the hypersphere is replaced by an hyperplan that is updated at each iteration [57] or not updated [58]. For a given sampling time t_i, such iterative scheme allows for computing a solution $(\mathbf{U}(t_i), \zeta(t_i))$ but does not allow for controlling the value of $\zeta(t_i)$. In the present case, the process is incrementally repeated in order to increase the value of $\zeta(t_i)$ that has to be controlled to 1. In order to achieve that, an adaptive arc length, depending on the number of iterations necessary to obtain the convergence of the previous increment is also implemented according to [55]. An unusual procedure is then added to the algorithm concerning parameter $\zeta(t_i)$. The state of the algorithm corresponding to the previous increment is stored. As the new incremental value of $\zeta(t_i)$ is found to be upper than 1, the algorithm is rewind to the previous increment and the computation is set again with the half of the arc-length. Such additional procedure is repeated until parameter $\zeta(t_i)$ reaches 1 within a numerical tolerance set.

3. Computational analysis of the role played by the geometrical nonlinearities in the detuned bladed-disk in presence of random mistuning and detuning optimization

For the computational analysis, we have deliberately chosen a blisk (turbomachine component comprising both rotor disk and blades) with mistuning with a relatively small number of blades so that the number of all the possible detuned configurations be also small. This will allow us

(1) to present a complete analysis of the role played by geometrical nonlinearities in the detuned blisk in presence of random mistuning,

(2) to build an exact solution (as the reference) of the combinatorial optimization problem introduced in Section 4. This reference will allow for validating the formulation of the combinatorial optimization problem (see Sections 4.1 to 4.5) and for validating the probabilistic machine learning tool for constructing a metamodel of the cost function (see Section 4.6 to 4.8). If we had chosen a larger number of blades, we would not have been able to build the reference solution of the combinatorial optimization problem, reference that is required for validation.

3.1. Description of the finite element model

The structure under consideration is a blisk with order $N = 12$ and with $n_w = N = 12$ blades whose finite element computational model is constructed with hexahedral solid finite elements with 8 nodes. The finite element mesh is issued from [59] for which the order of the cyclic symmetry has been modified from 24 to 12 as also used in [41]. The main motivation of such reduction of the number of blades is to decrease the number of possible detuning patterns in order to have a reasonable number of detuning possibilities, as previously explained. In the present case, the aim is to constitute a full reference data basis in the nonlinear mistuned/detuned context. When the detuning concept is approached with 2 possible types of blades, there are 352 possible detuned configurations when $N = 12$ that reduces the number of possibilities by a factor of almost $2^{N-1} \simeq 2\,000$ with respect to a structure with cyclic symmetry of order $2N = 24$. Let $(0, \mathbf{X}, \mathbf{Y}, \mathbf{Z})$ be the Cartesian reference coordinate system for which $(0, \mathbf{Z})$ coincides with the rotational axis for the blisk. Fig. 2 shows the finite element mesh of the blisk whose computational characteristics are summarized in Table 1. There are $n = 27\,108$ degrees of freedom (dof). The blisk is made up of a homogeneous and isotropic material with mass density $7\,860\ Kg/m^3$,

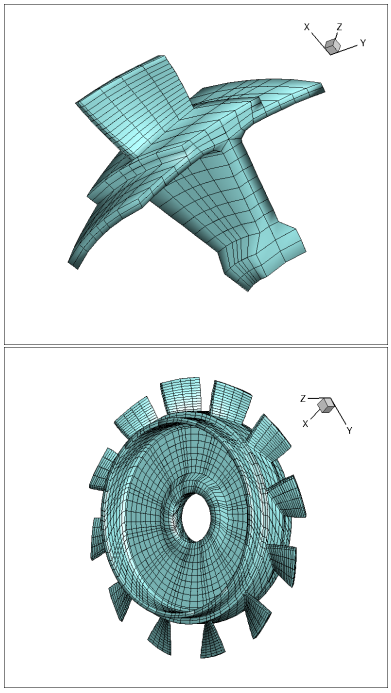

Figure 2: Finite element mesh of the blisk: blade sector (upper figure), full blisk (lower figure)

Poisson ratio 0.25, and Young modulus $2{\times}10^{11} N/m^2$. A Dirichlet condition is applied along the interfaces toward adjacent stages [59]. The fundamental frequency of the blisk is $\nu_0 = 977.32\,Hz$. A Rayleigh damping model (see Eq. (17)) is added for the blisk, with parameters $\alpha = 78.67\,s^{-1}$ and $\beta = 3.69{\times}10^{-7}\,s$ chosen such that the critical damping rate $\xi(2\pi\nu)$ belongs to $[0.0054, 0.008]$ for $\nu \in [900\,, 6\,000]\,Hz$ as shown in Fig. 3.

	Elements	Nodes	dof
Sector	476	846	2151
Full model	5712	9 036	27 108

Table 1: Computational characteristics of the finite element model

3.2. Modal characteristics of the tuned blisk

The eigenfrequencies (natural frequencies) of the structure are computed using the cyclic symmetry. Fig. 4 displays the eigenfrequencies of the tuned blisk with respect to its circumferential wave number. The graph exhibits several veerings. Let $\nu_{h,i}$ be the eigenfrequency number i related to the number h of nodal diameters. In the present case, the veering corresponding to $h = 2$ nodal diameters corresponds to (double) eigenfrequency $\nu_{2,4} = 4\,845.18\,Hz$ that is related to a dominant blade motion and to (double) eigenfrequency $\nu_{2,5} = 5\,091.09\,Hz$ that is related to a blisk global motion as can be shown in Fig. 5.

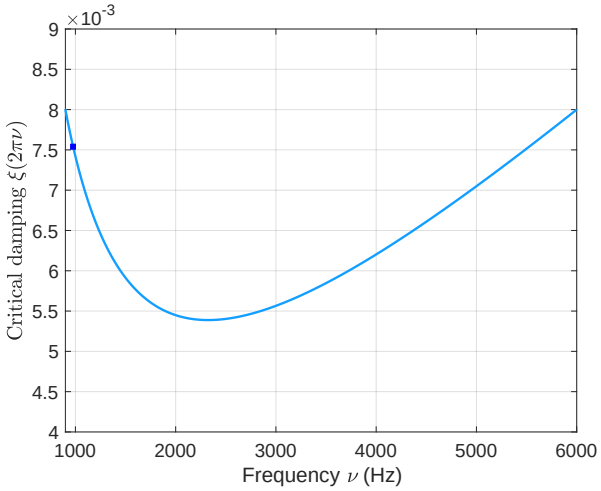

Figure 3: Critical damping rate: graph of $\nu \mapsto \xi(2\pi\nu)$. Square symbol is related to fundamental frequency $\nu_0 = 977.32\,Hz$ and $\xi_0 = \xi(2\pi\nu_0) = 0.00754$.

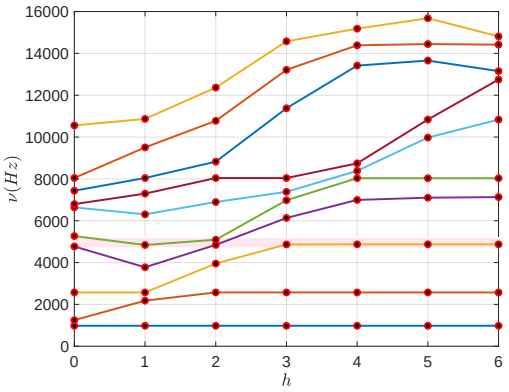

Figure 4: Graph of the eigenfrequencies ν of the tuned blisk with respect to its circumferential wave number h

3.3. Choice of the external excitation and time-frequency sampling

Since we are interested in the forced response of the structure, the presence of geometrical nonlinearities requires to solve the nonlinear equations in the time domain. The time-dependent external excitation is modeled by the $\mathbb{R}^n$-vector $\mathbf{F}(t)$ whose block decomposition according to each sector is given by $\mathbf{F}(t) = \left(\mathbf{F}^0(t), \ldots, \mathbf{F}^{N-1}(t)\right)$ such that

$$\mathbf{F}^j(t) = s_0\, g^j(t)\, \mathbb{F} \quad , \quad j \in \{0, 1, \ldots, N-1\}\,,$$

in which s_0 is the load intensity that allows the nonlinearity rate to be calibrated, $t \mapsto g^j(t)$ is a square integrable real-valued function on $\mathbb{R}$, which characterizes the time evolution of the load, and where $\mathbb{F}$ is a $\mathbb{R}^{\overline{n}}$-vector describing the space localization of the load related to a given sector,

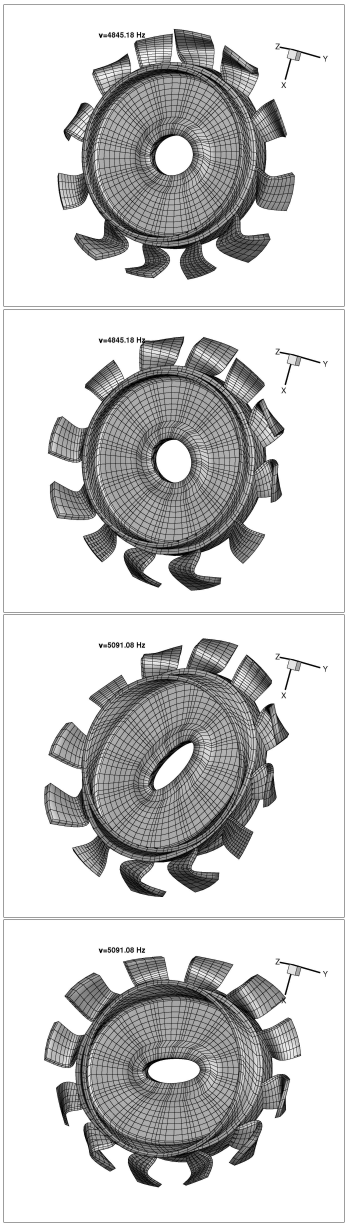

Figure 5: Graph of the modal shapes related to double eigenfrequencies $\nu_{2,4} = 4\,845.18\,Hz$ (upper figures corresponding to blade dominant motion) and to $\nu_{2,5} = 5\,091.09\,Hz$ (lower figures corresponding to blisk global motion)

in which integer $\overline{n}$ is equal to n/N. The Fourier transform of function $t \mapsto g^j(t)$ is the $\mathbb{C}$-valued function again noted g^j, but for which its argument is $2\pi\nu$, such that

$$g^j(2\pi\nu) = \int_{\mathbb{R}} e^{-2\imath\pi\nu t} g^j(t)\, dt \quad , \quad \nu \in \mathbb{R}\,,$$

in which ι is the imaginary unit. Complex-valued function $\nu \mapsto g^j(2\pi\nu)$ is assumed to have a compact support $\overline{\mathbb{B}}_e \cup \mathbb{B}_e \in \mathbb{R}$, independent of j, with $\overline{\mathbb{B}}_e = [-\nu_{\max}, -\nu_{\min}]$ and $\mathbb{B}_e = [\nu_{\min}, \nu_{\max}]$. This support is chosen as the frequency band of excitation for which $\nu_{\min} = 4\,700\,Hz$ and $\nu_{\max} = 5\,200\,Hz$ (see Fig. 7) in order that $\mathbb{B}_e$ contains the veering region for $h = 2$ (see Fig. 4). Time function g^j differs from one sector to another one by a constant phase shift $\varphi_j = (4\pi j)/N$. This choice of the phase allows the modes with $h = 2$ nodal diameters to be excited for the linearized dynamical system. For all t in $\mathbb{R}$, we write

$$g^j(t) = \sum_{k=1}^{S} \frac{2}{\pi t} \sin(\pi \Delta\nu\, t)\, \cos(2\pi s_k\, \Delta\nu\, t + \varphi_j)$$

in which $\Delta\nu = (\nu_{\max} - \nu_{\min})/S$ and where $s_k = \nu_{\min}/\Delta\nu + (2k-1)/2$. Consequently, $|g^j(2\pi\nu)| = 1$ if ν belongs to $\overline{\mathbb{B}}_e \cup \mathbb{B}_e \in \mathbb{R}$ and is equal to 0 if does not. Therefore, the structure is uniformly excited in band $\mathbb{B}_e$. From a numerical point of view, the computation is carried out on a truncated time domain $\mathbb{T} = [t_{\text{ini}}, t_{\text{ini}} + T]$. The initial time is chosen as $t_{\text{ini}} = -0.06\,s$ yielding a null initial load. The time duration T is then adjusted so that the system be returned at its equilibrium state within a given numerical tolerance for both linear and nonlinear computations. Even the fundamental eigenfrequency does not belong to excitation frequency band $\mathbb{B}_e$, it can indirectly be excited through the geometrical nonlinear effects. Let $\xi_0 = 0.00754$ be the critical damping rate at fundamental frequency ν_0 as shown in Fig.3. Time duration is chosen as $T = 0.128\,s$, which ensures the system to return to its equilibrium state with a negligible relative tolerance $\tau = e^{-2\pi\xi_0\nu_0 T} < 10^{-12}$ when fundamental frequency is excited. The sample frequency ν_e and the number of time steps are then chosen as $\nu_e = 64\,000\,Hz$ and $n_t = 8\,192$ yielding a constant sampling time step $\delta t = 15.6\times10^{-6}\,s$ and a constant sampling frequency step $\delta\nu = 7.8125\,Hz$. Function $\nu \mapsto g^j(2\pi\nu)$ is estimated by using FFT. A convergence analysis is carried out with respect to the number $S + 1$ of subdivisions of frequency band $\mathbb{B}_e$. Let $\text{Conv}_1(S)$ be defined by

$$\text{Conv}_1(S) = \frac{\int_{\mathbb{R}^+} |g^j(2\pi\nu)|\, d\nu}{\nu_{\max} - \nu_{\min}}\,.$$

Fig. 6 shows the graph of $S \mapsto \text{Conv}_1(S)$. It can be seen that $S = 30$ yields a good representation of $|g^j(2\pi\nu)|$. Fig. 7 displays the graphs of $t \mapsto g^0(t)$ and $\nu \mapsto |g^0(2\pi\nu)|$. The spatial repartition of the external load described by the normalized vector $\mathbb{F}$ is such that an external point load is applied along all directions at the excitation nodes located at the tip of each blade with a constant phase shift $\pi/3$. The load intensity s_0 is adjusted to get sufficient geometrical nonlinear effects that modify the vibrational behavior of the blisk.

3.4. Convergence analysis with respect to time sampling

The efficiency and the accuracy of the Newmark time integration scheme coupled with a Newton-Raphson procedure is investigated. The load intensity is set to $s_0 = 10\,N$ that corresponds to a situation for which nonlinear effects occur, involving displacements of magnitude $2\times10^{-3}\,m$ at the tip of blade, knowing that the blade thickness is $6.7\times10^{-3}\,m$. The nonlinear reduced-order model is then constructed with $M = 72$ elastic modes corresponding to increasing eigenfrequencies up to $\nu_{6,12} = 10\,835.13\,Hz$. The frequency band of analysis $\mathbb{B}$ is chosen as $\mathbb{B} = [300\,,\,6\,000]\,Hz$. We are then interested in the nonlinear computations for which the nonlinear response is calculated in the truncated time domain $\mathbb{T} = [-0.06, 0.068]\,s$. For performing the convergence analysis, the values of parameters δt, n_t, and ν_e are given in Table 2.

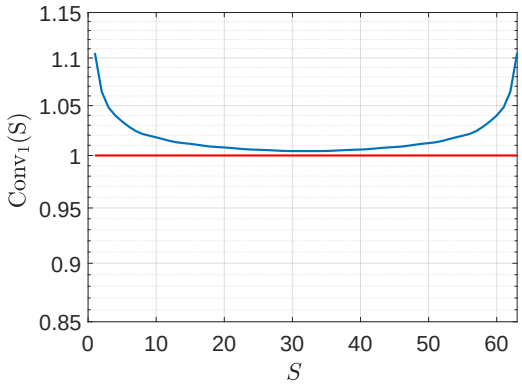

Figure 6: Graph of convergence function $S \mapsto \mathrm{Conv}_1(S)$.

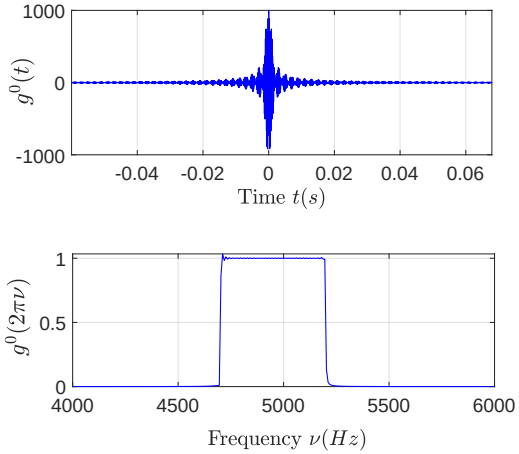

Figure 7: Graph of $t \mapsto g^0(t)$ (upper figure) and $\nu \mapsto |g^0(2\pi\nu)|$ (lower figure).

$T(s)$	0.128×10^{-3}	0.128×10^{-3}	0.128×10^{-3}	0.128×10^{-3}	0.128×10^{-3}	0.128×10^{-3}
$\delta t(s)$	62.5×10^{-6}	31.2×10^{-6}	20.8×10^{-6}	15.6×10^{-6}	12.5×10^{-6}	10.4×10^{-6}
n_t	2 048	4 096	6 144	8 192	10 240	12 288
$\nu_e(Hz)$	16 000	32 000	48 000	64 000	80 000	96 000

Table 2: Numerical parameters for Newmark algorithm

Let $\mathbf{u} = (u_1, \ldots, u_M)$ be the vector of the M modal coordinates. Let $\delta t \mapsto \mathrm{Conv}_2(\delta t)$ be the convergence function defined by

$$\mathrm{Conv}_2(\delta t) = \sqrt{\int_{\mathbb{B}} \|\mathbf{u}(2\pi\nu;\delta t)\|^2 d\nu}\,,$$

in which $\|\mathbf{u}(2\pi\nu;\delta t)\|^2 = \sum_{i=1}^{M} |u_i(2\pi\nu;\delta t)|^2$ and where the $\mathbb{C}^M$-vector $\mathbf{u}(2\pi\nu;\delta t)$ is the Fourier

transform of the $\mathbb{R}^M$-valued function $t \mapsto \mathbf{u}(t;\delta t)$. Fig. 8 shows the graph of $\delta t \mapsto \mathrm{Conv}_2(\delta t)$. It can be seen that a reasonable convergence is obtained for $\delta t = 15.6{\times}10^{-6}\ s$ yielding $n_t = 8\,192$ time steps, $\nu_e = 64\,000\ Hz$, and a frequency resolution $\delta\nu = 7.8\ Hz$.

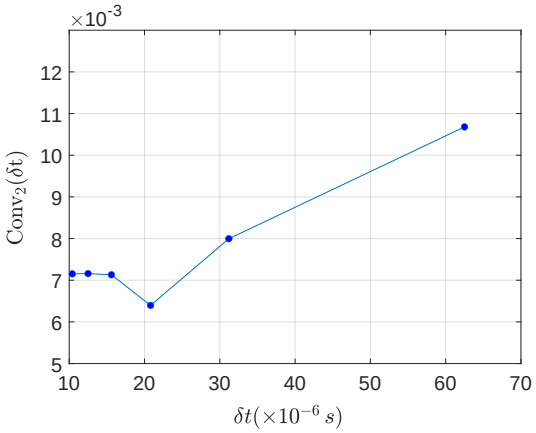

Figure 8: Convergence analysis with respect to time sampling δt. Graph of function $\delta t \mapsto \mathrm{Conv}_2(\delta t)$.

Let $\mathbb{x}^{\mathrm{tip}}(t) = (\mathbb{x}_1^{\mathrm{tip}}(t), \mathbb{x}_2^{\mathrm{tip}}(t), \mathbb{x}_3^{\mathrm{tip}}(t))$ be the displacement vector of the node located at the tip of blade number 0 and let $\mathbb{x}_i^{\mathrm{tip}}(2\pi\nu)$ be its Fourier transform. Fig. 9 displays the graphs of $t \mapsto \mathbb{x}_3^{\mathrm{tip}}(t)$ and $\nu \mapsto |\mathbb{x}_3^{\mathrm{tip}}(2\pi\nu)|$. First of all, it can be seen that the structure returns to its equilibrium state at the end of the simulation. The time response is strongly sensitive to the choice of δt. The response in the frequency domain displays consequent nonlinear effects, since the structure responds outside the frequency band of excitation $\mathbb{B}_e$. The convergence with respect to the choice of δt is relatively quick when analyzing the structure in the excitation frequency band. The fundamental frequency of the blisk is also excited through the nonlinearities and it can be seen that this response is strongly over-estimated when choosing $\delta t = 62.5{\times}10^{-6}\ s$ and becomes stable from for time steps lower than $\delta t = 15.6{\times}10^{-6}\ s$, which is confirmed by the zoom of the nonlinear response in the low-frequency range displayed in Fig. 10. From now on all the computations in the time domain are done taking $\delta t = 15.6{\times}10^{-6}\ s$.

3.5. Convergence analysis with respect to the order of the reduced-order model

The accuracy of the NL-ROM is investigated with respect to the order M of the reduced-order model. The elastic modes are sorted by increasing order of their eigenfrequencies belonging to a family of modes that are represented in Fig. 4. The load intensity is set to $s_0 = 10\,N$ and the time step is set to $\delta t = 15.6{\times}10^{-6}\ s$. Denoting always $\mathbf{u} = (u_1, \ldots, u_M)$ as the vector of the M modal coordinates, the convergence function $M \mapsto \mathrm{Conv}_3(M)$ is defined by

$$\mathrm{Conv}_3(M) = \sqrt{\int_{\mathbb{B}} \|\mathbf{u}(2\pi\nu; M)\|^2 d\nu}\,,$$

in which $\|\mathbf{u}(2\pi\nu; M)\|^2 = \sum_{i=1}^{M} |u_i(2\pi\nu; M)|^2$ and where the $\mathbb{C}^M$-vector $\mathbf{u}(2\pi\nu; M)$ is the Fourier transform of the $\mathbb{R}^M$-valued function $t \mapsto \mathbf{u}(t; M)$. The superscript $^{\mathrm{lin}}$ is added for the computation

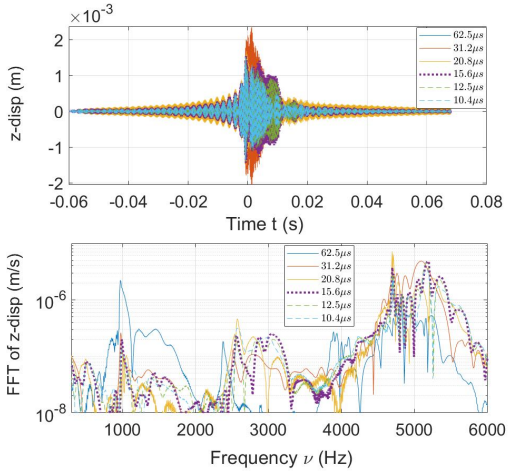

Figure 9: Graph of function $t \mapsto \mathfrak{X}_3^{\text{tip}}(t)$ representing the nonlinear response at the tip of blade 0 in the transverse direction for different values of δt (upper figure). Graph of $\nu \mapsto |\mathfrak{X}_3^{\text{tip}}(2\pi\nu)|$ in the frequency analysis $\mathbb{B} = [300, 6\,000]$ *Hz*.

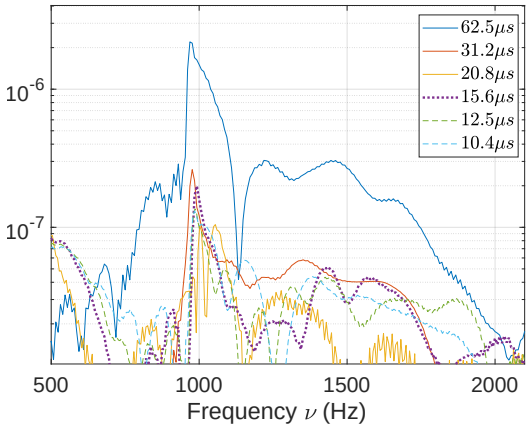

Figure 10: Zoom of the graph of function $\nu \mapsto |\mathfrak{X}_3^{\text{tip}}(2\pi\nu)|$ in the very low-frequency range, for different values of δt.

corresponding to the response of the linearized system. Fig. 11 displays the graphs of functions $M \mapsto \text{Conv}_3^{\text{lin}}(M)$ (upper graph) and $M \mapsto \text{Conv}_3(M)$ (lower graph). It should be noted that for each considered order M, the corresponding value of function $\text{Conv}_3(M)$ has been obtained by performing a whole deterministic nonlinear analysis using the NL-ROM parameterized by M. As expected, it can be seen that the converged values of both convergence functions differ, that underlines the presence of effects induced by the geometrical nonlinearities. As expected, it can also be seen that the convergence is slower in the nonlinear case. It should also be noted that the nonlinear tuned case yields response levels that are much more lower than the corresponding linearized case, which means that the geometrical nonlinearities have a stiffening effect on the vibrational behavior of the bladed-disk. Note also that the convergence analysis exhibits a maxi-

linear										
h	2	2	1	3						
$\nu(Hz)$	4845.2	5091.1	4840.0	4865.6						
ratio	1.0000	0.3660	0.2108	0.1927						
nonlinear										
h	2	2	1	3	0	5	2	4	6	0
$\nu(Hz)$	5091.1	4845.2	4840.0	4865.6	5266.1	4872.1	2571.5	4871.3	4872.1	4768.6
ratio	1.0000	0.8001	0.5421	0.3519	0.3129	0.2694	0.2653	0.2431	0.2375	0.2092

Table 3: Analysis of the most contributing generalized coordinates

mum when the nonlinear reduced-order model of order $M = 48$ is used for the computations. The main contribution comes from mode with $\nu_{2,5} = 5091.09\,Hz$, which is the mode with the higher frequency that is located in the excitation frequency band and that is directly excited by the load vector. Such an overestimation is then corrected by including additional modes in the nonlinear reduced-order model. From now on, the order of the NL-ROM is fixed to $M = 72$.

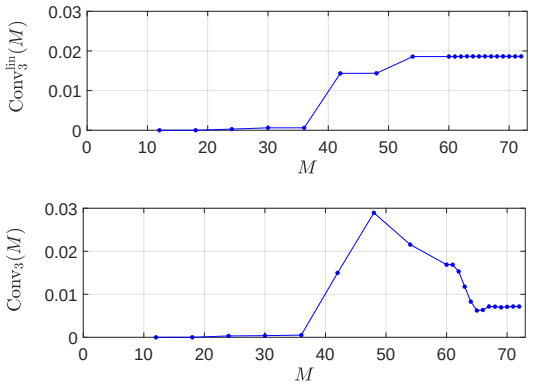

Figure 11: Convergence analysis with respect to the order M of the NL-ROM. Graph of function $M \mapsto \mathrm{Conv}_3^{\mathrm{lin}}(M)$ corresponding to the linearized case (upper graph) and graph of $M \mapsto \mathrm{Conv}_3(M)$ (lower graph).

An analysis of the most contributing generalized coordinates is carried out over $\mathbb{B}$ and presented in Table 3. In the linear case, it is seen that the most contributing generalized coordinates are related to natural eigenfrequencies $\nu_{2,5} = 5091.1\,Hz$ and $\nu_{2,4} = 4845.2\,Hz$. Moreover there are also two other contributions that are non negligible, that are located in $\mathbb{B}_e$, and that are not related to circumferential wave number $h = 2$. This is not theoretically expected since the load has been constructed to only excite circumferential wave number $h = 2$. Nevertheless, in the present case, the forced response is solved in the time domain. The signal is theoretically defined for $t \in \mathbb{R}$ but is numerically truncated, which explains those secondary contributions. In the nonlinear case, all the natural frequencies located in $\mathbb{B}_e$ are contributing to the nonlinear response. It should also be noted that the ratios of the generalized coordinates related to natural frequencies $\nu_{2,2} = 2571.5\,Hz$ and $\nu_{0,5} = 5266.1\,Hz$, that are located outside the excitation frequency band do have a non negligible participation.

3.6. Effects of the geometrical nonlinearities

In order to have a better understanding of the structural behavior of the blisk, it is essential to perform a sensitivity analysis of the nonlinear response with respect to load intensity s_0. The computations are carried out with numerical parameters set to $\delta t = 15.6\times10^{-6}\,s$ and $M = 72$. Parameter s_0 controls the level of nonlinear effects that can be quantified as follows. A criterion is that the nonlinear response does no longer coincide with the response of the linearized system (small deformations, small displacements) as soon as vibrations appear outside the excitation frequency band $\mathbb{B}_e$. As previoulsly, let $\mathbf{u} = (u_1, \ldots, u_M)$ be the vector of the M modal coordinates and let $s_0 \mapsto \mathrm{Conv}_4(s_0)$ be the function defined by

$$\mathrm{Conv}_4(s_0) = \frac{\int_{\mathbb{B}_e} \|\mathbf{u}(2\pi\nu; s_0)\|^2 d\nu}{\int_{\mathbb{B}} \|\mathbf{u}(2\pi\nu; s_0)\|^2 d\nu},$$

in which $\|\mathbf{u}(2\pi\nu; s_0)\|^2 = \sum_{i=1}^{M} |u_i(2\pi\nu; s_0)|^2$ and where the $\mathbb{C}^M$-vector $\mathbf{u}(2\pi\nu; s_0)$ is the Fourier transform of the $\mathbb{R}^M$-valued function $t \mapsto \mathbf{u}(t; s_0)$. Such function is equal to unity as long as the linear assumption remains valid. Consequently, there exists a threshold $s_{\min}$ above which geometrical nonlinearities can no longer be neglected. Fig. 12 shows the graph of function $s_0 \mapsto \mathrm{Conv}_4(s_0)$. The threshold value is found to be $s_{\min} = 1\,N$.

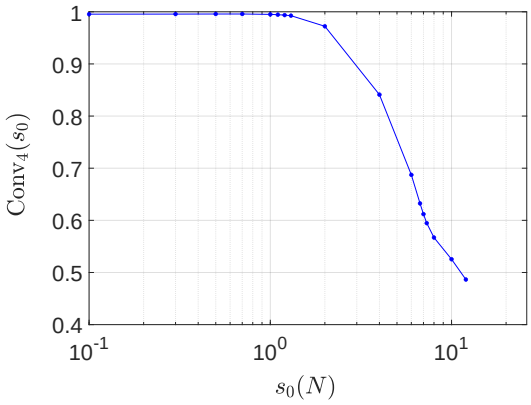

Figure 12: Sensitivity analysis with respect to load intensity s_0. Graph of function $s_0 \mapsto \mathrm{Conv}_4(s_0)$.

3.7. Convergence analysis with respect to the size Q *of the random germ.*

As defined in Section 2.4, the global stiffness matrix $[\mathcal{K}^{\mathrm{NL}}]$ corresponding to a reduced-order model of order $M = 72$ has a size $(P \times P)$ with $P = 72 \times 73 = 5256$. Figure 13 represents the function $j \mapsto [\Lambda^{\mathrm{Q}}]_{jj}$ where the eigenvalues of matrix $[\mathcal{K}^{\mathrm{NL}}]$ are sorted by decreasing values. One chooses Q so that eigenvalues that are greater than 10^{-6} the fundamental one and their corresponding eigenvectors are kept in the reduction so that $\mathrm{Q}=440$. Note that this value defined the length of the random vector used for constructing random matrix $[\mathbf{G}(\delta_K)]$. Let be $\mathrm{Conv}_5(\mathrm{Q})$ be the function defined by

$$\mathrm{Conv}_5(\mathrm{Q}) = \sqrt{\frac{\|\Delta\mathcal{K}(\mathrm{Q})\|^2}{\|\mathcal{K}^{\mathrm{NL}}\|^2}}$$

It can be shown that $\mathrm{Conv}_5(\mathrm{Q}=440) = 1.98 \times 10^{-6}$ which allows a good representation of the solution to be obtained and which is such that $\mathrm{Q}=440 \ll P=5256$.

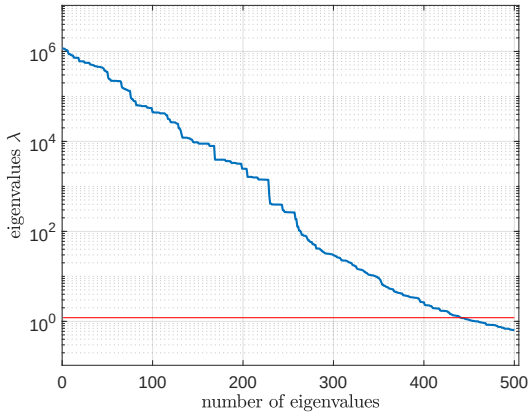

Figure 13: Convergence analysis with respect to the number Q of eigenvectors to be kept in the simulation. Graph of function $j \mapsto [\Lambda^{\mathrm{Q}}]_{jj}$.

3.8. Convergence analysis with respect to the number of Monte Carlo numerical simulations for the mistuned blisk without intentional detuning

The load intensity is set to $s_0 = 10\,N$ that corresponds to significant nonlinear effects and the numerical parameters are set to $M = 72$ and $\delta t = 15.6{\times}10^{-6}\ s$. The pure mistuning (that is to say without intentional detuning) of the blisk is considered through the nonparametric probabilistic approach with a hyperparameter δ_K set to $\delta_K = 0.1$.

Since the nonparametric probabilistic approach is used for modeling the mistuning, it seems important to precise what is the physical meaning of the choice of hyperparameter $\delta_K = 0.1$ in the pure mistuning case. Figure 14 displays the probability density function of the first three eigenfrequencies with circumferential wave number $h = 0$ using kernel density estimation in order to provide the level of variations of the natural frequencies induced by the pure mistuning when using the nonparametric probabilistic approach. The nonlinear random responses obtained in the pure mistuning case allows for the order of magnitude of the amplification to be estimated, yielding a mean level of amplification of 1.222, a corresponding standard deviation of 0.164 and a 98th quantile of 1.629.

The convergence analysis with respect to the number n_{sim} of Monte Carlo numerical simulations is investigated. Let $\mathbf{U} = (U_1, \ldots, U_M)$ be the random vector of the M modal coordinates on the probability space $(\Theta, \mathcal{T}, \mathcal{P})$. Let $\mathrm{Conv}_6(n_{\mathrm{sim}})$ be the function defined by

$$\mathrm{Conv}_6(n_{\mathrm{sim}}) = \sqrt{\frac{1}{n_{\mathrm{sim}}} \sum_{\alpha=1}^{n_{\mathrm{sim}}} \int_{\mathbb{B}} \|\mathbf{U}(2\pi\nu;\theta_\alpha)\|^2 d\nu}\,,$$

in which, for $\theta_\alpha \in \Theta$, $\mathbf{U}(2\pi\nu;\theta_\alpha)$ is the realization of the $\mathbb{C}^M$-valued random variable $\mathbf{U}(2\pi\nu)$ such that the $\mathbb{C}^M$-valued function $\nu \mapsto \mathbf{U}(2\pi\nu;\theta_\alpha)$ is the Fourier transform of the $\mathbb{R}^M$-valued function $t \mapsto \mathbf{U}(t;\theta_\alpha)$. Fig. 15 displays the graph of function $n_{\mathrm{sim}} \mapsto \mathrm{Conv}_6(n_{\mathrm{sim}})$. It is found that a good convergence is obtained from $n_{\mathrm{sim}} = 400$.

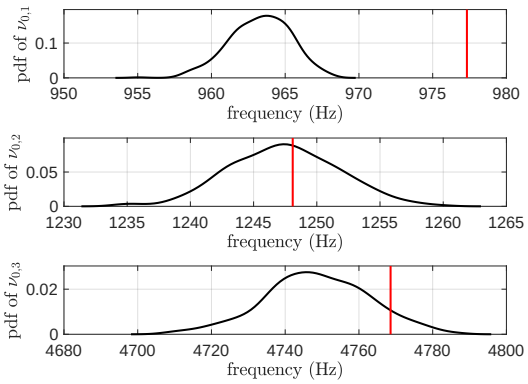

Figure 14: Estimation of the probability density function $p_{\nu_{0,i}}(\nu)$ for $i = \{1, 2, 3\}$ of the first three natural frequencies with circumferential wave number $h=0$ using kernel density estimation. Corresponding natural frequencies for the tuned case (red line).

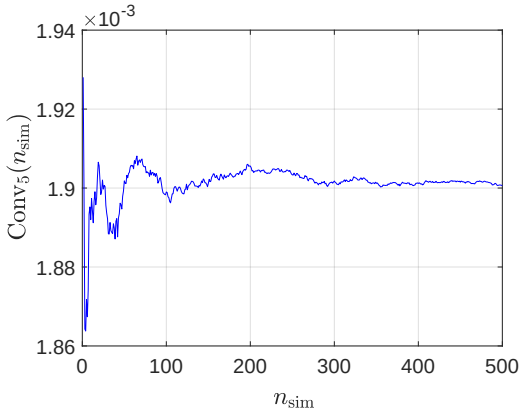

Figure 15: Convergence analysis with respect to the number n_{sim} of realizations for the Monte Carlo numerical simulation of the NL-SROM. Graph of function $n_{\mathrm{sim}} \mapsto \mathrm{Conv}_6(n_{\mathrm{sim}})$.

3.9. Quantification of the computational costs with regard to the detuning context of the mistuned blisk

These numerical computations are essential (1) to better understand the dynamic behavior of the blisk and (2) to optimize for the best the computational costs while keeping a predictive computational model that ensures a good accuracy on the nonlinear dynamical response. From now on, the load intensity is set to $s_0 = 10\,N$ that corresponds to significant nonlinear effects (see Fig. 12). The mistuning level is characterized by a dispersion level $\delta_K = 0.1$ and the numerical parameters are set to $M = 72$, $\delta t = 15.6\times10^{-6}\,s$, $n_{\mathrm{sim}} = 500$, and $\mathrm{Q} = 440$. It is essential to underline that all these convergence analyses have to be carried out meticulously. The aim of this work concerns the optimization of the detuning of the blisk in presence of mistuning. The computational model of the detuned blisk is constructed from the knowledge of two compatible meshes of two different sector types denoted as 1 and 2. The reference sector 2 is obtained from

nb_1	12	11	10	9	8	7	6	5	4	3	2	1	0
nb_2	0	1	2	3	4	5	6	7	8	9	10	11	12
$\widetilde{n}_c(nb_1, nb_2)$	1	1	6	19	43	66	80	66	43	19	6	1	1

Table 4: Number $\widetilde{n}_c(nb_1, nb_2)$ of detuned configurations as a function of the number nb_1 and nb_2 of blades of type 1 and 2.

sector 1 by decreasing the Young modulus of the blade from $\text{Young}_1 = 2.00\times10^{11}\,\text{N/m}^2$ to $\text{Young}_2 = 1.80\times10^{11}\,\text{N/m}^2$.

Let us denote by nb_1 and nb_2 the number of blades of type 1 and type 2 in a detuned configuration. Let $\widetilde{n}_c(nb_1, nb_2)$ be the number of possible detuned configurations having nb_1 and nb_2 blades of type 1 and 2 respectively. Let n_c be the total number of detuned configurations for all the possible values of nb_1 and nb_2. For the tuned blisk with cyclic symmetry of order $N = 12$, Table 4 gives the number $\widetilde{n}_c(nb_1, nb_2)$ of detuned configurations as a function of the number nb_1 and nb_2 of blades of type 1 and 2. There are a total number of $n_c = 352$ possible detuned configurations (patterns).

The objective is to find the optimal configuration (pattern) that will reduce for the best the response amplification induced by mistuning. Another objective is to have a complete knowledge of the nonlinear dynamical behavior of all possible detuned configurations in order to constitute a reference data basis. In the present numerical study, all the computations are distributed according to the number n_{sim} of Monte Carlo realizations and are made on workstations with 1 536 GB RAM and 30 cores (Intel(R) Xeon(R) Platinum 8 168 CPU@2.9Ghz). The generated elapsed time is about 6 hours to perform 1 computation corresponding to the nonlinear analysis of 1 detuned pattern in presence of mistuning, which means that the construction of the full data basis requires an elapsed time of about 88 days of computations.

3.10. Choice of the observation

The pure mistuning case corresponds to the usual situation for which the blisk is described with a tuned configuration in presence of mistuning. In that particular case, the deterministic case corresponds to a structure with a perfect cyclic symmetry with order N. The usual mistuning analyses, whether it is in a linear or nonlinear context, characterize the mistuning effects by introducing a random amplification factor that is expressed with respect to the deterministic resonance of the structure with perfect cyclic symmetry.

The detuned configuration in presence of mistuning is defined by a given distribution of the blades of type 1 and 2. The detuned configuration number ℓ is then represented by a vector $\mathbf{w}^{c,\ell} \in \{0,1\}^{n_w}$ whose component $w_j^{c,\ell}$ is equal to 0 or 1 whether the blade is of type 1 or of type 2. Let us recall that for a given mistuning level, the drastic mistuning effects yield a response amplification with respect to its deterministic counterpart. The objective is to find detuned configurations whose mistuning effects induce less amplification than the one obtained with the tuned configuration in presence of mistuning. The idea is then to define a scalar quantity that is able to quantify the mistuning effects of the detuned configuration with respect to the unavoidable mistuning effects of the tuned configuration.

Let $\mathbf{X}^{\ell}(j, 2\pi\nu_i, \theta_k)$ be the $\mathbb{C}^{3n_b}$-vector of the realization θ_k of the $3n_b$-displacement dofs of blade number $j \in \{1, \ldots, n_w\}$ in the frequency domain, taken at frequency ν_i, and corresponding

to the detuned configuration number ℓ. Let $[\underline{t}_j]$ be the $(3n_b \times n)$ real matrix that allows for restraining the complex vector of the n displacement-dofs of the structure to those related to blade number j, we have

$$\mathbf{X}^\ell(j, 2\pi\nu_i, \theta_k) = [\underline{t}_j]\,[\Phi^\ell]\,\mathbf{U}^\ell(2\pi\nu_i, \theta_k)\,,$$

in which $[\Phi^\ell] \in \mathbb{M}_{n,M}$ is the matrix of the M elastic modes for configuration ℓ and where $\mathbf{U}^\ell(2\pi\nu_i, \theta_k)$ is the realization $\theta_k \in \Theta$ of the $\mathbb{C}^M$-valued random variable $\mathbf{U}^\ell(2\pi\nu_i)$ of the modal coordinates at frequency ν_i.

For blade number j of configuration ℓ, at frequency ν_i, and for realization θ_k, we define the scalar observation $Y^\ell(j, 2\pi\nu_i, \theta_k) = \|\mathbf{X}^\ell(j, 2\pi\nu_i, \theta_k)\|$. Since the mistuning context requires to consider the resonance of the most responding blade, we define the $\mathbb{R}^+$-valued random variable A^ℓ whose realization $a^{\ell,k} = A^\ell(\theta_k)$ is such that

$$a^{\ell,k} = \max_j\{\max_i\ Y^\ell(j, 2\pi\nu_i, \theta_k)\}\,. \tag{36}$$

We define the associated random variable $J^\ell_{\max}$ whose realization $j^{\ell,k}_{\max} = J^\ell_{\max}(\theta_k)$ is such that

$$j^{\ell,k}_{\max} = \arg\max_j\{\max_i\ Y^\ell(j, 2\pi\nu_i, \theta_k)\}\,. \tag{37}$$

In order to get a robust scalar quantity for characterizing the random nonlinear dynamical behavior of the blisk, an estimate of the maximum extreme value statistics of random variable A^ℓ is introduced. It should be noted that, for a fixed ℓ-configuration, the maximum is used so that all realizations are in the confidence domain with the greatest probability. This estimation is constructed as follows. The available number of Monte Carlo numerical simulations is written as $n_{\text{sim}} = \nu_r\,\nu_e$ (for $n_{\text{sim}} = 500$, $\nu_e = 10$ and $\nu_r = 50$). We then define, for $r \in \{1, \ldots, \nu_r\}$,

$$a^{\ell,r}_M = \max_{k\in\{\nu_e(r-1)+1,\ldots,r\nu_e\}} a^{\ell,k}\,,$$

in which $a^{\ell,k}$ is defined by Eq. (36) and we define its mean value, $\underline{a}^\ell_M$, such that

$$\underline{a}^\ell_M = \frac{1}{\nu_r}\sum_{r=1}^{\nu_r} a^{\ell,r}_M\,.$$

The observation of the detuned ℓ-configuration with mistuning is then defined as the amplification factor $q^{c,\ell}$ with respect to its tuned counterpart with pure mistuning,

$$q^{c,\ell} = \frac{\underline{a}^\ell_M}{\underline{a}^{\text{t}}_M}\,, \tag{38}$$

in which superscript t is related to the tuned configuration.

3.11. Some remarks concerning the nonlinear detuning optimization and the linearized detuning optimization

In this paragraph, we investigate the deterministic response of the two tuned configurations with cyclic symmetry with order $N = 12$. Concerning the tuned configuration with blades of type 1, the natural eigenfrequencies related to the veering with circumferential wave number $h = 2$ are the double eigenfrequencies $\nu^{\text{type1}}_{2,4} = 4845.18\,Hz$ and $\nu^{\text{type1}}_{2,5} = 5091.09\,Hz$. Concerning

the tuned configuration with blades of type 2, the natural eigenfrequencies related to the veering with circumferential wave number $h=2$ are the double eigenfrequencies $\nu_{2,4}^{\text{type2}} = 4596.54\,Hz$ and $\nu_{2,5}^{\text{type1}} = 4829.83\,Hz$. Since the excitation frequency band $\mathbb{B}_e$ is a narrow excitation frequency band chosen as $\mathbb{B}_e = [4700\,,\,5200]\,Hz$, it can be seen that the tuned configuration with 12 blades of type 2 only presents one resonance in $\mathbb{B}_e$. In the linearized case, this means that there will be some detuned configurations for which there will be only one resonance in frequency band of analysis. $\mathbb{B}$. Let $y^{\text{type}\,\alpha}(2\pi\nu_i)$, with $\alpha = \{1, 2\}$ be the deterministic scalar observation defined similarly to quantity $Y^{\ell}(j, 2\pi\nu_i, \theta_k)$. Figure 16 displays the graphs of a zoom of $\nu \mapsto y^{\text{type}\,\alpha,\text{lin}}(2\pi\nu_i)$ and $\nu \mapsto y^{\text{type}\,\alpha}(2\pi\nu_i)$. It is clearly seen that the nonlinear and linearized response yield very different dynamical behavior due to the external load level for which geometrical nonlinearities occur. Concerning the nonlinear response, the two tuned configurations do exhibit a complex vibrational behavior, with several resonances in and outside the excitation frequency band, which is of interest for considering the nonlinear detuned optimization. Concerning the linearized response, it is seen that the second resonance for the tuned configuration with blades with type 1 has a response level about 5 times smaller than the main resonance. It is also seen that the first resonance for the tuned configuration with blades with type 2 is not captured because the corresponding natural eigenfrequency is localized below the excitation frequency band. For that reason and for the considered case, it does not seems appropriate to consider linearized detuning optimization and to compare it with the nonlinear detuned optimization.

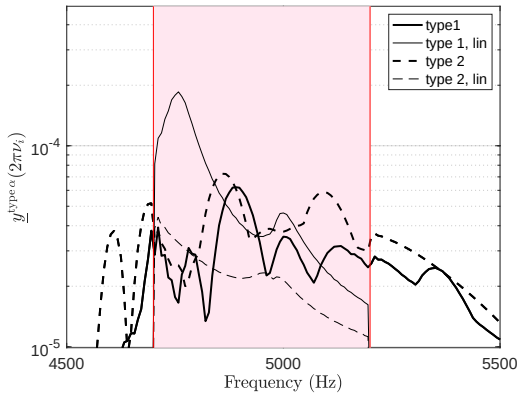

Figure 16: Graph of a zoom of the deterministic response for the nonlinear and linearized response of the tuned configurations with blades of type 1 and of type 2. Graphs of $\nu \mapsto y^{\text{type}\,1}(2\pi\nu_i)$ (thick line), $\nu \mapsto y^{\text{type}\,1,\text{lin}}(2\pi\nu_i)$ (thin line), $\nu \mapsto y^{\text{type}\,2}(2\pi\nu_i)$ (thick dashed line), $\nu \mapsto y^{\text{type}\,2,\text{lin}}(2\pi\nu_i)$ (thin dashed line). Excitation frequency band $\mathbb{B}_e$ is represented by the light pink area.

3.12. Detuned configurations that decrease the amplification of the nonlinear response induced by the mistuning

A detuned configuration ℓ, which yields a nonlinear mistuned response level that is smaller than the one obtained with the tuned configuration in presence of mistuning, is characterized by $q^{c,\ell} < 1$. Such configuration belongs to the set of optimal detuned configurations. In the detuning process, the tuned configuration $\mathbf{w}^{c,\text{t}} = [0\,0\,0\,0\,0\,0\,0\,0\,0\,0\,0\,0]$ in presence of mistuning is considered and yields amplification $q^{c,\text{t}} = 1.0000$. The detuning is defined around this tuned

configuration. This subset corresponds to $n_c = 216$ possible detuned configurations for which the number nb_2 of blades of type 2 is less than or equal to $n_w/2 = 6$ (see Table 4). However, in this paragraph, we will also consider as possible configurations, the detuned configurations around the other tuned configuration $\mathbf{w}^{c,\mathrm{t}_2} = [1\,1\,1\,1\,1\,1\,1\,1\,1\,1\,1\,1]$ corresponding to $\mathrm{nb}_2 > 6$ and for which the amplification factor is $q^{c,\mathrm{t}_2} = 1.1252$. In such a case (see Table 4), there are 136 additional detuned configurations and consequently, the total number of configurations is $n_c = 352$, which are randomly ordered. The tuned configuration $w^{c,t}$ corresponds to $\ell = 49$. Fig. 17 shows the graph of $j \mapsto q^{c,\ell_j}$ where q^{c,ℓ_j} are sorted by increasing order for $n_c = 352$ (upper graph) and for $n_c = 216$ (lower graph). It can be shown that the amplification factor increases from $q^{c,\ell_1} = q^{c,104} = 0.9476$ until $q^{c,\ell_{352}} = q^{c,9} = 1.1774$ corresponding to detuned configurations defined by $\mathbf{w}^{c,104} = [0\,0\,0\,1\,0\,0\,1\,0\,0\,1\,0\,1]$ and $\mathbf{w}^{c,9} = [0\,1\,0\,0\,0\,1\,1\,1\,0\,0\,1\,1]$. By comparing these two graphs, it is shown that only one improving detuned configuration has a number nb_2 of blades with type 2 greater than 6. Furthermore, it is seen that the worst detuned configuration $\ell = 9$ has a number nb_2 of blades with type 2 equal to 6. It can also be seen that most of the detuned configurations having a majority of blades with type 2, have a larger amplification factor.

From now on, only detuned configurations corresponding to $n_c = 216$ possible detuned configurations for which will be considered. With this new renumbering, it can be seen that there are 14 detuned configurations amongst all the 216 detuned configurations (representing 6.5 % of all the detuned configurations) for which the nonlinear mistuned response has smaller response levels than those obtained with the pure mistuning case. Table 5 summarizes the results obtained with these improving detuned configurations. Note that there is only one configuration that presents a subcyclicity with order $s = 2$. The other improving detuned configurations have no particular cyclicity.

Nonlinear detuning optimization in presence of mistuning							
j	ℓ_j	s	nb_1	nb_2	$\mathbf{w}^{c,\ell_j}$	q^{c,ℓ_j}	deterministic detuning q^{c,ℓ_j}_{det}
1	104		8	4	[0 0 0 1 0 0 1 0 0 1 0 1]	**0.9476**	1.0717
2	166		7	5	[1 0 1 1 0 0 1 0 0 1 0 1]	**0.9529**	1.1157
3	123		10	2	[1 0 0 1 0 0 0 0 0 0 0 0]	**0.9537**	1.0504
4	6		9	3	[0 0 0 1 0 1 0 0 0 1 0 0]	**0.9817**	1.0988
5	141		10	2	[1 0 0 0 0 1 0 0 0 0 0 0]	**0.9822**	1.0194
6	133		8	4	[1 0 1 0 0 0 0 0 0 1 0 1]	**0.9824**	1.1610
7	44		10	2	[1 0 1 0 0 0 0 0 0 0 0 0]	**0.9834**	1.1845
8	64		8	4	[0 0 1 0 0 1 1 0 0 1 0 0]	**0.9859**	1.0462
9	34		11	1	[1 0 0 0 0 0 0 0 0 0 0 0]	**0.9882**	1.0852
10	109		7	5	[1 0 1 0 0 1 0 0 1 1 0 0]	**0.9893**	1.3093
11	175		7	5	[1 0 1 0 0 0 1 0 1 1 0 0]	**0.9894**	1.1167
12	64		7	5	[0 0 1 1 0 1 1 0 0 1 0 0]	**0.9974**	0.9799
13	211	2	10	2	[1 0 0 0 0 0 1 0 0 0 0 0]	**0.9995**	0.9788
14	16		6	6	[0 0 1 1 0 1 1 0 1 1 0 0]	**0.9999**	0.9903

Table 5: Characteristics of the the improving detuned configurations.

A careful attention is also paid to the 10 detuned configurations that present a cyclic symmetry $s \in \{2, 3, 4, 6\} < N$. The characteristics are summarized in Table 6 and the corresponding amplification factors are represented by symbols in Fig. 17. As shown in Table 5, except for de-

j	ℓ_j	s	nb_1	nb_2	$\mathbf{w}^{c,\ell_j}$	q^{c,ℓ_j}
87	127	6	6	6	[0 1 0 1 0 1 0 1 0 1 0 1]	1.0757
159	79	4	8	4	[0 1 0 0 1 0 0 1 0 0 1 0]	1.1130
47	45	3	9	3	[0 1 0 0 0 1 0 0 0 1 0 0]	1.0519
164	195	3	6	6	[1 1 0 0 1 1 0 0 1 1 0 0]	1.1141
13	211	2	10	2	[1 0 0 0 0 0 1 0 0 0 0 0]	0.9995
52	152	2	8	4	[0 1 0 1 0 0 0 1 0 1 0 0]	1.0540
90	129	2	8	4	[1 0 0 0 0 1 1 0 0 0 0 1]	1.0766
192	121	2	6	6	[0 1 1 0 0 1 0 1 1 0 0 1]	1.1270
212	164	2	6	6	[0 1 1 0 1 0 0 1 1 0 1 0]	1.1545
213	185	2	6	6	[0 0 1 1 1 0 0 0 1 1 1 0]	1.1573

Table 6: Characteristics of the detuned configurations with a subcyclicity s.

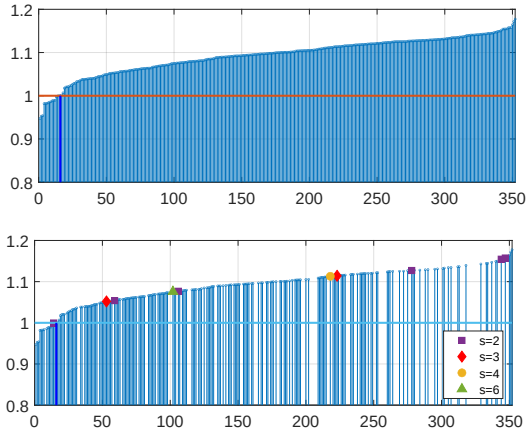

Figure 17: Dynamical amplification factor according to detuned configuration. Graph of function $j \mapsto q^{c,\ell_j}$ for the $n_c = 352$ detuned configurations (upper graph) and for the $n_c = 216$ detuned configurations with a number of blades with type 2 less than or equal to 6 (lower graph). Subcyclicity order s is given for $s = 2$ (purple square symbol), $s = 3$ (red diamond symbol), $s = 4$ (orange bullet symbol) and $s = 6$ (green triangle symbol).

tuned configuration $\ell = 211$ with $s = 2$ that has an amplification factor $q^{c,211} = 0.9995 \simeq 1$ that slightly inhibits the mistuning effects, these subcyclic configurations give rise to an amplification between 5% and 16% with respect to the pure mistuning situation.

3.13. Nonlinear analysis of the mistuned response of the best and the worst detuned configurations

The results are analyzed for the following detuned configurations: the tuned configuration corresponding to the pure mistuning case ($\ell = 49$), the best detuned configuration ($\ell = 104$), and the worst detuned configuration ($\ell = 9$). Fig. 18 displays the graphs of $k \mapsto a^{\ell,k} = A^{\ell}(\theta_k)$ for $k = 1, \ldots, n_{\mathrm{sim}}$, which describes the maximum displacement response over the frequency and the blades for each mistuning realization θ_k of the detuned configurations $\ell \in \{49, 104, 9\}$. By comparing these graphs, it can be seen that the best detuned configuration is characterized

by slightly lower response levels but also by less scattered realizations with respect to the pure mistuned case (left figure). The realizations of the worst detuned configurations (right graph) are clearly more scattered with higher response levels. The distribution of the blades related to these detuned configurations are displayed in Fig. 19. For a given detuned configuration ℓ and a

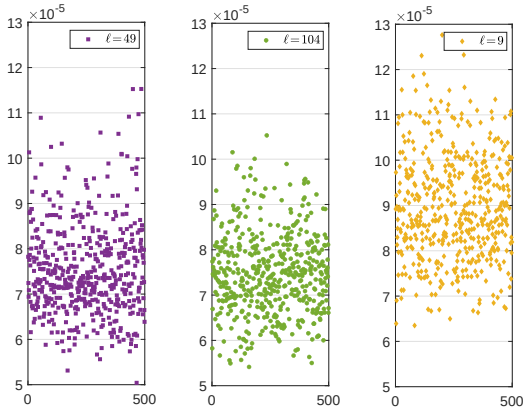

Figure 18: Analysis of the mistuned response for given detuned configurations: graph of realizations $k \mapsto a^{\ell,k} = A^{\ell}(\theta_k)$ for the tuned configuration (pure mistuning) $\ell = 49$ (left figure), the best detuned configuration $\ell = 104$ (middle figure), and the worst detuned configuration $\ell = 9$ (right figure).

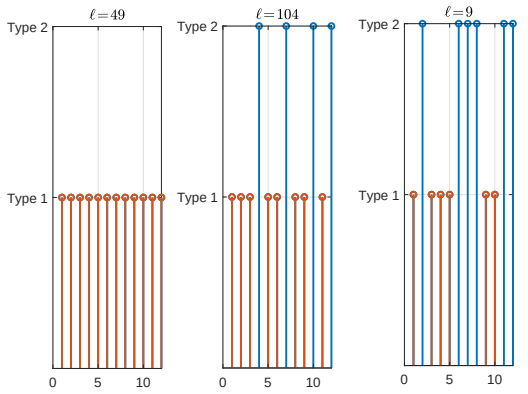

Figure 19: Analysis of the blade distribution corresponding to the pure mistuned configuration (left graph), the best detuned configuration (middle graph), and the worst detuning case (right graph).

fixed frequency ν, we introduce the real-valued random variable $Y^{\ell}_{\max}(2\pi\nu)$ whose realization θ_k is defined by

$$Y^{\ell}_{\max}(2\pi\nu, \theta_k) = Y^{\ell}(j^{\ell,k}_{\max}, 2\pi\nu, \theta_k)\,,$$

in which $j^{\ell,k}_{\max}$ is defined by Eq. (37). For detuned configurations $\ell \in \{49, 104, 9\}$, Figs. 20 to 22 display the graphs of the confidence region of the real-valued random function $\nu \mapsto Y^{\ell}_{\max}(2\pi\nu)$ for a probability level of 0.98. As expected, it can be seen that the structural displacements are

mainly located in the frequency band of excitation $\mathbb{B}_e$ but that there are also new resonances occurring below the frequency band of excitation $\mathbb{B}_e$ that are induced by the geometrical nonlinearities. The amplitudes of these new resonances correspond to the indirect excitation of the first blade modes of the blisk and are of a lower order of magnitude in the present case, probably because the blades are not very slender. Note that this phenomenon has already been observed in previous analyses of nonlinear mistuned blisk for which the blades were slender structures, attached to the disk [36, 47]. Moreover, the phenomenon for which the amplitude of the resonances located below the frequency band of excitation are dominant has been investigated in another context of sloshing in nonlinear fluid structure interaction [60]. Fig. 23 shows a zoom of these confidence regions around the excitation frequency band $\mathbb{B}_e$. It is clearly seen that the pure mistuned blisk have slightly more robust resonances that the one obtained with the detuned configurations in presence of mistuning. But the real interest is to verify that the optimal detuned configuration (middle graph) guarantees that the upper envelope of the confidence region stays below the critical level of response of the pure mistuned response. It is thus observed that the optimal detuned configuration yields a reduction of the maximum amplitude of about 12% with respect to the initial situation that corresponds to the pure mistuning case. Another observation is that the worst detuned configuration yields an amplification of about 11% with respect to the initial situation that corresponds to the pure mistuning case. Note that the resonance involved does not correspond to the main resonance of the pure mistuned system. All these observations allow for assessing the efficiency of the optimization through the output of interest $q^{c,\ell}$.

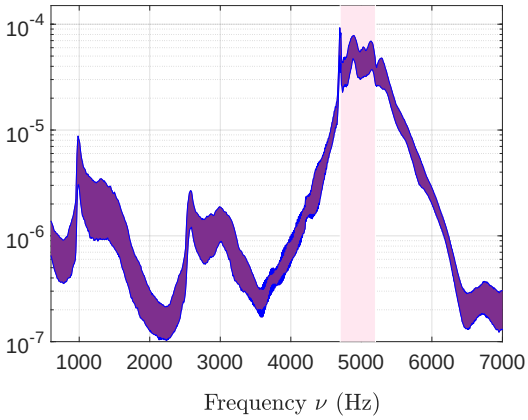

Figure 20: Analysis of the mistuned response for the tuned configuration: graph of the confidence region of $\nu \mapsto Y^{\ell}_{\max}(2\pi\nu)$ for a probability level of 0.98, corresponding to the pure mistuned configuration $\ell = 49$ (purple area). Excitation frequency band $\mathbb{B}_e$ is represented by the light pink area.

3.14. Sensitivity analysis of the nonlinear mistuned response of the best and the worst detuned configurations with respect to the detuning rate and the mistuning rate

It is interesting to perform a sensitivity analysis with respect to the detuning rate for the 3 configurations studied in Section 3.13. The detuning rate is described by the ratio r defined by

$$r = 1 - \sqrt{\frac{\text{Young}_2}{\text{Young}_1}} \quad . \tag{39}$$

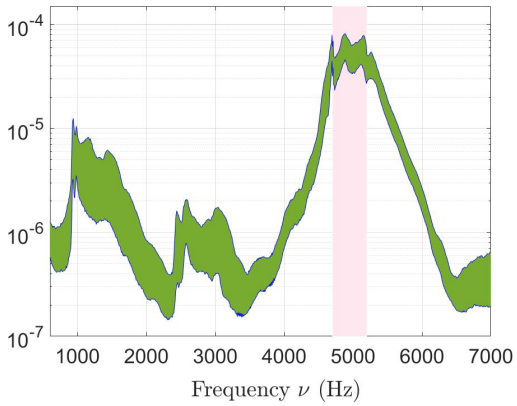

Figure 21: Analysis of the mistuned response for given detuned configurations: graph of the confidence region of $\nu \mapsto Y^{\ell}_{\max}(2\pi\nu)$ for a probability level of 0.98, corresponding to the best detuned configuration $\ell = 104$ (green area). Excitation frequency band $\mathbb{B}_e$ is represented by the light pink area.

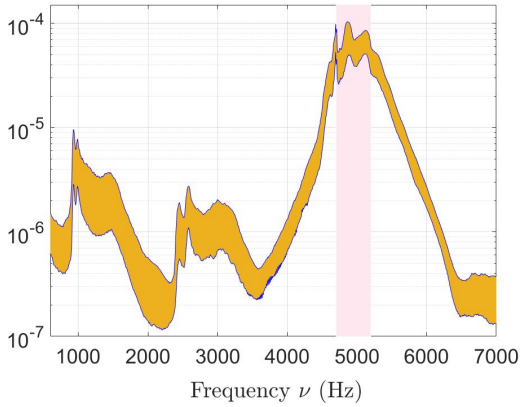

Figure 22: Analysis of the mistuned response for given detuned configurations: graph of the confidence region of $\nu \mapsto Y^{\ell}_{\max}(2\pi\nu)$ for a probability level of 0.98, corresponding to the worst detuned configuration $\ell = 9$ (orange area). Excitation frequency band $\mathbb{B}_e$ is represented by the light pink area.

It quantifies a ratio for the blade frequency. In this Section, observation $q^{c,\ell}$ is parameterized as a function of r and δ_K and is rewritten as $q^{c,\ell}(r;\delta_K)$. All the optimization process has been carried out for the constant mistuning defined by $\delta_K = 0.1$ and for a detuning rate $r = 5.13\,\%$ corresponding to blade Young modulus $\text{Young}_2 = 1.80\times10^{11}\,\text{N/m}^2$. The performed sensitivity analysis involves a blade Young modulus $\text{Young}_2 \in [1.70, 2.00]\times10^{11}\,\text{N/m}^2$ corresponding to $r \in [0, 7.8]\,\%$. The graph $r \mapsto q^{c,\ell}(r; 0.1)$ is shown in Fig. 24. The purple line describes the pure mistuning case taken as a reference and yielding $q^{c,49}(0, 0.1) = 1$. As expected, the two investigated detuned configurations ($\ell = 9$ and 104) tend to converge to the pure mistuned situation as r goes to zero. Note that the few fluctuations at $r = 0$ are caused by the statistical post-processing. The optimal detuned configuration $\ell = 104$ further reduces the amplification when the detuning rate is $r = 4.34\,\%$ corresponding to $\text{Young}_2 = 1.83\times10^{11}\,\text{N/m}^2$ yielding

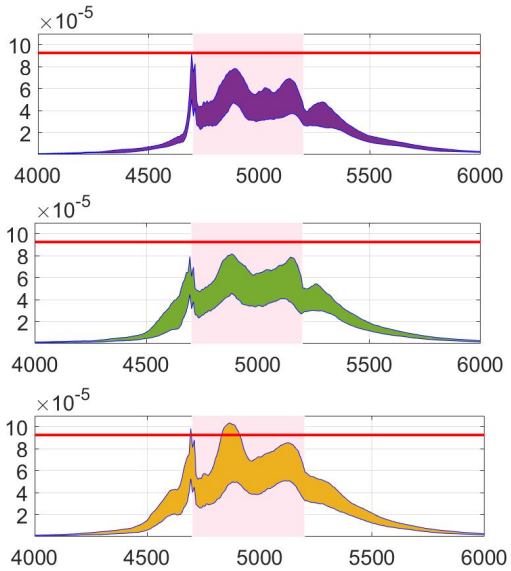

Figure 23: Analysis of the mistuned response for given detuned configurations: for a probability level of 0.98, zoom of the confidence region of $\nu \mapsto Y^{\ell}_{\max}(2\pi\nu)$ for the pure mistuned configuration $\ell = 49$ (upper graph), for the best detuned configuration $\ell = 104$ (middle graph), and for the worst detuned configuration $\ell = 9$ (lower graph). Critical level defined by the maximum of the upper envelope corresponding to the pure mistuned situation (red line).

$q^{c,\ell}(r = 4.34\,\%, 0.1) = 0.9394$. Note that this optimum is not necessarily a global optimum since the optimization has been carried out for $r = 5.13\,\%$. Moreover, it can also be seen that detuned configuration $\ell = 104$ does not behave monotonically with respect to inhibition or amplification induced by the mistuning. There is a range of detuning rate $r \in [3.30, 6.99]\,\%$ for which the detuned configuration reduces the amplification induced by the mistuning. But we have to carefully pay attention not to have a detuning rate r smaller than $3.30\,\%$. Note also that the detuned configuration $\ell = 9$ corresponding to the worst detuned configuration in the optimization process increases the amplification induced by the mistuning whatever the detuning rate r. Then a sensitivity analysis is performed for these three detuned configurations with respect to the mistuning rate δ_K, which is the hyperparameter that calibrates the uncertainty level in meta-stiffness matrix (See Section 2.4), and which contains both linear and nonlinear stiffness contributions. It is interesting to relate it to physical considerations. For instance, in the pure mistuning case and for a mistuning rate $\delta_K = 0.1$, the confidence region obtained with a probability level of 98% and related to the location of the main resonance is described by a dispersion between $-1.76\,\%$ and $+5.59\,\%$ around the main resonance. The performed sensitivity analysis involves a mistuning rate from $\delta_K \in [0, 0.24]$. The graph $\delta_K \mapsto q^{c,\ell}(5.13\,\%; \delta_K)$ is shown in Fig. 25. The purple line describes the pure mistuning case taken as a reference and yielding $q^{c,49} = 1$. The detuned configuration $\ell = 9$ never improves the mistuning situation whatever the mistuning rate. Concerning detuned configuration $\ell = 104$ that is optimal for a mistuning rate $\delta_K = 0.1$, there is a threshold value $\delta_K = 0.08$ from which the mistuning amplification effects are inhibited with respect to the pure mistuning situation. A remark concerns the deterministic detuning optimization. It can be seen that neither detuned configurations $\ell = 9$ or $\ell = 104$ allows for inhibiting the mistuning amplification effects as deterministic detuning is considered. Although deterministic optimization

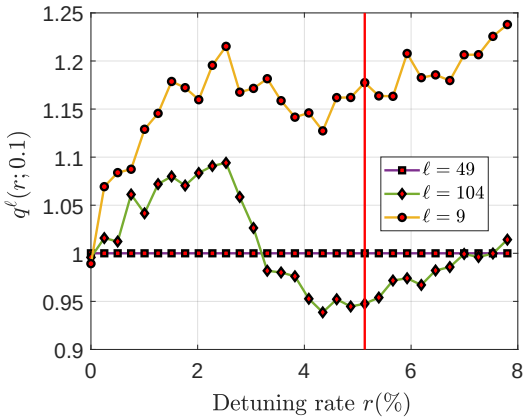

Figure 24: Analysis of the sensitivity of mistuned response for given detuned configurations with respect to the detuning rate r: graph of $r \mapsto q^{c,\ell}(r;0.1)$ for the pure mistuned situation corresponding to $\ell = 49$ (square symbol, purple line), for the best detuned configuration $\ell = 104$ (diamond symbol, green line), and for the worst detuned configuration $\ell = 9$ (circle symbol, orange line). Parameters for optimization process (vertical red line).

has no meaning because mistuning is an unavoidable phenomenon, it has also been performed and the results show that the optimal solutions are not optimal for the detuning optimization in presence of mistuning. Let $q_{det}^{c,\ell}$ be the corresponding quantity of interest related to $q^{c,\ell}$ when considering deterministic detuning (that is to say without mistuning). Table 7 displays the seven optimal deterministic detuned configurations and compares the quantity of interest when detuning optimization is carried out in presence of mistuning. It can be seen that three optimal deterministic detuned configurations belong to the set of the fourteen optimal detuned configurations (in presence of mistuning) but that such detuned configurations are in fact part of the less optimal configurations since the corresponding quantity $q^{c,\ell}$ is close to 1. Table 5 also compares the quantity of interest of the detuning optimization with those obtained when no mistuning is considered. It is interesting to see that such quantity is sensitive to the presence of mistuning. This proves that mistuning cannot be neglected in the detuning optimization process. The most optimal detuned configurations are not optimal solutions when no mistuning is considered in the detuning optimization process.

Nonlinear deterministic detuning optimization (without mistuning)							
j	ℓ_j	s	nb_1	nb_2	$\mathbf{w}^{c,\ell_j}$	deterministic detuning q_{det}^{c,ℓ_j}	q^{c,ℓ_j}
39	145		7	5	[0 0 1 1 0 0 1 0 0 0 1 1]	*0.9574*	1.0444
68	189		7	5	[0 0 1 1 0 1 1 1 0 0 0 0]	*0.9675*	1.0627
192	121		6	6	[0 1 1 0 0 1 0 1 1 0 0 1]	*0.9727*	1.1270
13	211	2	10	2	[1 0 0 0 0 0 1 0 0 0 0 0]	*0.9788*	0.9995
12	64		7	5	[0 0 1 1 0 1 1 0 0 1 0 0]	*0.9800*	0.9974
27	162		7	5	[1 1 0 0 0 0 0 1 0 1 1 0 0]	*0.9872*	1.0329
14	16		6	6	[0 0 1 1 0 1 1 0 1 1 0 0]	*0.9903*	0.9999

Table 7: Characteristics of the the improving deterministic detuned configurations without mistuning

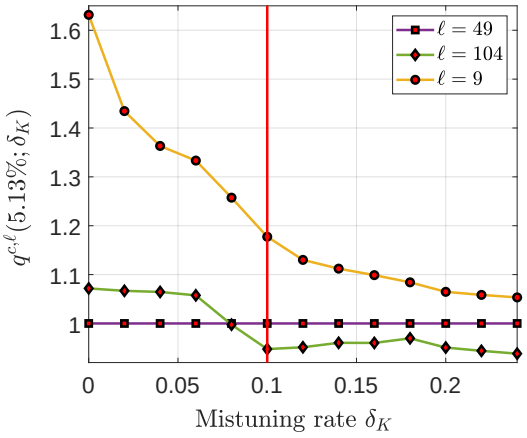

Figure 25: Analysis of the sensitivity of mistuned response for given detuned configurations with respect to the mistuning rate δ_K: graph of $\delta_K \mapsto q^{c,\ell}(5.13\,\%;\delta_K)$ for the pure mistuned situation corresponding to $\ell = 49$ (square symbol, purple line), for the best detuned configuration $\ell = 104$ (diamond symbol, green line), and for the worst detuned configuration $\ell = 9$ (circle symbol, orange line). Parameters for optimization process (vertical red line).

4. Optimization of the detuning in presence of mistuning using probabilistic learning on manifolds (PLoM) as a machine learning tool

4.1. Discrete set $\mathcal{N}_c$ of a configuration

We consider the detuning of a blisk as the one analyzed in Section 3 having n_w blades and two types of blades that are labelled by integer 0 and 1. A configuration (also called a pattern) of the blisk consists in giving a vector

$$\mathbf{w}^c = (w_1^c, \ldots, w_{n_w}^c)\,, \tag{40}$$

in which for $k \in \{1, \ldots, n_w\}$, w_k^c is equal to 0 or to 1. We then define the finite subset $\mathcal{N}_c$ of $\mathbb{N}^{n_w}$ such that

$$\mathcal{N}_c = \Pi_{k=1}^{n_w} \{0, 1\}^{n_w} \subset \mathbb{N}^{n_w}\,, \tag{41}$$

and consequently, $\mathbf{w}^c \in \mathcal{N}_c$.

4.2. Discrete set $\mathcal{C}_c$ of the n_c possible configurations

The total number of all the possible configurations is denoted by n_c. As already explained in Section. 2.5, n_c can be very large as soon as n_w is large. By excluding the rotations by an integer number of blades, the asymptotic value of n_c is $n_c = (2^{n_w})/n_w$. For instance, if $n_w = 48$, then $n_c = 5.86 \times 10^{12}$. This asymptotic formula includes the configuration with n_w blades of type 0 and the configuration with n_w blades of type 1. If the configurations are restricted to the case for which the number of blades of type 1 is less than or equal to $n_w/2$, then $n_c < (2^{n_w})/n_w$. It will be the case for the configurations of the detuned blisk considered in this section, for which $n_w = 12$ and therefore, $n_c = 216$ (see also Section 3.9).

The finite set $\mathcal{C}_c$ of the n_c possible configurations is defined by

$$\mathcal{C}_c = \{\mathbf{w}^{c,1}, \ldots, \mathbf{w}^{c,n_c}\}\,,\ \mathbf{w}^{c,\ell} \in \mathcal{N}_c\,. \tag{42}$$

4.3. Quantity of interest (QoI) computed for a given configuration

For a given configuration $\mathbf{w}^c \in \mathcal{N}_c$, the HFCM is used (see Section 3) for computing the QoI that is the dynamic amplification factor $q^c \in \mathbb{R}$ (defined by Eq. (38)) of the detuned disk in presence of random mistuning. Consequently, there exists a mapping $\mathbf{w}^c \mapsto f_{\text{HFCM}}(\mathbf{w}^c)$ defined on $\mathcal{N}_c$ with values in $\mathbb{R}$ such that

$$q^c = f_{\text{HFCM}}(\mathbf{w}^c)\,. \tag{43}$$

Mapping f_{HFCM} is completely defined by the set $\{(q^{c,\ell}, \mathbf{w}^{c,\ell}), \ell = 1, \ldots, n_c\}$ of the n_c points in $\mathbb{R} \times \mathcal{N}_c$ in which $q^{c,\ell} = f_{\text{HFCM}}(\mathbf{w}^{c,\ell})$ with $\mathbf{w}^{c,\ell} \in \mathcal{C}_c$.

4.4. Definition of a combinatorial optimization problem on finite set $\mathcal{C}_c$

Such a combinatorial optimization problem [61, 62, 63] on finite set $\mathcal{C}_c$ would consist in finding $\mathbf{w}_{\text{un}}^{c,\text{opt}} \in \mathcal{N}_c$ such that

$$\mathbf{w}_{\text{un}}^{c,\text{opt}} = \arg \min_{\mathbf{w}^c \in \mathcal{C}_c} \mathcal{J}_c(\mathbf{w}^c)\,, \tag{44}$$

in which $\mathbf{w}^c \mapsto \mathcal{J}_c(\mathbf{w}^c)$ is chosen for minimizing the dynamic amplification factor defined by Eq. (43), that is to say,

$$\mathcal{J}_c(\mathbf{w}^c) = f_{\text{HFCM}}(\mathbf{w}^c) \quad , \quad \mathbf{w}^c \in \mathcal{N}_c\,. \tag{45}$$

(i) The exhaustive search of the combinatorial optimization problem on finite set $\mathcal{C}_c$, defined by Eqs. (44)-(45), is not tractable and unachievable for large value of n_c. There are many methods in the literature for solving such a problem: the theory of linear programming [64] including the polynomial-time algorithms [65], integer programming [66] that deals with graph structures [67], the operations research [68], and the computational complexity theory [69]. Certainly, the most popular methods are the branch-and-bound [70], the branch-and-cut [71], the tabu search and greedy [72], and the dynamic programming [73].

(ii) When the numerical cost for the evaluation of $\mathcal{J}_c(\mathbf{w}^c)$ at any point $\mathbf{w}^v$ in $\mathcal{C}_c$ is negligible, then the previous listed methods and algorithms can be used for estimating an optimal solution.

(iii) The specificity of the combinatorial optimization problem under consideration is the high numerical cost of one evaluation $q^{c,\ell} = f_{\text{HFCM}}(\mathbf{w}^{c,\ell})$ using HFCM. In practice, only $N_d \ll n_c$ evaluations can be carried out (for instance, $N_d = 50$ or 100 while n_c can be 10^{12}). We therefore need to construct a metamodel of $\mathcal{J}_c$ for computing $\mathcal{J}_c(\mathbf{w}^c)$ for any $\mathbf{w}^c$ proposed by the optimization algorithm in order that each evaluation has a negligible numerical cost. We propose to use a machine learning tool for evaluating $\mathcal{J}_c(\mathbf{w}^c)$ for any $\mathbf{w}^c$ in $\mathcal{C}_c$.

4.5. Transforming the combinatorial optimization problem in another one adapted to probabilistic machine learning tools

The combinatorial optimization problem defined by Eqs. (44)-(45) is reformulated in a probabilistic framework, which will be adapted to a machine learning solver in order to limit the number of evaluations using HFCM.

Let $\mathbf{W}^c = (W_1^c, \ldots, W_{n_w}^c)$ be the $\mathcal{N}_c$-valued random variable, defined on a probability space $(\Theta, \mathcal{T}, \mathcal{P})$, for which the n_c elements $\mathbf{w}^{c,1}, \ldots \mathbf{w}^{c,n_c}$ of $\mathcal{C}_c$ are n_c independent realizations. Let Q^c be the real-valued random variable, defined on $(\Theta, \mathcal{T}, \mathcal{P})$ such that

$$Q^c = f_{\text{HFCM}}(\mathbf{W}^c)\,. \tag{46}$$

Consequently, $\{q^{c,\ell} = f_{\text{HFCM}}(\mathbf{w}^{c,\ell}), \ell = 1, \dots, n_c\}$ is the set of the n_c realizations of Q^c. The optimization problem defined by Eqs. (44)-(45) is then replaced by the following one: find $\mathbf{w}^{c,\text{opt}} \in \mathcal{N}_c$ such that

$$\mathbf{w}^{c,\text{opt}} = \arg \min_{\mathbf{w}^c \in \mathcal{C}_c} J_c(\mathbf{w}^c)\,, \tag{47}$$

in which the cost function $\mathbf{w}^c \mapsto J_c(\mathbf{w}^c)$ is chosen as the conditional mathematical expectation of Q^c given $\mathbf{W}^c = \mathbf{w}^c$,

$$J_c(\mathbf{w}^c) = E\{Q^c \,|\, \mathbf{W}^c = \mathbf{w}^c\} \quad , \quad \mathbf{w}^c \in \mathcal{N}_c\,. \tag{48}$$

For $\mathbf{w}^{c,\ell} \in \mathcal{C}_c$, the conditional random variable $\{Q^c \,|\, \mathbf{W}^c = \mathbf{w}^{c,\ell}\}$ is equal to the deterministic value $q^{c,\ell} = f_{\text{HFCM}}(\mathbf{w}^{c,\ell})$. We thus have $J_c(\mathbf{w}^{c,\ell}) = \mathcal{J}_c(\mathbf{w}^{c,\ell})$ for $\ell \in \{1, \dots, n_c\}$, which proves that Eqs. (47)-(48) is a rewriting of Eqs. (44)-(45) for $\mathbf{w}^c \in \mathcal{C}_c$. Therefore, this optimization problem is still a combinatorial optimization problem, but $J_c(\mathbf{w}^c)$ will be computed using a probabilistic machine learning tool.

4.6. Definition of the training set $\mathcal{D}_d$ and learned set $\mathcal{D}_{\text{ar}}$ for a probabilistic machine learning tool

Taking into account Section 4.5, we will use a probabilistic machine learning tool for constructing a probabilistic metamodel of cost function J_c in order to avoid a large number of evaluations of $J_c(\mathbf{w}^c)$ with HFCM for $\mathbf{w}^c \in \mathcal{C}_c$.

(i) Training set $\mathcal{D}_d$. The first step consists in generating the training set $\mathcal{D}_d$ by using HFCM. Training set $\mathcal{D}_d$ is made up of N_d points $(q^{c,\ell}, \mathbf{w}^{c,\ell})$ such that $q^{c,\ell} = f_{\text{HFCM}}(\mathbf{w}^{c,\ell})$ for $\ell \in \{1, \dots, N_d\}$ with $N_d \ll n_c$. This means that the construction of $\mathcal{D}_d$ requires N_d calls to HFCM, and consequently, N_d will be small. The training set is therefore, by hypothesis, a small data set (in opposite to a big data set that is generally requires for the machine learning algorithms).

(ii) Learned set $\mathcal{D}_{\text{ar}}$. The second step will thus consist in using a machine learning method for generating, from the training set $\mathcal{D}_d$, the learned set $\mathcal{D}_{\text{ar}}$ made up of N_{ar} learned realizations $\{(q^\ell_{\text{ar}}, \mathbf{w}^\ell_{\text{ar}}), \ell = 1, \dots, N_{\text{ar}}\}$ of an $\mathbb{R} \times \mathbb{R}^{n_w}$-valued random variable $(Q, \mathbf{W})$ (defined in Section 4.7) without calling HFCM. The number N_{ar} of points is chosen sufficiently large ($N_{\text{ar}} \gg N_d$) to obtain a converged estimate of the conditional expectation introduced in Eq. (48) for computing $J_c(\mathbf{w}^c)$ for any $\mathbf{w}^c \in \mathcal{C}_c$ (see Eq. (42)). So $\mathcal{D}_{\text{ar}}$ can be viewed as a big data set.

4.7. Probabilistic learning on manifolds (PLoM) used as a machine learning tool and approximate combinatorial optimization problem

There are many methods available in the literature for building metamodels. Each method has its own validity assumptions with respect to the input-output dimensions, the complexity of the function to be represented, the number of points in the training set (small or big), the presence or not of uncertainties, a formulation performed in a deterministic or stochastic framework. It is not possible here to propose a review of all these methods, knowing that the use of each requires a precise analysis of its domain of validity, which depends on the hypotheses with which it was constructed. Nevertheless, we refer the reader to [74] for methods based on probability theory and mathematical statistics, including polynomial chaos expansion methodology, to [75, 76, 77, 78, 79, 80] for surrogate based modeling, to [81, 82, 83, 27, 84, 85, 86, 87, 88] for projection-based model reduction, and to [89, 90, 91, 92, 93] for optimization of expensive functions.

The specific difficulty of the problem considered here is the small number of points available in training set $\mathcal{D}_d$ (a few tens or even hundreds for industrial turbomachinery problems) and the

complexity of the function f_{HFCM}. For instance, the very efficient ANN approach [94] cannot be used, *a priori*, for constructing a metamodel of J_c because N_d is too small. There are methods for sampling underlying distributions on manifolds [95, 96, 97, 98, 99, 100, 101, 102]. Among all these existing methods in machine learning, there is the probabilistic learning method (PLoM), which has specifically been developed for small non-Gaussian data (small value of N_d) in arbitrary dimension [103, 104, 105], with the possibility to take into account additional constraints coming from experiments [106] or from nonlinear partial differential equations [107], to construct a polynomial chaos representation of databases on manifolds [77], to construct Bayesian posteriors in high dimension [108], and which has been used for complex optimization problems under uncertainties [93, 109] and challenging applications [110, 111, 112].

(i) Generating the learned set $\mathcal{D}_{\mathrm{ar}}$ with the PLoM method. We thus propose to use the PLoM method for generating the learned set $\mathcal{D}_{\mathrm{ar}}$ from the training set $\mathcal{D}_d$. The PLoM method is adapted to a continuous random variable $\mathbf{X} = (Q, \mathbf{W})$, defined on $(\Theta, \mathcal{T}, \mathcal{P})$, with values in $\mathbb{R}^n = \mathbb{R} \times \mathbb{R}^{n_w}$ with $n = 1 + n_w$, while the combinatorial optimization problem defined by Eqs. (47)-(48) is related to the random variable $\mathbf{X}^c = (Q^c, \mathbf{W}^c)$, in which $Q^c = f_{\mathrm{HFCM}}(\mathbf{W}^c)$ (see Eq. (46)) and where $\mathbf{W}^c$ is a random variable with values in a finite set $\mathcal{N}_c$. From the training set $\mathcal{D}_d = \{(q^{c,\ell}, \mathbf{w}^{c,\ell}), \ell = 1, \ldots, N_d\}$, the PLoM method is used for generating the learned set $\mathcal{D}_{\mathrm{ar}} = \{(q^{\ell}_{\mathrm{ar}}, \mathbf{w}^{\ell}_{\mathrm{ar}}), \ell = 1, \ldots, N_{\mathrm{ar}}\}$.

In order to facilitate the reading of this paper, the reader will find in Section A.1 of Appendix A a summary of the PLoM algorithm. We give this summary, because the proposed algorithm is the assembly of ingredients, which are distributed in three different papers with slightly different notations: basic algorithm of PLoM [103, 104], novel algorithm to estimate the optimal value of the parameter of the kernel for the calculation of the diffusion-maps basis [105], and taking into account of the normalization constraints [106].

(ii) Approximate combinatorial optimization problem. In order to use the learned set $\mathcal{D}_{\mathrm{ar}}$, we introduce the following approximation of the combinatorial optimization problem defined by Eqs. (47)-(48): find $\mathbf{w}^{\mathrm{opt}}$ in $\mathcal{N}_c$ such that

$$\mathbf{w}^{\mathrm{opt}} = \arg \min_{\mathbf{w}^c \in \mathcal{C}_c} J_{\mathrm{ar}}(\mathbf{w}^c)\,, \tag{49}$$

in which the learned cost function $\mathbf{w}^c \mapsto J_{\mathrm{ar}}(\mathbf{w}^c)$ is defined by

$$J_{\mathrm{ar}}(\mathbf{w}^c) = E\{Q \,|\, \mathbf{W} = \mathbf{w}^c\} \quad , \quad \mathbf{w}^c \in \mathcal{N}_c\,, \tag{50}$$

in which $(Q, \mathbf{W})$ is the random variable with values in $\mathbb{R} \times \mathbb{R}^{n_w}$, which approximates (for the learning step) random variable $(Q^c, \mathbf{W}^c)$ with values in $\mathbb{R} \times \mathcal{N}_c$ and for which the learned realizations are $\{(q^{\ell}_{\mathrm{ar}}, \mathbf{w}^{\ell}_{\mathrm{ar}}), \ell = 1, \ldots, N_{\mathrm{ar}}\}$. Since random variable $(Q, \mathbf{W})$ has been defined by its learned realizations, the joint probability density function $p_{Q,\mathbf{W}}$ of $(Q, \mathbf{W})$ on $\mathbb{R} \times \mathbb{R}^{n_w}$ will be constructed by using the multidimensional Gaussian Kernel Estimation (KDE) method with the learned realizations of $\mathcal{D}_{\mathrm{ar}}$ (thus this pdf exists by construction, see Section 4.8). With such a hypothesis, the right-hand side of Eq. (50) can be written as

$$E\{Q|\mathbf{W}=\mathbf{w}^c\} = \frac{1}{p_{\mathbf{W}}(\mathbf{w}^c)} \int_{\mathbb{R}} q\, p_{Q,\mathbf{W}}(q, \mathbf{w}^c)\, dq, \tag{51}$$

in which $p_{\mathbf{W}}(\mathbf{w}^c) = \int_{\mathbb{R}} p_{Q,\mathbf{W}}(q, \mathbf{w}^c)\, dq$.

(iii) Difficulties induced by the fluctuations (variations) of the cost function. There is still a difficulty with the combinatorial optimization problem defined by Eqs. (49)-(50), induced by the physics of the nonlinear stochastic dynamics of detuned bladed-disks in presence of random mistuning. Function $\mathbf{w}^c \mapsto f_{\text{HFCM}}(\mathbf{w}^c)$ defined for $\mathbf{w}^c \in C_c$ has many local minima with very close values (very similar dynamic amplification factor $q^c = f_{\text{HFCM}}(\mathbf{w}^c)$ for many different configurations $\mathbf{w}^c$). This implies that function $\mathbf{w} \mapsto J_{\text{ar}}(\mathbf{w})$ defined by Eq. (50) and extended on $\mathbb{R}^{n_w}$, is not convex on $\mathbb{R}^{n_w}$, and has also many local minima with very close values.

(iv) Reformulation of the combinatorial optimization problem. Taking into account the need to introduce the approximation defined by Eq. (50) to build a metamodel of cost function J_{ar} and taking into account the specificities of its fluctuations (variations) involved by physics, the formulation defined by Eqs. (49)-(50) is not suitable and must be adapted. Estimating a single optimal configuration $\mathbf{w}^{\text{opt}}$, which yields the smallest dynamic amplification factor, is not sufficiently robust. We therefore propose to reformulate Eq. (49) as follows.

Subset $\mathcal{W}_{n_s}^{\text{opt}}$ of optimal solutions. Let $n_s \ll n_c$ be an integer that is fixed *a priori* (chosen as a few units). Let $\mathcal{W}_{n_s}^{\text{opt}}$ be the subset of C_c made up of the n_s configurations $\mathbf{w}^{c,\ell_1}, \ldots, \mathbf{w}^{c,\ell_{n_s}}$ in C_c with $\{\ell_1, \ldots, \ell_{n_s}\} \subset \{1, \ldots, n_c\}$, which correspond to the n_s first smallest values $J_{\text{ar}}(\mathbf{w}^{c,\ell_1}), \ldots, J_{\text{ar}}(\mathbf{w}^{c,\ell_{n_s}})$ of the set $\{J_{\text{ar}}(\mathbf{w}^c), \mathbf{w}^c \in C_c\}$. We then have,

$$\mathcal{W}_{n_s}^{\text{opt}} = \{\mathbf{w}^{c,\ell_1}, \ldots, \mathbf{w}^{c,\ell_{n_s}}\} \subset C_c \,, \tag{52}$$

$$J_{\text{ar}}(\mathbf{w}^{c,\ell_1}) \leq J_{\text{ar}}(\mathbf{w}^{c,\ell_2}) \leq \ldots \leq J_{\text{ar}}(\mathbf{w}^{c,\ell_{n_s}}) \,. \tag{53}$$

The subset of optimal solutions of the combinatory optimization problem is therefore defined as the subset $\mathcal{W}_{n_s}^{\text{opt}}$ of C_c.

(v) Convergence analysis of the subset of optimal solution. Since the conditional mathematical expectation in Eq. (50) will be estimated with the N_{ar} points of the learned set $\mathcal{D}_{\text{ar}}$, the subset of optimal solution $\mathcal{W}_{n_s}^{\text{opt}}$ depends on N_{ar} and will be rewritten as $\mathcal{W}_{n_s}^{\text{opt}}(N_{\text{ar}})$ when necessary. A convergence analysis will be carried out in Section 4.10 with respect to $N_{\text{ar}} \gg N_d$.

(vi) Searching a best optimal configuration in the subset $\mathcal{W}_{n_s}^{\text{opt}}$ of optimal solutions. The hypotheses for constructing the best optimal configuration are the following.

(H1) The number N_d of points in the training set is fixed. This number corresponds to the maximum numerical effort that can be made for performing N_d calls to HFCM. As N_d is assumed to be small, convergence with respect to N_d has no object. Once set N_d, we seek to improve the values of the dynamic amplification factors that have been computed with HFCM for constructing the training set.

(H2) Let us assume that N_d and N_{ar} are fixed. As previously explained, taking into account the complexity of the variations of function f_{HFCM}, which is not explicitly known in C_c, but only point-by-point using HFCM, it is not possible to demonstrate that subset $\mathcal{W}_{n_s}^{\text{opt}}(N_{\text{ar}})$ contains an optimal configuration that improves the dynamic amplification factors computed for constructing the training set $\mathcal{D}_d$. The only way to do this is to compute again, with HFCM,

$$\mathcal{J}_c(\mathbf{w}^{c,\ell_1}), \ldots, \mathcal{J}_c(\mathbf{w}^{c,\ell_{n_s}}) \,, \tag{54}$$

for the n_s configurations of subset $\mathcal{W}_{n_s}^{\text{opt}}(N_{\text{ar}})$, which have been identified by PLoM (see Eqs. (52)-(53)). Therefore, we define the configuration $\mathbf{w}^{c,\ell_{\text{opt}}}$ with $\ell_{\text{opt}} \in \{\ell_1, \ldots, \ell_{n_s}\}$ as the one that satisfies,

$$\mathbf{w}^{c,\ell_{\text{opt}}} = \arg \min_{\mathbf{w}^{c,\ell_j},\, j=1,\ldots,n_s} \{\mathcal{J}_c(\mathbf{w}^{c,\ell_1}), \ldots, \mathcal{J}_c(\mathbf{w}^{c,\ell_{n_s}})\}. \tag{55}$$

(H3) *Definition of the best optimal configuration*. Let n_s be fixed and let $\mathbf{w}^{c,\ell_{\text{opt}}}$ be the configuration identified by Eq. (55) . If we have

$$\mathcal{J}_c(\mathbf{w}^{c,\ell_{\text{opt}}}) < \min_{\ell=1,\ldots,N_d} f_{\text{HFCM}}(\mathbf{w}^{c,\ell})\,, \tag{56}$$

then $\mathbf{w}^{c,\ell_{\text{opt}}}$ is identified as the optimal configuration in $\mathcal{W}_{n_s}^{\text{opt}}(N_{\text{ar}})$, which is better than all the configurations $\{\mathbf{w}^{c,\ell}, \ell = 1,\ldots,N_d\}$ used for constructing the training set $\mathcal{D}_d$.

(H4) If Eq. (56) does not hold, that is to say, a configuration has not be found for improving the knowledge corresponding to the training set, then we can:

(a) Increase the value of n_s (N_d remaining fixed at its value). Note that the value of n_s should be kept small because the number of evaluations with HFCM is n_s.

(b) If (a) is not a success, this means that the value of N_d is not large enough for obtaining a good learned set $\mathcal{D}_{\text{ar}}$ from the training set $\mathcal{D}_d$. It is then necessary to increase the value of N_d.

(c) It should be noted that to build the learned set from the training set, the PLoM algorithm is initialized with the points of the training set, which means that the points of the training set belong also to the learned set. Consequently, if the best optimal configuration belongs to the training set, then this optimal configuration will be identified with Eq. (56).

4.8. Estimating the cost function using the learned set

As explained in Section 4.7-(i), the PLoM method allows for generating $N_{\text{ar}} \gg N_d$ realizations $\{\mathbf{x}_{\text{ar}}^{\ell}, \ell = 1,\ldots,N_{\text{ar}}\}$ with $\mathbf{x}_{\text{ar}}^{\ell} = (q_{\text{ar}}^{\ell}, \mathbf{w}_{\text{ar}}^{\ell})$ of random variable $\mathbf{X} = (Q, \mathbf{W})$ with values in $\mathbb{R}\times\mathbb{R}^{n_w}$, $n = 1 + n_w$, without calling HFCM. The classical Gaussian KDE method of the pdf $\mathbf{x} \mapsto p_{\mathbf{X}}(\mathbf{x})$ on $\mathbb{R}^n$ of random variable $\mathbf{X}$, with respect to the Lebesgue measure $d\mathbf{x}$, is written [113, 114, 115, 116] as

$$p_{\mathbf{X}}(\mathbf{x}) = \frac{1}{N_{\text{ar}}}\sum_{\ell=1}^{N_{\text{ar}}} \frac{1}{(\sqrt{2\pi}s_{\text{SBX}})^n \sigma_1\ldots\sigma_n} \times \exp\{-\frac{1}{2s_{\text{SBX}}^2}\sum_{k=1}^{n}(\frac{x_k - x_{\text{ar}}^{\ell}}{\sigma_k})^2\}\,, \tag{57}$$

in which σ_k is the empirical estimate of the standard deviation of X_k calculated with $\{x_{\text{ar},k}^{\ell}, \ell = 1,\ldots,N_{\text{ar}}\}$ and where s_{SBX} is the Silverman bandwidth that is written [117] as

$$s_{\text{SBX}} = \left(\frac{4}{N_{\text{ar}}(2+n)}\right)^{1/(4+n)}\,. \tag{58}$$

Since $\mathbf{W}$ with values in $\mathbb{R}^{n_w}$ is a representation of $\mathbf{W}^c$ with values in the finite set $\{0,1\}^{n_w}$, a modification of Eq. (57) is proposed as follows.

(i) Random variable Q is normalized in a random variable $\widetilde{Q}$. Let $\underline{q}$ and σ_Q be the empirical mean value and standard deviation of Q estimated with $\{q_{\text{ar}}^{\ell}, \ell = 1,\ldots,N_{\text{ar}}\}$. We then have,

$$Q = \underline{q} + \sigma_Q\,\widetilde{Q} \quad , \quad \widetilde{Q} = (Q - \underline{q})/\sigma_Q\,, \tag{59}$$

whose realizations of $\widetilde{Q}$ are

$$\widetilde{q}_{\text{ar}}^{\ell} = (q_{\text{ar}}^{\ell} - \underline{q})/\sigma_Q \quad , \quad \ell \in \{1,\ldots,N_d\}\,, \tag{60}$$

Consequently, Eq. (50) can be rewritten as

$$J_{\mathrm{ar}}(\mathbf{w}^c) = \underline{q} + \sigma_Q \, E\{\widetilde{Q} \,|\, \mathbf{W} = \mathbf{w}^c\}\,, \; \mathbf{w}^c \in \mathcal{N}_c\,. \tag{61}$$

In Eq. (61), the conditional mathematical expectation is written as

$$E\{\widetilde{Q}|\mathbf{W}=\mathbf{w}^c\} = \frac{1}{p_{\mathbf{W}}(\mathbf{w}^c)} \int_{\mathbb{R}} \widetilde{q}\, p_{\widetilde{Q},\mathbf{W}}(\widetilde{q}, \mathbf{w}^c)\, d\widetilde{q}, \tag{62}$$

in which $p_{\mathbf{W}}(\mathbf{w}^c) = \int_{\mathbb{R}} p_{\widetilde{Q},\mathbf{W}}(\widetilde{q}, \mathbf{w}^c)\, d\widetilde{q}$ and where $p_{\widetilde{Q},\mathbf{W}}$ is the pdf on $\mathbb{R} \times \mathbb{R}^{n_w}$ of random variable $(\widetilde{Q}, \mathbf{W})$ with respect to $d\widetilde{q}\, d\mathbf{w}$, whose following construction is directly deduced from Eq. (57).

(ii) The PLoM algorithm that is summarized in Section A.1 of Appendix A is appropriated to the case of a random vector $\mathbf{X}$ that belongs to an uncountable set $\mathbb{R}^n$. In the present case, the quantity of interest Q has values in an uncountable set whereas the control variable $\mathbf{W}$ is a representation of $\mathbf{W}^c$ that takes its values in a finite discrete set. This mixed uncountable - countable case can be approached elegantly with PLoM by taking an adapted value of the Silverman bandwidth of the nonparametric representation of the probability density function of $\mathbf{W}$ in order to properly separate the bimodality linked to the two discrete values $\{0\}$ and $\{1\}$. This is done and explained below.

Since $\mathbf{W}^c$ is a random variable with values in the finite set $\{0, 1\}^{n_w}$ and since the $\mathbb{R}^{n_w}$-valued random variable $\mathbf{W}$ is a representation of $\mathbf{W}^c$, we do not normalize $\mathbf{W}$ and we choose its bandwidth as $s_w = c_0\, s_{\mathrm{SBW}}$ for constructing the Gaussian KDE of pdf $p_{\mathbf{W}}$ in order to obtain a possible bimodality centered in 0 and in 1, in which s_{SBW} is the following Silverman bandwidth of $\mathbf{W}$,

$$s_{\mathrm{SBW}} = \left(\frac{4}{N_{\mathrm{ar}}(2+n_w)}\right)^{1/(4+n_w)}. \tag{63}$$

The numerical experiments have shown that $c_0 = 0.2$ is a good value for obtaining a clear separation (see Fig. 26). Therefore, we have

$$p_{\mathbf{W}}(\mathbf{w}) = \frac{1}{N_{\mathrm{ar}}} \sum_{\ell=1}^{N_{\mathrm{ar}}} \frac{1}{(s_w\sqrt{2\pi})^{n_w}} \exp\{-\frac{1}{2s_w^2}\|\mathbf{w} - \mathbf{w}_{\mathrm{ar}}^{\ell}\|^2\}, \tag{64}$$

in which $\|.\|$ is the usual Euclidean norm on $\mathbb{R}^{n_w}$.

(iii) Using (i) and (ii), the Gaussian KDE of $p_{\widetilde{Q},\mathbf{W}}$ is defined as

$$p_{\widetilde{Q},\mathbf{W}}(\widetilde{q}, \mathbf{w}) = \frac{1}{N_{\mathrm{ar}}} \sum_{\ell=1}^{N_{\mathrm{ar}}} \frac{1}{s_q\sqrt{2\pi}} \exp\{-\frac{1}{2s_q^2}(\widetilde{q} - \widetilde{q}_{\mathrm{ar}}^{\ell})^2 \times \frac{1}{(s_w\sqrt{2\pi})^{n_w}} \exp\{-\frac{1}{2s_w^2}\|\mathbf{w} - \mathbf{w}_{\mathrm{ar}}^{\ell}\|^2\}\,, \tag{65}$$

in which s_q is chosen as $s_q = (4/(3N_{\mathrm{ar}}))^{1/5}$. From Eqs. (62) and (65), it can be deduced that

$$E\{\widetilde{Q}|\mathbf{W}=\mathbf{w}^c\} = \frac{\sum_{\ell=1}^{N_{\mathrm{ar}}} \widetilde{q}_{\mathrm{ar}}^{\ell} \exp\{-\frac{1}{2s_w^2}\|\mathbf{w}^c - \mathbf{w}_{\mathrm{ar}}^{\ell}\|^2\}}{\sum_{\ell=1}^{N_{\mathrm{ar}}} \exp\{-\frac{1}{2s_w^2}\|\mathbf{w}^c - \mathbf{w}_{\mathrm{ar}}^{\ell}\|^2\}}\,. \tag{66}$$

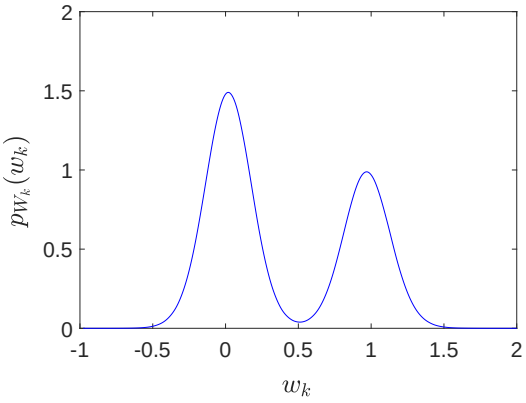

Figure 26: Scheme of the graph of the pdf $w_k \mapsto p_{W_k}(w_k)$ of a component W_k of $\mathbf{W}$ using Eq. (64) with $s_w = c_0\, s_{\mathrm{SBW}}$, $c_0 = 0.2$, and s_{SBW} given by Eq. (63).

4.9. Data for the validation of the optimization method based on a probabilistic machine learning tool

In subsections (i)-(iv), there are a few repetitions of results and discussions that have already be given in the previous sections. These small repetitions have voluntary be introduced in order to facilitate the reading of the paper in order to avoid going back and forth in the paper.

(i) Hypothesis and objective for the validation. The number n_w of blades in the blisk (See Section 3) has deliberately be chosen so that the number n_c of elements in C_c (all the possible configurations) is also small in order to build the exact solution of the combinatorial optimization problem defined by Eqs. (44)-(45), in order to be able to validate the proposed approach. For $n_w = 12$, the number of all possible configurations for which the blade of type 1 is less than or equal to $n_w/2 = 6$ is $n_c = 216$. Consequently, 216 calls to HFCM has been carried out for constructing the solution $\mathbf{w}_{\mathrm{un}}^{c,\mathrm{opt}}$ of Eqs. (44)-(45).

We wish to insist here on the fact that the proposed optimization method has been developed to analyze bladed-disks whose number of blades is such that n_c leads to a combinatorial optimization problem for which the cost function could only be evaluated with HFCM for N_d configurations with $N_d \ll n_c$. In such a case, the construction of the exact solution of Eqs. (44)-(45) is unachievable and therefore, a reference solution would not be available for the validation. For instance, for $n_w = 24$, we would have $n_c \simeq 350,000$, which would require $350,000$ call to HFCM, that is unachievable.

(ii) Defining the n_c configurations of C_c. The $n_c = 216$ configurations $\{\mathbf{w}^{c,\ell}, \ell = 1, \ldots, n_c\}$ of C_c are extracted from the 352 configurations introduced in Section 3.9.

(iii) Computation of the dynamic amplification factor for all the configurations in C_c. In order to construct the exact optimal solution $\mathbf{w}_{\mathrm{un}}^{c,\mathrm{opt}}$ of the combinatorial optimization problem on finite set C_c, defined by Eqs. (44)-(45), the $n_c = 216$ configurations $\{\mathbf{w}^{c,\ell}, \ell = 1, \ldots, n_c\}$ of C_c are considered and the n_c dynamic amplification factors $\{q^{c,\ell} = f_{\mathrm{HFCM}}(\mathbf{w}^{c,\ell}), \ell = 1, \ldots, n_c\}$ (see Sections 3.12 and 3.13) have been computed with HFCM. Fig. 27 shows the graph $\ell \mapsto q^{c,\ell}$ for $\ell \in \{1, \ldots, n_c\}$.

(1) The configuration $\mathbf{w}^{c,49}$ is the configuration without detuning in presence of random mistuning for which $w_k^{c,49} = 0$ for $k = 1, \ldots, n_w$ and $q^{c,49} = 1$.

(2) There are 14 configurations $\{\mathbf{w}^{c,\ell_j}, j = 1, \ldots, 14\}$ for which $q^{c,\ell_j} < 1$. The three smallest values of $q^{c,\ell}$ are reached for $\ell = 104$, 123, and 166 and are $q^{c,\ell} = 0.9476$, 0.9529, and 0.9537.

(3) It can be deduced that there are 202 configurations for which $q^{c,\ell}$ is greater than or equal to 1

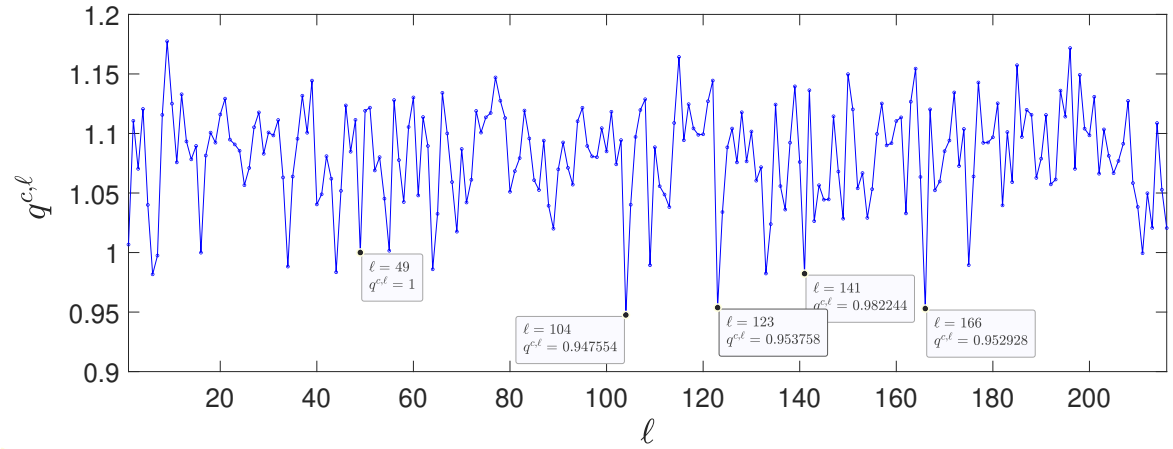

Figure 27: For the $n_c = 216$ configurations of C_c, dynamic amplification factor $q^{c,\ell}$ as a function of index $\ell \in \{1, \ldots, n_c\}$ of configuration $\mathbf{w}^{c,\ell}$, computed with HFCM.

(iv) Reference Optimal solution of the combinatorial optimization problem defined by Eqs. (44)-(45) *on finite set* C_c. From the previous paragraph (iii), it can be deduced that the reference optimal solution $\mathbf{w}_{\text{un}}^{c,\text{opt}}$ of Eqs. (44)-(45) is $\mathbf{w}^{c,104} = [0\,0\,0\,1\,0\,0\,1\,0\,0\,1\,0\,1\,1]$, which is such that $q^{c,104} = f_{\text{HFCM}}(\mathbf{w}^{c,104}) = 0.9476$.

(v) Defining the subset $C_{c,q\geq 1}$ *of* C_c *for constructing the training set*. In order to present a validation of the proposed method, which is based on the use of PLoM as a probabilistic learning tool, we consider the most difficult case that consists only of configurations $\mathbf{w}^{c,\ell}$ for which the dynamic amplification factor $q^{c,\ell} = f_{\text{HFCM}}(\mathbf{w}^{c,\ell})$ is greater than or equal to 1. These configurations will constitute a subset $C_{c,q\geq 1}$ defined by

$$C_{c,q\geq 1} = \{\{\mathbf{w}^{c,\ell_j}, j = 1, \ldots, n_{c,q\geq 1}\} \,|\, q^{c,\ell_j} = f_{\text{HFCM}}(\mathbf{w}^{c,\ell_j}) \geq 1\}\,. \tag{67}$$

Fig. 28 shows the graph $\ell \mapsto q^{c,\ell}$ for the $n_{c,q\geq 1}$ configurations of $C_{c,q\geq 1}$.

(vi) Defining the training set $\mathcal{D}_d$ *for the validation of the machine learning tool*. Let N_d be the number of points in the training set $\mathcal{D}_d$ (see Section 4.6-(i). For the validation that we propose, 4 values of N_d are considered. We recall that any convergence analysis with respect to N_d has no object (see Section 4.7-(vi)-(H1)). The reason for this choice of these four values are the following. The construction of the training set $\mathcal{D}_d$ is then performed as follows. For each considered value of N_d, the first N_d points of $C_{c,q\geq 1}$ are selected,

$$\mathcal{D}_d = \{(q^{c,\ell_j}, \mathbf{w}^{c,\ell_j}), j = 1, \ldots, N_d\} \subset C_{c,q\geq 1}\,, \tag{68}$$

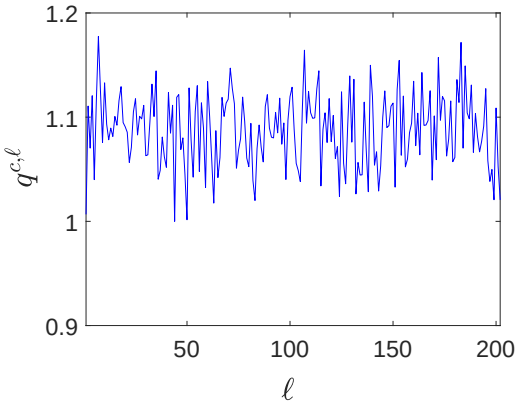

Figure 28: For the $n_{c,q\geq 1} = 202$ configurations of $C_{c,q\geq 1}$, graph of the dynamic amplification factor $q^{c,\ell_j} = f_{\text{HFCM}}(\mathbf{w}^{c,\ell_j}) \geq 1$ as a function of index $j \in \{1, \ldots, n_{c,q\geq 1}\}$ computed with HFCM.

in which $\{\mathbf{w}^{c,\ell_j}), j = 1, \ldots, N_d\}$ are defined in Section 4.9-(v). The four chosen values of N_d are 50, 75, 100, and 202.

(1) For each one of the two values 50 and 75 of N_d, the prediction of subset $\mathcal{W}_{n_s}^{\text{opt}}$ of C_c with $n_s = 6$ (see Eq. (52)) is carried out and the best solution $\mathbf{w}^{c,\ell_{\text{opt}}}$ is deduced (see Section 4.7-(vi)).

(2) The third value $N_d = 100$ is then considered in order to compare the corresponding best solution with the one obtained for $N_d = 75$.

(3) Finally, the last value, $N_d = n_{c,q\geq 1} = 202$, has just been considered to check the consistency of the approach proposed for solving the combinatorial optimization problem.

(vii) Values of the parameters of the PLoM algorithm. These values are given in Section A.2 of Appendix A.

4.10. Results and discussion

(i) Convergence analysis of the subset of optimal solutions with respect to the number N_{ar} of points in the learned set $\mathcal{D}_{\text{ar}}$. This convergence analysis with respect to N_{ar} (see Section 4.6-(ii)) has been defined in Section 4.7-(v) and is carried out for each training set $\mathcal{D}_d$ defined by N_d points. Let $\{(q_{\text{ar}}^{\ell}, \mathbf{w}_{\text{ar}}^{\ell}), \ell = 1, \ldots, N_{\text{ar}}\}$ be the N_{ar} points of $\mathcal{D}_{\text{ar}}$ generated by PLoM. The criteria for the convergence analysis are the empirical estimates $\text{conv}_{\text{Q}}(\text{N}_{\text{ar}})$ and $\text{conv}_{\mathbf{W}}(\text{N}_{\text{ar}})$ of the mean-square norm of Q and $\mathbf{W}$,

$$\text{conv}_{\text{Q}}(\text{N}_{\text{ar}}) = \{\frac{1}{\text{N}_{\text{ar}}} \sum_{\ell=1}^{\text{Nar}} (\text{q}_{\text{ar}}^{\ell})^2\}^{1/2}\,, \tag{69}$$

$$\text{conv}_{\mathbf{W}}(\text{N}_{\text{ar}}) = \{\frac{1}{\text{N}_{\text{ar}}} \sum_{\ell=1}^{\text{Nar}} \|\mathbf{w}_{\text{ar}}^{\ell}\|^2\}^{1/2}\,. \tag{70}$$

For $N_d = 50$, the convergence is obtained for $N_{\text{ar}} = 2 \times 10^7$, while for $N_d = 75$, 100, and 202, for $N_{\text{ar}} = 10^7$. For illustration and for $N_d = 75$, Fig. 29 displays the graph of function $N_{\text{ar}} \mapsto \text{conv}_{\text{Q}}(\text{N}_{\text{ar}})$ defined by Eq. (69) while Fig. 30 displays the graph of function $N_{\text{ar}} \mapsto \text{conv}_{\mathbf{W}}(\text{N}_{\text{ar}})$ defined by Eq. (70). The graphs of the three other values of N_d are similar.

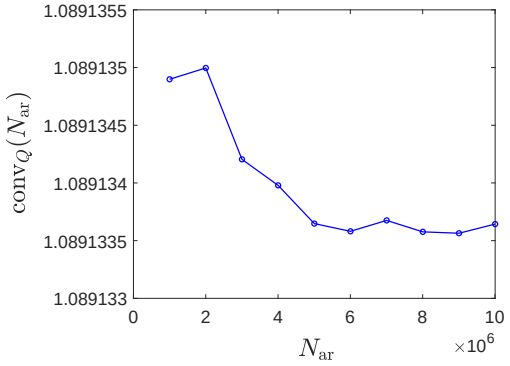

Figure 29: For $N_d = 75$, graph of function $N_{\mathrm{ar}} \mapsto \mathrm{conv_Q(N_{ar})}$.

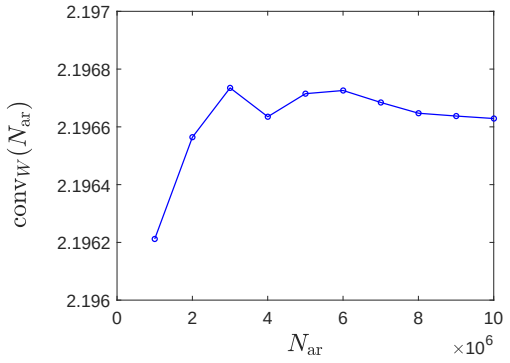

Figure 30: For $N_d = 75$, graph of function $N_{\mathrm{ar}} \mapsto \mathrm{conv_W(N_{ar})}$.

(ii) Illustration of the detailed results for $N_d = 75$ using PLoM. In order to limit the number of figures, we illustrate the results obtained by using PLoM for $N_d = 75$. Qualitatively, the results for the three other values of N_d are similar.

(a) *Generation of the learned set with PLoM*. Figs. 31 and 32 show realizations q^{ℓ}_{ar} and $w^{\ell}_{\mathrm{ar},1}$ (first component of $\mathbf{w}^{\ell}_{\mathrm{ar}}$) for $\ell \in \{5\,240\,000, \ldots, 5\,245\,000\}$ of $\mathcal{D}_{\mathrm{ar}}$ generated by using PLoM (we have presented a zoom in order to avoid a view having an absence of space resolution when the 10^7 realizations are plotted). The pdf $w_1 \mapsto p_{W_1}(w_1)$ of component W_1 of $\mathbf{W}$, estimated using $\{w^{\ell}_{\mathrm{ar},1}, \ell = 1, \ldots, 10^7\}$ is shown in Fig. 33.

(b) *Cost function computed with the learned set*. Fig. 34 shows the graph of function $\ell \mapsto J_{\mathrm{ar}}(\mathbf{w}^{c,\ell})$ for $\ell \in \{1, \ldots, n_c\}$ (with $n_c = 216$) in which $J_{\mathrm{ar}}(\mathbf{w}^{c,\ell})$ is computed by using Eqs. (61) and (66) with $N_{\mathrm{ar}} = 10^7$. This graph is superimposed to the graph of function $\ell \mapsto q^{c,\ell}$ (the reference shown in Fig. 27). It can be seen that the two graphs have similar fluctuations.

(c) *Computation of the best optimal solution*. For $n_s = 6$, the indices $\{\ell_j, j = 1, \ldots, 6\}$ of the 6 configurations $\mathbf{w}^{c,\ell_j}$, which define subset $\mathcal{W}^{\mathrm{opt}}_{n_s}$ of optimal solutions (see Eqs. (52) and (53)) are 7, 34, 49, 55, 1, and 166, for which the corresponding values of q^{c,ℓ_j} (see Section 4.9-(iii) and

Fig. 27) are respectively, 0.9974, 0.9882, 1.0000 (the tuned configuration), 1.0015, 1.0067, and 0.9529. The use of Eq. (56) yields the best optimal solution $\mathbf{w}^{c,\ell_{\text{opt}}} = [1\,0\,1\,1\,0\,0\,1\,0\,0\,1\,0\,0]$ for which $\ell_{\text{opt}} = 166$ and $q^{c,\ell_{\text{opt}}} = 0.9529$.

(d) *Numerical cost*. The numerical cost in terms of Elapsed Time (in seconds) of the analysis performed with a workstation 3072 GB RAM and 110 cores (Intel(R) Xeon(R) Platinium 8280 CPU@2.706 Hz) is the following: 21 607 *s* for the generation of the learned dataset by the PLoM with constraints and 1 144 *s* for computing the best optimal solution.

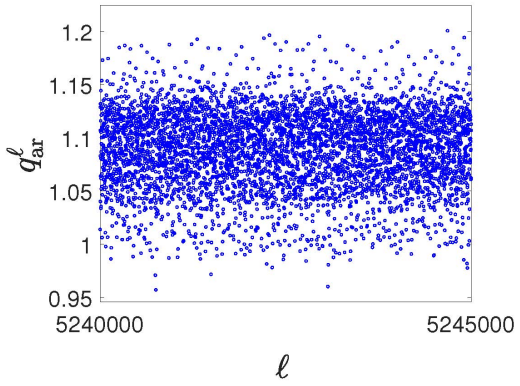

Figure 31: For $N_d = 75$, realizations q^{ℓ}_{ar} for $\ell \in \{5.240, \ldots, 5.245\} \times 10^6$ of Q generated by PLoM.

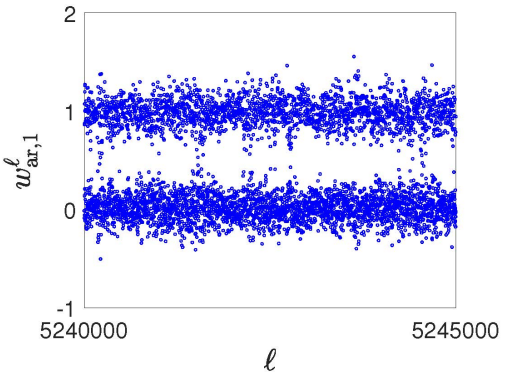

Figure 32: For $N_d = 75$, realizations $w^{\ell}_{\text{ar},1}$ of the first component of $\mathbf{w}^{\ell}_{\text{ar}}$ for $\ell \in \{5.240, \ldots, 5.245\} \times 10^6$ of $\mathbf{W}$ generated by PLoM.

(iii) Checking the stability and consistency of the proposed methodology and algorithm. The proposed methodology and algorithm allow for estimating the best optimal solution $\mathbf{w}^{c,\ell_{\text{opt}}}$ given by Eq. (56), in which $\mathcal{W}^{\text{opt}}_{n_s}$ is constructed using Eqs. (52)-(53), and where $J_{\text{ar}}(\mathbf{w}^{c,\ell_j})$ is computed by Eqs. (61) and (66), in which the learned set $\mathcal{D}_{\text{ar}} = \{(q^{\ell}_{\text{ar}}, \mathbf{w}^{\ell}_{\text{ar}}), \ell = 1, \ldots, N_{\text{ar}}\}$ is generated using PLoM algorithm from the training set $\mathcal{D}_d$ defined by Eq. (68) for a given value of N_d. In order to check the stability/consistency of the algorithm, we have analyzed the case for which

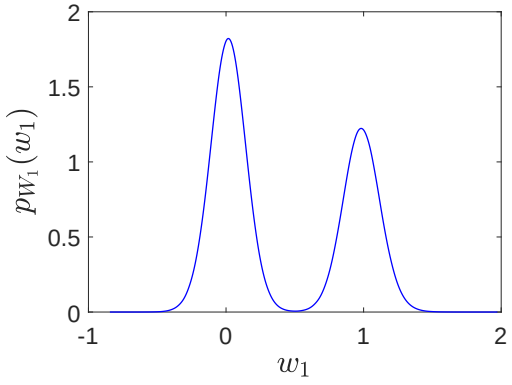

Figure 33: For $N_d = 75$, pdf $w_1 \mapsto p_{W_1}(w_1)$ of component W_1 of $\mathbf{W}$, estimated using $\{w_{\text{ar},1}^{\ell}, \ell = 1, \ldots, 10^7\}$ generated by PLoM.

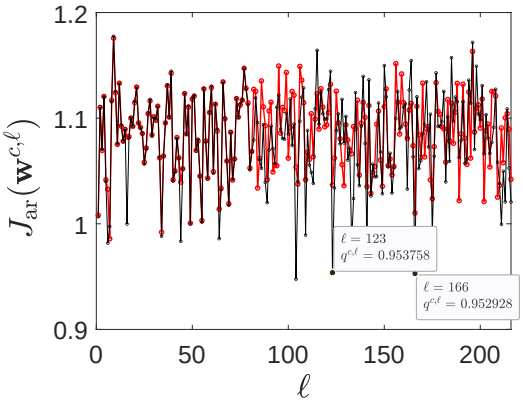

Figure 34: For $N_d = 75$, graph of function $\ell \mapsto J_{\text{ar}}(\mathbf{w}^{c,\ell})$ for $\ell \in \{1, \ldots, n_c\}$, with $n_c = 216$ (red thick line) and graph of function $\ell \mapsto q^{c,\ell}$, the reference shown in Fig. 27 (black thin line).

$\mathcal{D}_d = C_c$ that is therefore constituted of $N_d = n_c$ points of C_c (see Section 4.9-(iii)). The results are presented in the next paragraph and are good.

(iv) Synthesis of the results obtained as a function of the number N_d of points in the training set $\mathcal{D}_d$. The results obtained with the proposed methodology/algorithm are summarized in Tables 8 and 9 for $n_s = 6$.

(1) The best optimal solution obtained for $N_d = 50$ improves the dynamic amplification factors $\{q^{c,\ell_j}, j = 1, \ldots, 50\}$ used in the training set $\mathcal{D}_d$ defined by Eq. (68) for which $q^{c,\ell_j} \geq 1$, which have been computed with HFCM. However, although $q^{c,\ell_{\text{opt}}} = 0.9822 < 1$, it is not a value close to the optimum that is 0.9476. As explained in Section 4.7-(vi)-(H4)-(a) and (b), this solution can possibly be improved by increasing the value of N_d as it can be seen in Table 8.

(2) For $N_d = 75$ and, *a fortiori*, for $N_d = 100$ and 202, the best optimal solutions $q^{c,\ell_{\text{opt}}}$ are 0.9529 and 0.9538 that are close to the optimum 0.9476, and which constitute very good predictions.

Table 8: Synthesis of the results as a function of the number N_d of points in the training set $\mathcal{D}_d$ and results obtained for $N_d = n_c = 216$ (reference).

N_d	$j = 1, \ldots, 6$	$\mathcal{W}_{n_s}^{\text{opt}}$						ℓ_{opt}	$q^{c,\ell_{\text{opt}}}$
50	ℓ_j	211	7	44	49	141	55	141	0.9822
	q^{c,ℓ_j}	0.9995	0.9974	0.9834	1.0000	0.9822	1.0015		
75	ℓ_j	7	34	49	55	1	166	166	0.9529
	q^{c,ℓ_j}	0.9974	0.9882	1.0000	1.0015	1.0067	0.9529		
100	ℓ_j	7	49	211	123	141	34	123	0.9538
	q^{c,ℓ_j}	0.9974	1.0000	0.9995	0.9538	0.9822	0.9882		
202	ℓ_j	49	55	34	123	1	141	123	0.9538
	q^{c,ℓ_j}	1.0000	1.0015	0.9882	0.9538	1.0067	0.9822		
Reference 216	ℓ_j	104	166	123	141	44	133	104	0.9476
	q^{c,ℓ_j}	0.9476	0.9529	0.9538	0.9822	0.9834	0.9824		

Table 9: Best optimal configuration $\mathbf{w}^{c,\ell_{\text{opt}}}$ listed in Table 8.

ℓ_{opt}	$q^{c,\ell_{\text{opt}}}$	$\mathbf{w}^{c,\ell_{\text{opt}}} = (w_1^{c,\ell_{\text{opt}}}, \ldots, w_{12}^{c,\ell_{\text{opt}}})$											
104	0.9476	0	0	0	1	0	0	1	0	0	1	0	1
123	0.9537	1	0	0	1	0	0	0	0	0	0	0	0
141	0.9822	1	0	0	0	0	1	0	0	0	0	0	0
166	0.9529	1	0	1	1	0	0	1	0	0	1	0	0

5. Conclusion and discussion

We have presented an approach for the optimization of the detuning in presence of random mistuning and geometrical nonlinearities for bladed-disks, based on the use of high-fidelity computational models. This very challenging problem has given rise to very little published work and remains an open subject. The difficulties we have addressed are related to the developments of an efficient computational methodology for reducing the computational cost, to the physics understanding of such stochastic nonlinear dynamical systems, and to the probabilistic formulation of the detuning optimization problem. We have presented a deep computational analysis on a bladed-disk that is representative of industrial turbomachines, in order to understand the role played by the geometrical nonlinearities on the dynamical behavior and to exhibit the consequences on the detuning effects. Several results can be put forward.

A careful convergence analysis with respect to all numerical parameters must be performed to obtain a predictive solution with an optimal computational cost. This is essential for exploring a relatively large number of detuned configurations in the context of the stochastic nonlinear mistuning analysis. It should be noted that the sensitivity analysis with respect to the time step used in the numerical resolution of the nonlinear coupled differential equations is particularly delicate, yielding a fast convergence in the excitation frequency band but a slow convergence in the low-frequency range that is not directly excited by the external loading.

Another point of attention concerns the choice of the quantities of interest used in the formulation of the detuning optimization problem from a scalar-valued highly nonlinear cost function. It is found that there is a few number of optimal solutions with respect to the number of possible detuned configurations. It is also proved that the optimization problem is well-posed, yielding to robust optimal detuned configurations that are identified after post-processing analysis as detuned configurations for which the mistuning amplification effects are inhibited with respect to the pure mistuning situation.

The detuning patterns yielding the best optimal detuned configurations and yielding the worst amplification response levels have no particularly structure in terms of number of blades of different types and of blade distribution, which deserve further investigations to understand the complex mechanisms induced by the detuning. As expected, the sub-cyclic detuned configurations that present a cyclic symmetry with a lower cyclic order are sensitive to the mistuning and are not part of the optimal solutions.

For the considered bladed-disk, the sensitivity analysis with respect to the detuning rate or the mistuning rate shows that the detuned configuration yielding the worst case in terms of response amplification remains a wrong detuned configuration whatever the detuning or mistuning rate. There also exists a threshold in terms of detuning rate and mistuning rate from which a detuned configuration belongs to the set of optimal detuned configurations. There is no guarantee that an optimal solution remains optimal when the detuning rate increases too much. Note that the mistuning rate corresponds to the uncertainty level related to the global stiffness matrix with a huge dimension and that the involved magnitude orders are much larger than the uncertainty levels describing the usual frequency mistuning modeling but corresponds in fact to small mistuning levels.

The chosen external load corresponds to a narrow-frequency band of excitation so that the linearized detuning optimization problem has no real interest. It cannot be properly achieved since the natural frequencies of most detuned configurations do not belong to this narrow excitation frequency range and since the structure only can respond in the excitation frequency band. This is to underline that the nonlinear detuned optimization problem is of different nature because of the complex vibratory behavior induced by the geometric nonlinearities that appear themselves as an excitation that spreads the nonlinear response on the whole frequency band of analysis.

Concerning the detuning optimization of bladed-disks in presence of random mistuning, for nonlinear responses regimes involved by geometrical nonlinearities and using high-fidelity computational models, there are no published methods. When the number of detuned configurations is large, we have proposed a reformulation in a probabilistic framework of the combinatorial optimization problem, which is adapted to a probabilistic machine learning tool in order to limit the number of evaluations of the cost function with the high-fidelity computational model. The optimization must be carried out in a probabilistic framework in order to give robustness to the identification of an optimal detuned configuration. It should be noted that the proposed approach is unambiguous as it allows for building a subset of optimal detuned configurations and the search for the optimal solution in this subset is done using the high-fidelity computational model. The methodology proposed has been validated for a 12-bladed-disk structure for which the exact optimal detuned configuration in presence of random mistuning has been identified. A good prediction has been obtained for this very difficult case, which constitutes one validation of the proposed method.

Acknowledgments

The authors thank Pr. Christophe Pierre from the Illinois University concerning the use of the bladed-disk finite element model.

A. Probabilistic learning on manifolds (PLoM), its parameterization and numerical results

A.1. Summary of the PLoM algorithm

The PLoM approach [103, 104, 105] starts from a training set $\mathcal{D}_d$ made up of a relatively small number N_d of points. For the supervised case, it is assumed that the training set is related to an underlying stochastic manifold related to a $\mathbb{R}^n$-valued random variable $\mathbf{X} = (\mathbf{Q}, \mathbf{W})$ in which $\mathbf{X}$, $\mathbf{Q}$ (quantity of interest), and $\mathbf{W}$ (control parameter) are $\mathbb{R}^n$-, $\mathbb{R}^{n_q}$-, and $\mathbb{R}^{n_w}$-valued random variables defined on a probability space $(\Theta, \mathcal{T}, \mathcal{P})$ with $n = n_q + n_w$. Let $\mathbf{U}$ (uncontrolled parameter) be another $\mathbb{R}^{n_u}$- valued random variable defined on $(\Theta, \mathcal{T}, \mathcal{P})$. Random variable $\mathbf{Q}$ is written as $\mathbf{Q} = \mathbf{f}(\mathbf{U}, \mathbf{W}) = \mathbf{F}(\mathbf{W})$ in which the measurable mapping $\mathbf{f}$ is not explicitly known (unknown) and $\mathbf{F}$ is such that $\mathbf{F} = \mathbf{f}(\mathbf{U}, \cdot)$ is a random mapping. The probability distributions of the vector-valued random variables $\mathbf{W}$ and $\mathbf{U}$ are assumed to be given. The stochastic manifold is defined by the unknown random graph $\{\mathbf{w}, \mathbf{F}(\mathbf{w})\}$ for $\mathbf{w}$ belonging to an admissible set C_w that is the support of the probability distribution of $\mathbf{W}$. With the PLoM construction, its is assumed that this stochastic manifold cannot directly be described. Under these conditions, the non-Gaussian probability measure of $\mathbf{X}$ is concentrated in a region of $\mathbb{R}^n$ for which the only available information is the cloud of the points of the training set. The PLoM method makes it possible to generate the learned set $\mathcal{D}_{\text{ar}}$ whose $n_{\text{MC}} \gg N_d$ points (learned realizations) are generated by the non-Gaussian probability measure that is estimated from the training set. The concentration of the probability measure is preserved thanks to the use of a diffusion-maps basis that allows to enrich the available information from the training set. It should also be noted that the estimate of the unknown probability measure of $\mathbf{X}$ cannot be performed from the training set by using an arbitrary estimator. It must be parameterized in a manner that permits convergence to any probability measure as its number of points in the training set goes towards infinity. The PLoM method therefore does not only consist in generating points that belong to the region in which the measure is concentrated, but also allows these learned points to be realizations of the estimate probability measure with the convergence properties evoked above. The choice of the kernel density estimation method for estimating the probability measure of $\mathbf{X}$ from the training dataset guarantees that this required fundamental property is satisfied [104]. Considering all of these assumptions in the construction and in the methodology of PLoM makes PLoM as a general approach for small datasets for arbitrary non-Gaussian measures. Using the learned set $\mathcal{D}_{\text{ar}}$, PLoM allows for carrying out any conditional statistics such as $\mathbf{w} \mapsto E\{\mathbf{Q}|\mathbf{W} = \mathbf{w}\}$ from C_w in $\mathbb{R}^{n_q}$, and consequently, to directly construct metamodels in a probabilistic framework.

The training set $\mathcal{D}_d$ is made up of the N_d independent realizations $\{\mathbf{x}_d^j = (\mathbf{q}_d^j, \mathbf{w}_d^j) \in \mathbb{R}^n = \mathbb{R}^{n_q} \times \mathbb{R}^{n_w}, j = 1, \ldots, N_d\}$ of random variable $\mathbf{X} = (\mathbf{Q}, \mathbf{W})$. The PLoM method allows for generating the learned set $\mathcal{D}_{\text{ar}}$ made up of $N_{\text{ar}} \gg N_d$ learned realizations $\{\mathbf{x}_{\text{ar}}^\ell, \ell = 1, \ldots, N_{\text{ar}}\}$ of random vector $\mathbf{X}$. As soon as the learned set has been constructed, the learned realizations for $\mathbf{Q}$ and $\mathbf{W}$ can be extracted as $(\mathbf{q}_{\text{ar}}^\ell, \mathbf{w}_{\text{ar}}^\ell) = \mathbf{x}_{\text{ar}}^\ell$ for $\ell = 1, \ldots, N_{\text{ar}}$.

(i) Normalization of the training set. The N_d independent realizations $\{\mathbf{x}_d^j, j = 1, \ldots, N_d\}$ of $\mathbf{X}$ with values in $\mathbb{R}^n$ can be represented by the matrix $[x_d] = [\mathbf{x}_d^1 \ldots \mathbf{x}_d^{N_d}]$ in $\mathbb{M}_{n,N_d}$. Let $[\mathbf{X}] =$

$[\mathbf{X}^1, \ldots, \mathbf{X}^{N_d}]$ be the random matrix with values in $\mathbb{M}_{n,N_d}$, whose columns are N_d independent copies of random vector $\mathbf{X}$. Therefore, $[x_d]$ is one realization of random matrix $[\mathbf{X}]$. The normalization of random matrix $[\mathbf{X}]$ is performed by using a principal component analysis (PCA) of $\mathbf{X}$ allowing for defining the random matrix $[\mathbf{H}] = [\mathbf{H}^1, \ldots, \mathbf{H}^{N_d}]$ with values in $\mathbb{M}_{\nu,N_d}$ with $\nu \leq n$. Consequently, random matrix $[\mathbf{X}]$ is written as,

$$[\mathbf{X}] = [\underline{x}] + [\varphi]\,[\mu]^{1/2}\,[\mathbf{H}]\,, \tag{71}$$

in which $[\mu]$ is the $(\nu \times \nu)$ diagonal matrix of the ν positive eigenvalues of the empirical estimate of the covariance matrix of $\mathbf{X}$ (computed using $\mathbf{x}_d^1, \ldots, \mathbf{x}_d^{N_d}$). The $(n \times \nu)$ matrix $[\varphi]$ is made up of the associated eigenvectors such $[\varphi]^T\,[\varphi] = [I_\nu]$. The matrix $[\underline{x}]$ in $\mathbb{M}_{n,N_d}$ has identical columns, each one being equal to the empirical estimate $\underline{\mathbf{x}} \in \mathbb{R}^n$ of the mean value of random vector $\mathbf{X}$ (computed using $\mathbf{x}_d^1, \ldots, \mathbf{x}_d^{N_d}$). The columns of $[\mathbf{H}]$ are N_d independent copies of a random vector $\mathbf{H}$ with values in $\mathbb{R}^\nu$. The realization $[\eta_d] = [\boldsymbol{\eta}_d^1 \ldots \boldsymbol{\eta}_d^{N_d}] \in \mathbb{M}_{\nu,N_d}$ of $[\mathbf{H}]$ (associated with the realization $[x_d]$ of $[\mathbf{X}]$) is computed by $[\eta_d] = [\mu]^{-1/2}[\varphi]^T\,([x_d] - [\underline{x}])$. The value ν is classically calculated in order that the L^2- error function $\nu \mapsto \mathrm{err}_{\mathbf{X}}(\nu)$ defined by

$$\mathrm{err}_{\mathbf{X}}(\nu) = 1 - \frac{\sum_{\alpha=1}^{\nu} \mu_\alpha}{E\{\|\mathbf{X}\|^2\}}\,, \tag{72}$$

be smaller that $\varepsilon_{\mathrm{PCA}}$. If $\nu < n$, then there is a statistical reduction.

(ii) Construction of a reduced-order diffusion-maps basis (ROB). To identify the subset around which the points of the training set are concentrated, the PLoM relies on the diffusion-maps method [118, 119]. This is an algebraic basis of vector space $\mathbb{R}^{N_d}$, which is constructed using the diffusion maps. Let $[K]$ and $[b]$ be the matrices such that, for all i and j in $\{1, \ldots, N_d\}$, $[K]_{ij} = \exp\{-(4\,\varepsilon_{\mathrm{DM}})^{-1}\|\boldsymbol{\eta}_d^i - \boldsymbol{\eta}_d^j\|^2\}$ and $[b]_{ij} = \delta_{ij}\,b_i$ with $b_i = \sum_{j=1}^{N_d}[K]_{ij}$, in which $\varepsilon_{\mathrm{DM}} > 0$ is a smoothing parameter (the non symmetric matrix $\mathbb{P} = [b]^{-1}[K] \in \mathbb{M}_{N_d}$ is the transition matrix of a Markov chain that yields the probability of transition in one step). The eigenvalues $\lambda_1, \ldots, \lambda_{N_d}$ and the associated eigenvectors $\boldsymbol{\psi}^1, \ldots, \boldsymbol{\psi}^{N_d}$ of the right-eigenvalue problem $[\mathbb{P}]\,\boldsymbol{\psi}^\alpha = \lambda_\alpha\,\boldsymbol{\psi}^\alpha$ are such that $1 = \lambda_1 > \lambda_2 \geq \ldots \geq \lambda_{N_d}$ and are computed by solving the generalized eigenvalue problem $[K]\,\boldsymbol{\psi}^\alpha = \lambda_\alpha\,[b]\,\boldsymbol{\psi}^\alpha$ with the normalization $< [b]\,\boldsymbol{\psi}^\alpha, \boldsymbol{\psi}^\beta >= \delta_{\alpha\beta}$. The eigenvector $\boldsymbol{\psi}^1$ associated with $\lambda_1 = 1$ is a constant vector. For a given integer $\kappa \geq 0$, the diffusion-maps basis $\{\mathbf{g}^1, \ldots, \mathbf{g}^\alpha, \ldots, \mathbf{g}^{N_d}\}$ is a vector basis of $\mathbb{R}^{N_d}$ defined by $\mathbf{g}^\alpha = \lambda_\alpha^\kappa\,\boldsymbol{\psi}^\alpha$. For a given integer m with $3 \leq m \leq N_d$, the reduced-order diffusion-maps basis of order m is defined as the family $\{\mathbf{g}^1, \ldots, \mathbf{g}^m\}$ that is represented by the matrix $[g_m] = [\mathbf{g}^1 \ldots \mathbf{g}^m] \in \mathbb{M}_{N_d,m}$ with $\mathbf{g}^\alpha = (g_1^\alpha, \ldots, g_{N_d}^\alpha)$ and $[g_m]_{\ell\alpha} = g_\ell^\alpha$. This ROB depends on two parameters, $\varepsilon_{\mathrm{DM}}$ and m, which have to be identified. It is proven in [104], that the PLoM method does not depend of κ that can therefore be chosen to 0.

For estimating the optimal values $\varepsilon_{\mathrm{opt}}$ of $\varepsilon_{\mathrm{DM}}$ and m_{opt} of m, we use the algorithm proposed in [105], which is summarized hereinafter. We have to find the value $m_{\mathrm{opt}} \leq N_d$ of m and the smallest value $\varepsilon_{\mathrm{opt}} > 0$ of $\varepsilon_{\mathrm{DM}}$ such that

$$1 = \lambda_1 > \lambda_2(\varepsilon_{\mathrm{opt}}) \simeq \ldots \simeq \lambda_{m_{\mathrm{opt}}}(\varepsilon_{\mathrm{opt}}) \gg \lambda_{m_{\mathrm{opt}}+1}(\varepsilon_{\mathrm{opt}}) \geq \ldots \geq \lambda_{N_d}(\varepsilon_{\mathrm{opt}}) > 0\,, \tag{73}$$

with an amplitude jump equal to an order of magnitude (a factor 10 as demonstrated in [104]) between $\lambda_{m_{\mathrm{opt}}}(\varepsilon_{\mathrm{opt}})$ and $\lambda_{m_{\mathrm{opt}}+1}(\varepsilon_{\mathrm{opt}})$. This property means that we have to find $m_{\mathrm{opt}} \leq N_d$ and the smallest positive value $\varepsilon_{\mathrm{opt}}$ in order (1) to have $\lambda_2(\varepsilon_{\mathrm{opt}}) < 1$ (one must not have several

eigenvalues in the neighborhood of 1) and (2) to obtain a plateau for $\lambda_2(\varepsilon_{\text{opt}})$ to $\lambda_{m_{\text{opt}}}(\varepsilon_{\text{opt}})$ with a jump of amplitude 10 between $\lambda_{m_{\text{opt}}}(\varepsilon_{\text{opt}})$ and $\lambda_{m_{\text{opt}}+1}(\varepsilon_{\text{opt}})$. A further in-depth analysis makes it possible to state the following criterion and algorithm to easily estimate ε_{opt} and m_{opt}. Let $\varepsilon_{\text{DM}} \mapsto \text{Jump}(\varepsilon_{\text{DM}})$ be the function on $]0, +\infty[$ defined by

$$\text{Jump}(\varepsilon_{\text{DM}}) = \lambda_{m_{\text{opt}}+1}(\varepsilon_{\text{DM}})/\lambda_2(\varepsilon_{\text{DM}})\,. \tag{74}$$

The algorithm is the following:
- set the value of m to $m_{\text{opt}} = \nu + 1$;
- identify the smallest possible value ε_{opt} of ε_{DM} in order that $\text{Jump}(\varepsilon_{\text{opt}}) \leq 0.1$ and such that Equation (73) be verified.

Remark concerning the choice of factor 10 for the jump of the eigenvalues. This choice is justified in [104], which gives the mathematical results in support of PLoM (we refer the reader to Theorem 7.8 of this paper and its Lemmas 7.5, 7.6, and 7.7 on which the proof is based). In this paper, it is proven that Eq. (73) must hold for preserving the concentration of the probability measure, which is quantified by the square of the L^2-distance (see Eq. (75)), and which is estimated with the $N_{\text{ar}} \gg N_d$ learned realizations. Note that there are two important hypotheses in Eq. (73) that must be verified: one is the existence of the plateau for $m \in \{2, \ldots, m_{\text{opt}}\}$ and the other one is the existence of a jump between $m = m_{\text{opt}}$ and $m = m_{\text{opt}} + 1$. In [104], it is proven that the plateau and the jump on the eigenvalues are directly related to the variations of the function $m \mapsto \varepsilon_{\text{DM}}(m)$ (denoted as $m \mapsto \varepsilon_d(m)$ in [104]), which has to be rapidly decreasing in m in the neighborhood of m_{opt} by the lower integer values and which has to remain much lower than 1 for $m \geq m_{\text{opt}}$ (see Fig. 1 of [104]). When Eq. (73) holds, then $\varepsilon_{\text{DM}}(m) \ll 1$ for $m \geq m_{\text{opt}}$, that is a fundamental property used for proving Theorem 7.8. This property $\varepsilon_{\text{DM}}(m) \ll 1$ for $m \geq m_{\text{opt}}$ has been quantified by choosing one order of magnitude for the jump of the eigenvalues.

(iii) Reduced-order representation of random matrices $[\boldsymbol{H}]$ *and* $[\boldsymbol{X}]$. The diffusion-maps vectors $\mathbf{g}^1, \ldots, \mathbf{g}^m \in \mathbb{R}^{N_d}$ span a subspace of $\mathbb{R}^{N_d}$ that characterizes, for the optimal values m_{opt} and ε_{opt} of m and ε_{DM}, the local geometry structure of data set $\{\boldsymbol{\eta}_d^j, j = 1, \ldots, N_d\}$. So the PLoM method introduces the $\mathbb{M}_{\nu,N_d}$-valued random matrix $[\mathbf{H}_m] = [\mathbf{Z}_m]\,[g_m]^T$ with $3 \leq m \leq N$, corresponding to a data-reduction representation of random matrix $[\mathbf{H}]$, in which $[g_m]$ is the ROB and where $[\mathbf{Z}_m]$ is a $\mathbb{M}_{\nu,m}$-valued random matrix for which its probability measure $p_{[\mathbf{Z}_m]}([z])\,d[z]$ is explicitly described by Proposition 2 of [104]. The MCMC generator of random matrix $[\mathbf{Z}_m]$ belongs to the class of Hamiltonian Monte Carlo methods, is explicitly described in [103], and is mathematically detailed in Theorem 6.3 of [104]. For generating the learned set, the best probability measure of $[\mathbf{H}_m]$ is obtained for $m = m_{\text{opt}}$ and using the previously defined $[g_{m_{\text{opt}}}]$. For these optimal quantities m_{opt} and $[g_{m_{\text{opt}}}]$, the generator allows for computing n_{MC} realizations $\{[\mathbf{z}_{\text{ar}}^\ell], \ell = 1, \ldots, n_{\text{MC}}\}$ of $[\mathbf{Z}_{m_{\text{opt}}}]$ and therefore, for deducing the n_{MC} realizations $\{[\boldsymbol{\eta}_{\text{ar}}^\ell], \ell = 1, \ldots, n_{\text{MC}}\}$ of $[\mathbf{H}_{m_{\text{opt}}}]$. The reshaping of matrix $[\boldsymbol{\eta}_{\text{ar}}^\ell] \in \mathbb{M}_{\nu,N_d}$ allows for obtaining $N_{\text{ar}} = n_{\text{MC}} \times N_d$ learned realizations $\{\boldsymbol{\eta}_{\text{ar}}^{\ell'}, \ell' = 1, \ldots, N_{\text{ar}}\}$ of $\mathbf{H}$. These learned realizations allow for estimating converged statistics on $\mathbf{H}$ and then on $\mathbf{X}$, such as pdf, moments, or conditional expectation of the type $E\{\boldsymbol{\xi}(\mathbf{Q}) \,|\, \mathbf{W} = \mathbf{w}\}$ for $\mathbf{w}$ given in $\mathbb{R}^{n_w}$ and for any given vector-valued function $\boldsymbol{\xi}$ defined on $\mathbb{R}^{n_q}$.

(iv) Quantifying the concentration of the probability measure of random matrix $[\boldsymbol{H}_{m_{\text{opt}}}]$. In [104], for $3 \leq m \leq N_d$, we have introduced an L^2-distance $d_{N_d}(m)$ of random matrix $[\mathbf{H}_m]$ to matrix $[\eta_d]$ in order to quantify the concentration of the probability measure of random matrix $[\mathbf{H}_m]$, which

is informed by the training set represented by matrix $[\eta_d]$. The square of this distance is defined by

$$d^2_{N_d}(m) = E\{\|[\mathbf{H}_m] - [\eta_d]\|^2\}/\|[\eta_d]\|^2 \,. \tag{75}$$

Let $\mathcal{M}_{\text{opt}} = \{m_{\text{opt}}, m_{\text{opt}} + 1, \ldots, N_d\}$ in which m_{opt} is the optimal value of m previously defined. Theorem 7.8 of [104] shows that $\min_{m\in\mathcal{M}_{\text{opt}}} d^2_{N_d}(m) \leq 1 + m_{\text{opt}}/(N_d - 1) < d^2_{N_d}(N_d)$, which means that the PLoM method, for $m = m_{\text{opt}}$ and $[g_{m_{\text{opt}}}]$ is a better method than the usual one corresponding to $d^2_{N_d}(N_d) = 1 + N_d/(N_d - 1) \simeq 2$. Using the n_{MC} realizations $\{[\boldsymbol{\eta}^\ell_{\text{ar}}], \ell = 1, \ldots, n_{\text{MC}}\}$ of $[\mathbf{H}_{m_{\text{opt}}}]$, we have the estimate $d^2_{N_d}(m_{\text{opt}}) \simeq (1/n_{\text{MC}}) \sum_{\ell=1}^{n_{\text{MC}}} \{\|[\boldsymbol{\eta}^\ell_{\text{ar}}] - [\eta_d]\|^2\}/\|[\eta_d]\|^2$.

(v) Generation of learned realizations $\{\boldsymbol{\eta}^{\ell'}_{\text{ar}}, \ell' = 1, \ldots, N_{\text{ar}}\}$ of random vector $\boldsymbol{H}$. The generation of learned realizations $[z^1_{\text{ar}}], \ldots, [z^{n_{\text{MC}}}_{\text{ar}}]$ of random matrix $[\mathbf{Z}_{m_{\text{opt}}}]$ is carried out by using the MCMC generator detailed in [103], which is based on a reduced-order Itô stochastic differential equation (ISDE) that is constructed as the projection on the ROB of the ISDE related to a dissipative Hamiltonian dynamical system for which the invariant measure is the pdf of random matrix $[\mathbf{H}]$ constructed with the Gaussian kernel-density estimation method and $[\eta_d]$. Let $\{([\mathcal{Z}(t)], [\mathcal{Y}(t)]), t \in \mathbb{R}^+\}$ be the unique asymptotic (for $t \to +\infty$) stationary diffusion stochastic process with values in $\mathbb{M}_{\nu,m_{\text{opt}}} \times \mathbb{M}_{\nu,m_{\text{opt}}}$, of the following reduced-order ISDE (stochastic nonlinear second-order dissipative Hamiltonian dynamical system), for $t > 0$,

$$\begin{aligned} d[\mathcal{Z}(t)] &= [\mathcal{Y}(t)]\, dt \,, \\ d[\mathcal{Y}(t)] &= [\mathcal{L}([\mathcal{Z}(t)])]\, dt - \frac{1}{2} f_0\, [\mathcal{Y}(t)]\, dt \\ &\quad + \sqrt{f_0}\, [d^\nu \boldsymbol{W}^{\text{wien}}(t)] \,, \end{aligned}$$

with $[\mathcal{Z}(0)] = [\eta_d]\,[a]$ and $[\mathcal{Y}(0)] = [\boldsymbol{\mathcal{N}}]\,[a]$, in which

$$[a] = [g_{m_{\text{opt}}}]\, ([g_{m_{\text{opt}}}]^T\, [g_{m_{\text{opt}}}])^{-1} \in \mathbb{M}_{N_d,m_o pt} \,.$$

(1) $[\mathcal{L}([\mathcal{Z}(t)])] = [L([\mathcal{Z}(t)]\,[g_{m_{\text{opt}}}]^T)]\,[a]$ is a random matrix with values in $\mathbb{M}_{\nu,m_{\text{opt}}}$. For all $[u] = [\mathbf{u}^1 \ldots \mathbf{u}^{N_d}]$ in $\mathbb{M}_{\nu,N_d}$ with $\mathbf{u}^j = (u^j_1, \ldots, u^j_\nu)$ in $\mathbb{R}^\nu$, the matrix $[L([u])]$ in $\mathbb{M}_{\nu,N_d}$ is defined, for all $k = 1, \ldots, \nu$ and for all $j = 1, \ldots, N_d$, by

$$[L([u])]_{kj} = \frac{1}{p(\mathbf{u}^j)}\, \{\boldsymbol{\nabla}_{\mathbf{u}^j}\, p(\mathbf{u}^j)\}_k \,, \tag{76}$$

$$p(\mathbf{u}^j) = \frac{1}{N_d} \sum_{j'=1}^{N_d} \exp\{-\frac{1}{2\widehat{s_\nu}^2} \|\frac{\widehat{s_\nu}}{s_\nu} \boldsymbol{\eta}^{j'} - \mathbf{u}^j\|^2\} \,,$$

$$\begin{aligned} \boldsymbol{\nabla}_{\mathbf{u}^j}\, p(\mathbf{u}^j) = &\frac{1}{\widehat{s_\nu}^2\, N_d} \sum_{j'=1}^{N_d} (\frac{\widehat{s_\nu}}{s_\nu} \boldsymbol{\eta}^{j'} - \mathbf{u}^j) \\ &\times \exp\{-\frac{1}{2\widehat{s_\nu}^2} \|\frac{\widehat{s_\nu}}{s_\nu} \boldsymbol{\eta}^{j'} - \mathbf{u}^j\|^2\} \,, \end{aligned}$$

in which $\widehat{s_\nu}$ is the modified Silverman bandwidth s_ν, which has been introduced in [120],

$$\widehat{s_\nu} = \frac{s_\nu}{\sqrt{s^2_\nu + \frac{N_d - 1}{N_d}}} \quad , \quad s_\nu = \left\{\frac{4}{N_d(2 + \nu)}\right\}^{1/(\nu+4)} \,.$$

(2) $[\boldsymbol{\mathcal{W}}^{\text{wien}}(t)] = [\mathbb{W}^{\text{wien}}(t)]\,[a]$ where $\{[\mathbb{W}^{\text{wien}}(t)], t \in \mathbb{R}^+\}$ is the $\mathbb{M}_{\nu,N_d}$-valued normalized Wiener process.
(3) $[\boldsymbol{\mathcal{N}}]$ is the $\mathbb{M}_{\nu,N_d}$-valued normalized Gaussian random matrix that is independent of process $[\mathbb{W}^{\text{wien}}]$.
(4) The free parameter f_0, such that $0 < f_0 < 4/\widehat{s_\nu}$, allows the dissipation term of the nonlinear second-order dynamical system (dissipative Hamiltonian system) to be controlled in order to kill the transient part induced by the initial conditions. A common value is $f_0 = 4$ (note that $\widehat{s_\nu} < 1$).
(5) We then have $[\mathbf{Z}_{m_{\text{opt}}}] = \lim_{t\to+\infty}[\mathcal{Z}(t)]$ in probability distribution. The Störmer-Verlet scheme is used for solving the reduced-order ISDE, which allows for generating the learned realizations, $[z_{\text{ar}}^1], \ldots, [z_{\text{ar}}^{n_{\text{MC}}}]$, and then, generating the learned realizations $[\eta_{\text{ar}}^1], \ldots, [\eta_{\text{ar}}^{n_{\text{MC}}}]$ such that $[\eta_{\text{ar}}^\ell] = [z_{\text{ar}}^\ell]\,[g_{m_{\text{opt}}}]^T$.
(6) The learned realizations $\{\mathbf{x}_{\text{ar}}^{\ell'}, \ell' = 1, \ldots, N_{\text{ar}}\}$ of random vector $\mathbf{X}$ are then calculated (see Eq. (71)) by $\mathbf{x}_{\text{ar}}^{\ell'} = \underline{\mathbf{x}} + [\varphi]\,[\mu]^{1/2}\,\boldsymbol{\eta}_{\text{ar}}^{\ell'}$.

(vi) Constraints on the second-order moments of the components of $\boldsymbol{H}$ if loss of normalization occurs. In general, the mean value of $\mathbf{H}$ estimated using the N_{ar} learned realizations $\{\boldsymbol{\eta}_{\text{ar}}^{\ell'}, \ell' = 1, \ldots, N_{\text{ar}}\}$, is sufficiently close to zero. Likewise, the estimate of the covariance matrix of $\mathbf{H}$, which must be the identity matrix, is sufficiently close to a diagonal matrix. However, sometimes the diagonal entries of the estimated covariance matrix can be lower than 1 (for instance 0.8). Such a case is application-dependent. Normalization can be recovered by imposing constraints

$$\{E\{(H_k)^2\} = 1, k = 1, \ldots, \nu\}\,,$$

in the algorithm presented in paragraph (v). For that, we use the method and the iterative algorithm presented in [105] (that is based on Sections 5.5 and 5.6 of [106]). The constraints are imposed by using the Kullback-Leibler minimum cross-entropy principle. The resulting optimization problem is formulated using a Lagrange multiplier $\mathbf{v} = (v_1, \ldots, v_\nu)$ associated with the constraints. The optimal solution of the Lagrange multiplier is computed using an efficient iterative algorithm. At each iteration, the MCMC generator detailed in paragraph (v) is used. The constraints are rewritten as

$$E\{\mathbf{h}(\mathbf{H})\} = \mathbf{b}\,,$$

in which the function $\mathbf{h} = (h_1, \ldots, h_\nu)$ and the vector $\mathbf{b} = (b_1, \ldots, b_\nu)$ are such that $h_k(\mathbf{H}) = (H_k)^2$ and $b_k = 1$ for k in $\{1, \ldots, \nu\}$. To take into account the constraints in the algorithm of paragraph (v), Eq. (76) is replaced by the following one,

$$[L_{\mathbf{v}}([u])]_{kj} = \frac{1}{p(\mathbf{u}^j)}\,\{\boldsymbol{\nabla}_{\mathbf{u}^j}\,p(\mathbf{u}^j)\}_k - 2\,v_k u_k^j\,.$$

The iteration algorithm for computing $\mathbf{v}^{i+1}$ as a function of $\mathbf{v}^i$ is the following,

$$\begin{aligned}\mathbf{v}^{i+1} &= \mathbf{v}^i - \alpha_i[\Gamma''(\mathbf{v}^i)]^{-1}\,\boldsymbol{\Gamma}'(\mathbf{v}^i) \quad , \quad i \geq 0\,,\\ \mathbf{v}^0 &= \mathbf{0}_\nu\,,\end{aligned} \tag{77}$$

in which $\boldsymbol{\Gamma}'(\mathbf{v}^i) = \mathbf{b} - E\{\mathbf{h}(\mathbf{H}_{\mathbf{v}^i})\}$ and $[\Gamma''(\mathbf{v}^i)] = [\text{cov}\{\mathbf{h}(\mathbf{H}_{\mathbf{v}^i})\}]$ (the covariance matrix), and where α_i is a relaxation function (less than 1) that is introduced for controlling the convergence as a function of iteration number i. For given $i_2 \geq 2$, for given β_1 and β_2 such that $0 < \beta_1 < \beta_2 \leq 1$, α_i can be defined by:

- for $i \leq i_2$, $\alpha_i = \beta_1 + (\beta_2 - \beta_1)(i-1)/(i_2 - 1)$;
- for $i > i_2$, $\alpha_i = \beta_2$.

The convergence of the iteration algorithm is controlled by the error function $i \mapsto \text{err}(i)$ defined by

$$\text{err}(i) = \|\mathbf{b} - E\{\mathbf{h}(\mathbf{H}_{\mathbf{v}^i})\}\|/\|\mathbf{b}\| \,. \tag{78}$$

At each iteration i, $E\{\mathbf{h}(\mathbf{H}_{\mathbf{v}^i})\}$ and $[\text{cov}\{\mathbf{h}(\mathbf{H}_{\mathbf{v}^i})\}]$ are estimated by using the N_{ar} learned realizations of $\mathbf{H}_{m_{\text{opt}}}(\mathbf{v}^i)$ obtained by reshaping the learned realizations.

A.2. Values of the PLoM parameters and results for $N_d = 75$

In order to limit the developments and the number of figures, we only present the case $N_d = 75$. The values of the PLoM parameters and the results are similar for the other values of N_d.

(i) PCA of random vector $\mathbf{X} = (Q, \mathbf{W})$. We have $n_q = 1$ and $n_w = 12$. Consequently, $\mathbf{X}$ is a $\mathbb{R}^n$-valued random variable with $n = 1 + 12 = 13$. The PCA of $\mathbf{X}$ is constructed using the training set $\mathcal{D}_d$ defined by Eq. (68), with a relative tolerance $\varepsilon_{\text{PCA}} = 10^{-6}$. Using Eq. (72) yields $\nu = n = 13$ (so there is no statistical reduction).

(ii) Computation of the diffusion-maps basis. The graph of function $\varepsilon_{\text{DM}} \mapsto \text{Jump}(\varepsilon_{\text{DM}})$ defined by Eq. (74) is shown in Fig. 35 and allows for identifying the optimal value $\varepsilon_{\text{opt}} = 19.6$ of ε_{DM}. The function $\alpha \mapsto \lambda_\alpha(\varepsilon_{\text{opt}})$ of the eigenvalues of the transition matrix for $\varepsilon_{\text{DM}} = \varepsilon_{\text{opt}}$ is shown in Fig. 36 and shows that the optimal value m_{opt} of m is 14. The diffusion-maps basis is made up of the columns of matrix $[g_{m_{\text{opt}}}] \in \mathbb{M}_{\nu, m_{\text{opt}}}$.

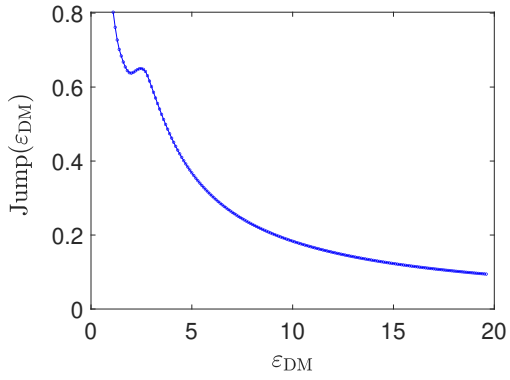

Figure 35: For $N_d = 75$, graph of function $\varepsilon_{\text{DM}} \mapsto \text{Jump}(\varepsilon_{\text{DM}})$ yielding the optimal value $\varepsilon_{\text{opt}} = 19.6$ of ε_{DM}.

(iii) Values of the parameters that control the integration scheme of the reduced-order Itô stochastic differential equation. The dissipation coefficient is $f_0 = 4$ and the integration step is $\Delta r = 0.018399$. The number of realizations of random matrix $[\mathbf{H}]$ with values in $\mathbb{M}_{\nu, N_d}$ is $n_{\text{MC}} = 133\,400$ yielding $N_{\text{ar}} \simeq 10^7$ realizations for the $\mathbb{R}^\nu$-valued random variable $\mathbf{H}$.

(iv) Constraints. The constraints $\{E\{H_k^2\} = 1, k = 1, \ldots, \nu\}$ are applied for generating the N_{ar} realizations $\{\boldsymbol{\eta}_{\text{ar}}^{\ell'}, \ell' = 1, \ldots, N_{\text{ar}}\}$ of random vector $\mathbf{H}$. The parameters of the relaxation function are $\beta_1 = 0.01$, $\beta_2 = 0.2$, and $i_2 = 20$. The graph of the error function $i \mapsto \text{err}(i)$ defined by Eq. (78) is shown in Fig. 37. The convergence is obtained at iteration $i = 45$ for which

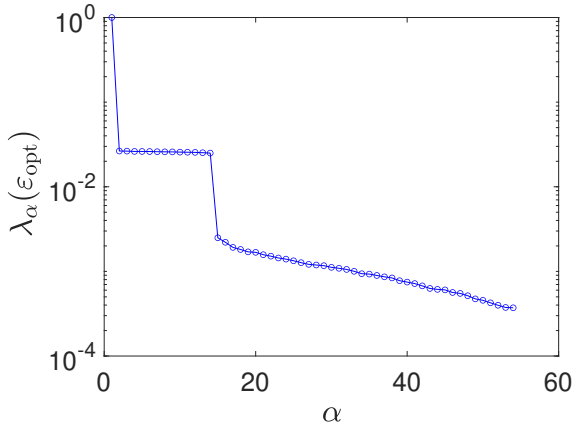

Figure 36: For $N_d = 75$, graph of function $\alpha \mapsto \lambda_\alpha(\varepsilon_{\rm opt})$.

$\text{err}(45) = 4.1 \times 10^{-3}$. Fig. 38 shows the estimation of $\{E\{H_k^2\}$ for $k = 1, \ldots, \nu$ performed with $\{\boldsymbol{\eta}_{\rm ar}^{\ell'}, \ell' = 1, \ldots, N_{\rm ar}\}$ generated in taking into account the constraints. It can be seen that the constraints are satisfied because $E\{H_k^2\} \simeq 1$ for all k.

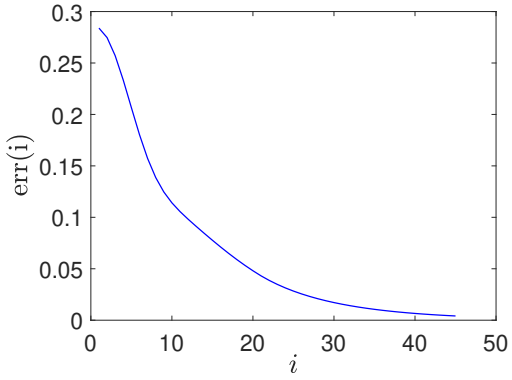

Figure 37: For $N_d = 75$, error function $\text{err}(i)$ as a function of iteration number i of the iterative algorithm for the computation of the Lagrange multipliers.

(v) Quantifying the concentration of the probability measure of random matrix $[\boldsymbol{H}_{m_{\rm opt}}]$. The use of Eq. (75) yields $d^2_{N_d}(m_{\rm opt}) = 0.073 \ll 2$, which shows the concentration of the measure is kept.

References

[1] D. Whitehead, Effects of mistuning on the vibration of turbomachine blades induced by wakes, Journal of Mechanical Engineering Science 8 (1) (1966) 15–21. doi:10.1243/JMES_JOUR_1966_008_004_02.

[2] D. Ewins, The effects of detuning upon the forced vibrations of bladed disks, Journal of Sound and Vibration 9 (1) (1969) 65–69. doi:10.1016/0022-460X(69)90264-8.

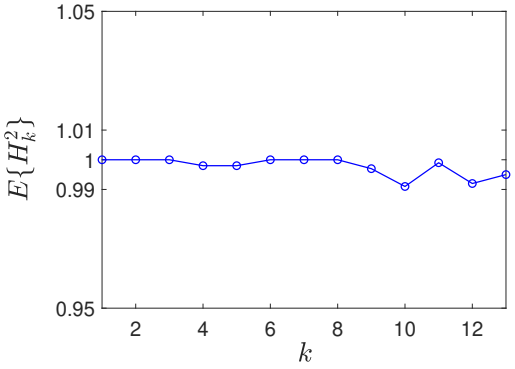

Figure 38: For $N_d = 75$, estimation of $\{E\{H_k^2\}$ for $k = 1, \ldots, \nu$ performed with $\{\boldsymbol{\eta}_{\rm ar}^{\ell}, \ell = 1, \ldots, N_{\rm ar}\}$ generated in taking into account the constraints.

[3] S. Wei, C. Pierre, Localization phenomena in mistuned assemblies for cyclic symmetry - part ii: forced vibrations, ASME Journal of Vibration, Acoustics, Stress, and Reliability in Design 110 (4) (1988) 439–449. doi:10.1115/1.3269548.

[4] R. Bladh, M. Castanier, C. Pierre, Component-mode-based reduced order modeling techniques for mistuned bladed disks. part 1: theoretical models, ASME Journal of Engineering for Gas Turbines and Power 123 (1) (2001) 89–99. doi:10.1115/1.1338947.

[5] M.-T. Yang, J. Griffin, A reduced-order model of mistuning using a subset of nominal modes, ASME Journal of Engineering for Gas Turbines and Power 123 (3) (2001) 893–900. doi:10.1115/1.1385197.

[6] E. Capiez-Lernout, C. Soize, Nonparametric modeling of random uncertainties for dynamic response of mistuned bladed-disks., ASME Journal of Engineering for Gas Turbines and Power 126 (3) (2004) 610–618. doi:10.1115/1.1760527.

[7] A. Sinha, Reduced-order model of a bladed rotor with geometric mistuning, ASME Journal of Turbomachinery 131 (3) (2009) 031007. doi:10.1115/1.2987237.

[8] M. Mbaye, C. Soize, J.-P. Ousty, A reduced-order model of detuned cyclic dynamical systems with geometric modifications using a basis of cyclic modes, ASME Journal of Engineering for Gas Turbines and Power 132 (11) (2010) 112502–1–9. doi:10.1115/1.4000805.

[9] P. Vargiu, C. Firrone, S. Zucca, M. Gola, A reduced order model based on sector mistuning for the dynamic analysis of mistuned bladed disks, International Journal of Mechanical Sciences 53 (8) (2011) 639–646. doi:10.1016/j.ijmecsci.2011.05.010.

[10] A. Madden, B. I. Epureanu, S. Filippi, Reduced-order modeling approach for blisks with large mass, stiffness, and geometric mistuning, AIAA Journal 50 (2) (2012) 366–374. doi:10.2514/1.J051140.

[11] L. Schwerdt, L. Panning-von Scheidt, J. Wallaschek, A model reduction method for bladed disks with large geometric mistuning using a partially reduced intermediate system model, ASME Journal of Engineering for Gas Turbines and Power 143 (7). doi:10.1115/1.4049357.

[12] D. Laxalde, F. Thouverez, Complex non-linear modal analysis for mechanical systems: Application to turbomachinery bladings with friction interfaces, Journal of Sound and Vibration 322 (4) (2009) 1009–1025. doi:10.1016/j.jsv.2008.11.044.

[13] M. Krack, L. Panning-von Scheidt, J. Wallaschek, C. Siewert, A. Hartung, Reduced order modeling based on complex nonlinear modal analysis and its application to bladed disks with shroud contact, ASME Journal of Engineering for Gas Turbines and Power 135 (10). doi:10.1115/1.4025002.

[14] A. Batailly, M. Legrand, C. Pierre, Full three-dimensional rotor/stator interaction simulations in aircraft engines with time-dependent angular speed, ASME Journal of Engineering for Gas Turbines and Power 139 (3) (2017) 031202. doi:10.1115/1.4034503.

[15] L. Pesaresi, L. Salles, A. Jones, J. Green, C. Schwingshackl, Modelling the nonlinear behaviour of an underplatform damper test rig for turbine applications, Mechanical Systems and Signal Processing 85 (2017) 662–679. doi:10.1016/j.ymssp.2016.09.007.

[16] C. Joannin, F. Thouverez, B. Chouvion, Reduced-order modelling using nonlinear modes and triple nonlinear modal synthesis, Computers and Structures 203 (2018) 18–33. doi:10.1016/j.compstruc.2018.05.005.

[17] E. Piollet, F. Nyssen, A. Batailly, Blade/casing rubbing interactions in aircraft engines: Numerical benchmark and design guidelines based on NASA rotor 37, Journal of Sound and Vibration 460 (2019) 114878. doi:10.1016/j.jsv.2019.114878.
[18] S. Quaegebeur, B. Chouvion, F. Thouverez, Nonlinear dynamic analysis of three-dimensional bladed-disks with frictional contact interfaces based on cyclic reduction strategies, International Journal of Solids and Structures 236-237 (2022) 111277. doi:10.1016/j.ijsolstr.2021.111277.
[19] S. Mehrdad Pourkiaee, S. Zucca, A reduced order model for nonlinear dynamics of mistuned bladed disks with shroud friction contacts, ASME Journal of Engineering for Gas Turbines and Power 141 (1). doi:10.1115/1.4041653.
[20] A. Koscso, E. Petrov, Sensitivity and forced response analysis of anisotropy-mistuned bladed disks with nonlinear contact interfaces, ASME Journal of Engineering for Gas Turbines and Power 141 (10). doi:10.1115/1.4044883.
[21] J. Chen, C. Zang, B. Zhou, E. P. Petrov, Analysis of nonlinear modal damping due to friction at blade roots in mistuned bladed disks, ASME Journal of Engineering for Gas Turbines and Power 143 (3). doi:10.1115/1.4049860.
[22] J. Joachim, F. Nyssen, A. Batailly, Numerical investigation of a mistuned academic bladed disk dynamics with blade/casing contact, Journal of Engineering for Gas Turbines and Power 143 (4). doi:10.1115/1.4047780.
[23] F. Nyssen, A. Batailly, Investigation on the robustness of rotor/stator contact interactions with respect to small mistuning, ASME Journal of Engineering for Gas Turbines and Power 143 (12). doi:10.1115/1.4051957.
[24] S. Quaegebeur, B. Chouvion, F. Thouverez, Impact of mistuned underplatform dampers on the nonlinear vibration of bladed disks, ASME Journal of Engineering for Gas Turbines and Power 143 (12). doi:10.1115/1.4051868.
[25] S. M. Pourkiaee, S. Zucca, R. G. Parker, Relative cyclic component mode synthesis: A reduced order modeling approach for mistuned bladed disks with friction interfaces, Mechanical Systems and Signal Processing 163 (2022) 108197. doi:10.1016/j.ymssp.2021.108197.
[26] A. A. Muravyov, S. Rizzi, Determination of nonlinear stiffness with application to random vibration of geometrically nonlinear structures, Computers & Structures 81 (15) (2003) 1513–1523. doi:10.1016/S0045-7949(03)00145-7.
[27] M. P. Mignolet, A. Przekop, S. A. Rizzi, S. M. Spottswood, A review of indirect/non-intrusive reduced order modeling of nonlinear geometric structures, Journal of Sound and Vibration 332 (10) (2013) 2437–2460. doi:10.1016/j.jsv.2012.10.017.
[28] K. Kim, A. G. Radu, X. Wang, M. P. Mignolet, Nonlinear reduced order modeling of isotropic and functionally graded plates, International Journal of Non-Linear Mechanics 49 (2013) 100–110. doi:10.1016/j.ijnonlinmec.2012.07.008.
[29] X. Wang, G. P. Phlipot, R. A. Perez, M. P. Mignolet, Locally enhanced reduced order modeling for the nonlinear geometric response of structures with defects, International Journal of Non-Linear Mechanics 101 (2018) 1–7. doi:10.1016/j.ijnonlinmec.2018.01.007.
[30] X. Wang, M. P. Mignolet, C. Soize, Structural uncertainty modeling for nonlinear geometric response using nonintrusive reduced order models, Probabilistic Engineering Mechanics 60 (2020) 103033. doi:10.1016/j.probengmech.2020.103033.
[31] X. Q. Wang, V. Khanna, K. Kim, M. P. Mignolet, Nonlinear reduced-order modeling of flat cantilevered structures: Identification challenges and remedies, Journal of Aerospace Engineering 34 (6) (2021) 04021085. doi:10.1061/(ASCE)AS.1943-5525.0001324.
[32] A. Vakakis, Dynamics of a nonlinear periodic structure with cyclic symmetry, Acta Mechanica 95 (1-4) (1992) 197–226. doi:10.1007/BF01170813.
[33] A. Grolet, F. Thouverez, Computing multiple periodic solutions of nonlinear vibration problems using the harmonic balance method and groebner bases, Mechanical Systems and Signal Processing 52 (2015) 529–547. doi:10.1016/j.ymssp.2014.07.015.
[34] A. Martin, F. Thouverez, Dynamic analysis and reduction of a cyclic symmetric system subjected to geometric nonlinearities, Journal of Engineering for Gas Turbines and Power 141 (4). doi:10.1115/1.4041001.
[35] E. Delhez, F. Nyssen, J.-C. Golinval, A. Batailly, Reduced order modeling of blades with geometric nonlinearities and contact interactions, Journal of Sound and Vibrationdoi:10.1016/j.jsv.2021.116037.
[36] E. Capiez-Lernout, C. Soize, M. Mbaye, Mistuning analysis and uncertainty quantification of an industrial bladed disk with geometrical nonlinearity, Journal of Sound and Vibration 356 (10) (2015) 124–143. doi:10.1016/j.jsv.2015.07.006.
[37] M. Castanier, C. Pierre, Investigation of the combined effects of intentional and random mistuning on the forced response of bladed disks, in: Proceedings 34th AIAA/ASME/SAE/ASEE Joint Propulsion Conference and Exhibit, Cleveland OH ,July, 13-15 1998, 1998. doi:10.2514/6.1998-3720.
[38] M. Castanier, C. Pierre, Using intentional mistuning in the design of turbomachinery rotors, AIAA Journal 40 (10) (2002) 2077–2086. doi:10.2514/2.1542.
[39] B.-K. Choi, J. Lentz, A. J. Rivas-Guerra, M. P. Mignolet, Optimization of intentional mistuning patterns for the reduction of the forced response effects of unintentional mistuning: formulation and assessment, ASME Journal

of Engineering for Gas Turbines and Power 125 (1) (2003) 131–140. doi:10.1115/1.1498270.
[40] M. Mbaye, C. Soize, J.-P. Ousty, E. Capiez-Lernout, Robust analysis of design in vibration of turbomachines, ASME Journal of Turbomachinery 135 (2) (2013) 021008. doi:10.1115/1.4007442.
[41] Y. Han, R. Murthy, M. Mignolet, J. Lentz, Optimization of intentional mistuning patterns for the mitigation of the effects of random mistuning, ASME Journal of Engineering for Gas Turbines and Power 136 (06) (2014) 062505. doi:10.1115/1.4026141.
[42] B. Beirow, F. Figaschewsky, A. Kühhorn, A. Bornhorn, Vibration analysis of an axial turbine blisk with optimized intentional mistuning pattern, Journal of Sound and Vibration 442 (2019) 11–27. doi:10.1016/j.jsv.2018.10.064.
[43] A. Lupini, J. Shim, S. Callan, B. I. Epureanu, Mistuning identification technique based on blisk detuning, AIAA Journal 59 (8) (2021) 3087–3095. doi:10.2514/1.J060209.
[44] A. Nakos, B. Beirow, A. Zobel, Mistuning and damping of a radial turbine wheel. part 1: fundamental analyses and design of intentional mistuning pattern, Journal of Engineering for Gas Turbines and Power 144 (2). doi:10.1115/1.4052201.
[45] J. J. Sanchez-Alvarez, C. Martel, Key action mechanisms of intentional mistuning, Applied Sciences 11 (12). doi:10.3390/app11125650.
[46] B. Beirow, M. Golze, F. Popig, Vibration reduction of a steam turbine wheel by means of intentional mistuning, in: In: Beran J., Bilek M., Vaclavik M., Zabka P. (eds) Advances in Mechanism Design III. TMM 2020. Mechanisms and Machine Science, Vol. 85, Springer,Cham, 2022. doi:10.1007/978-3-030-83594-1_8.
[47] A. Picou, E. Capiez-Lernout, C. Soize, M. Mbaye, Robust dynamic analysis of detuned-mistuned rotating bladed disks with geometric nonlinearities, Computational Mechanics 65 (3) (2020) 711–730. doi:10.1007/s00466-019-01790-4.
[48] C. Soize, Stochastic Models of Uncertainties in Computational Mechanics, Lecture Notes in Engineering Mechanics 2, American Society of Civil Engineers (ASCE), 2012. doi:10.1061/9780784412237.
[49] C. Soize, Uncertainty Quantification, Springer, New York, 2017. doi:10.1007/978-3-319-54339-0.
[50] C. Desceliers, C. Soize, Non-linear viscoelastodynamic equations of three-dimensional rotating structures in finite displacement and finite element discretization, International Journal of Non-Linear Mechanics 39 (3) (2004) 343–368. doi:10.1016/S0020-7462(02)00191-9.
[51] M.-P. Mignolet, C. Soize, Stochastic reduced order models for uncertain geometrically nonlinear dynamical systems, Computer Methods in Applied Mechanics and Engineering 197 (45-48) (2008) 3951–3963. doi:10.1016/j.cma.2008.03.032.
[52] E. Capiez-Lernout, C. Soize, M. Mignolet, Computational stochastic statics of an uncertain curved structure with geometrical nonlinearity in three-dimensional elasticity, Computational Mechanics 49 (1) (2012) 87–97. doi:10.1007/s00466-011-0629-y.
[53] E. Capiez-Lernout, C. Soize, An improvement of the uncertainty quantification in computational structural dynamics with nonlinear geometrical effects, International Journal for Uncertainty Quantification 7 (1) (2017) 83–98. doi:10.1615/Int.J.UncertaintyQuantification.2016019141.
[54] C. Soize, A nonparametric model of random uncertainties for reduced matrix models in structural dynamics, Probabilistic Engineering Mechanics 15 (3) (2000) 277–294. doi:10.1016/S0266-8920(99)00028-4.
[55] R. De Borst, M. Crisfield, J. Remmers, C. V. Verhoosel, Non-Linear Finite Element Analysis of Solids and Structures, Second Edition, Wiley, 2012. doi:10.1002/9781118375938.
[56] M. Crisfield, A fast incremental/iterative solution procedure that handles "snap-through", Computers and Structures 13 (1-3) (1981) 55–62. doi:10.1016/0045-7949(81)90108-5.
[57] E. Ramm, Strategies for tracing the nonlinear response near limit points, in: B. K. Wunderlich W., Stein E. (Ed.), Nonlinear Finite Element Analysis in Structural Mechanics, Springer, Berlin, Heidelberg, 1981, pp. 63–89. doi:10.1007/978-3-642-81589-8_5.
[58] E. Riks, The application of Newton's method to the problem of elastic stability, Journal of Applied Mechanics 39 (4) (1972) 1060–1065. doi:10.1115/1.3422829.
[59] R. Bladh, M. Castanier, C. Pierre, Component-mode-based reduced order modeling techniques for mistuned bladed disks. part 2: application, ASME Journal of Engineering for Gas Turbines and Power 123 (1) (2001) 100–108. doi:10.1115/1.1338948.
[60] Q. Akkaoui, E. Capiez-Lernout, C. Soize, R. Ohayon, Revisiting the experiment of a free-surface resonance of a liquid in a vibration tank using a nonlinear fluid-structure computational model, Journal of Fluids and Structures 85 (2019) 149–164. doi:10.1016/j.jfluidstructs.2019.01.005.
[61] C. H. Papadimitriou, K. Steiglitz, Combinatorial Optimization: Algorithms and Complexity, Dover Publications, Inc., 1998.
[62] J. Lee, A First Course in Combinatorial Optimization, Vol. 36, Cambridge University Press, 2004.
[63] W. J. Cook, W. Cunningham, W. Pulleyblank, A. Schrijver, Combinatorial optimization, Oberwolfach Reports 5 (4) (2009) 2875–2942.
[64] H. Karloff, Linear Programming, Springer Science & Business Media, 2008.

[65] J. Renegar, A polynomial-time algorithm, based on Newton's method, for linear programming, Mathematical Programming 40 (1) (1988) 59–93. doi:10.1007/BF01580724.
[66] H. P. Williams, Integer programming, in: Logic and Integer Programming, Springer, 2009, pp. 25–70.
[67] R. Diestel, Graph Theory, Springer, Berlin, 2017.
[68] H. A. Taha, Operations Research: an Introduction, 10th Edition, Vol. 790, Pearson, Prentice Hall Upper Saddle River, NJ, USA, 2011.
[69] S. Arora, B. Barak, Computational Complexity: a Modern Approach, Cambridge University Press, Cambridge, 2009.
[70] M. J. Brusco, S. Stahl, et al., Branch-and-Bound Applications in Combinatorial Data Analysis, Vol. 2, Springer, Berlin, 2005.
[71] J. E. Mitchell, Branch-and-cut algorithms for combinatorial optimization problems, Handbook of Applied Optimization 1 (2002) 65–77.
[72] M. Gendreau, J.-Y. Potvin, Tabu search, in: Search Methodologies, Springer, 2005, pp. 165–186.
[73] H. AbouEisha, T. Amin, I. Chikalov, S. Hussain, M. Moshkov, Extensions of Dynamic Programming for Combinatorial Optimization and Data Mining, Springer, 2019.
[74] R. Ghanem, D. Higdon, H. Owhadi, Handbook of Uncertainty Quantification, Vol. 1 to 3, Springer, Cham, Switzerland, 2017. doi:10.1007/978-3-319-12385-1.
[75] R. Zimmermann, Gradient-enhanced surrogate modeling based on proper orthogonal decomposition, Journal of Computational and Applied Mathematics 237 (1) (2013) 403–418. doi:10.1016/j.cam.2012.06.010.
[76] P. G. Constantine, E. Dow, Q. Wang, Active subspace methods in theory and practice: applications to kriging surfaces, SIAM Journal on Scientific Computing 36 (4) (2014) A1500–A1524. doi:10.1137/130916138.
[77] C. Soize, R. Ghanem, Polynomial chaos representation of databases on manifolds, Journal of Computational Physics 335 (2017) 201–221. doi:10.1016/j.jcp.2017.01.031.
[78] A. Bhosekar, M. Ierapetritou, Advances in surrogate based modeling, feasibility analysis, and optimization: A review, Computers & Chemical Engineering 108 (2018) 250–267. doi:10.1016/j.compchemeng.2017.09.017.
[79] I. Kalogeris, V. Papadopoulos, Diffusion maps-based surrogate modeling: An alternative machine learning approach, International Journal for Numerical Methods in Engineering 121 (4) (2020) 602–620. doi:10.1002/nme.6236.
[80] M. Mignolet, C. Soize, Compressed principal component analysis of non-gaussian vectors, SIAM/ASA Journal on Uncertainty Quantification 8 (4) (2020) 1261–1286. doi:10.1137/20M1322029.
[81] D. Ryckelynck, A priori hyperreduction method: an adaptive approach, Journal of Computational Physics 202 (1) (2005) 346–366. doi:10.1016/j.jcp.2004.07.015.
[82] M. A. Grepl, Y. Maday, N. C. Nguyen, A. T. Patera, Efficient reduced-basis treatment of nonaffine and nonlinear partial differential equations, ESAIM: Mathematical Modelling and Numerical Analysis 41 (3) (2007) 575–605. doi:10.1051/m2an:2007031.
[83] K. Carlberg, C. Farhat, A low-cost, goal-oriented compact proper orthogonal decomposition basis for model reduction of static systems, International Journal for Numerical Methods in Engineering 86 (3) (2011) 381–402. doi:10.1002/nme.3074.
[84] D. Amsallem, M. Zahr, Y. Choi, C. Farhat, Design optimization using hyper-reduced-order models, Structural and Multidisciplinary Optimization 51 (4) (2015) 919–940. doi:10.1007/s00158-014-1183-y.
[85] C. Farhat, T. Chapman, P. Avery, Structure-preserving, stability, and accuracy properties of the energy-conserving sampling and weighting method for the hyper reduction of nonlinear finite element dynamic models, International Journal for Numerical Methods in Engineering 102 (5) (2015) 1077–1110. doi:10.1002/nme.4820.
[86] C. Soize, C. Farhat, Probabilistic learning for modeling and quantifying model-form uncertainties in nonlinear computational mechanics, International Journal for Numerical Methods in Engineering 117 (2019) 819–843. doi:10.1002/nme.5980.
[87] R. Swischuk, L. Mainini, B. Peherstorfer, K. Willcox, Projection-based model reduction: Formulations for physics-based machine learning, Computers & Fluids 179 (2019) 704–717. doi:10.1016/j.compfluid.2018.07.021.
[88] X. Wang, M. Mignolet, Discussion on a non-intrusive model-order reduction of geometrically nonlinear structural dynamics using modal derivatives, Mechanical Systems and Signal Processing 159 (2021) 107638. doi:/10.1016/j.ymssp.2021.107638.
[89] D. Jones, M. Schonlau, W. Welch, Efficient global optimization of expensive black-box functions, Journal of Global Optimization 13 (4) (1998) 455–492. doi:10.1023/A:1008306431147.
[90] X. Du, W. Chen, Sequential optimization and reliability assessment method for efficient probabilistic design, ASME Journal of Mechanical Design 126 (2) (2004) 225–233. doi:10.1115/1.1649968.
[91] N. Queipo, R. Haftka, W. Shyy, T. Goel, R. Vaidyanathan, K. Tucker, Surrogate-based analysis and optimization, Progress in Aerospace Science 41 (1) (2005) 1–28. doi:10.1016/j.paerosci.2005.02.001.
[92] R. Byrd, G. Chin, W. Neveitt, J. Nocedal, On the use of stochastic Hessian information in optimization methods for machine learning, SIAM Journal of Optimization 21 (3) (2011) 977–995. doi:10.1137/10079923X.

[93] R. Ghanem, C. Soize, Probabilistic nonconvex constrained optimization with fixed number of function evaluations, International Journal for Numerical Methods in Engineering 113 (4) (2018) 719–741. doi:10.1002/nme.5632.
[94] J. Schmidhuber, Deep learning in neural networks: An overview, Neural networks 61 (2015) 85–117. doi:10.1016/j.neunet.2014.09.003.
[95] A. Talwalkar, S. Kumar, H. Rowley, Large-scale manifold learning, in: 2008 IEEE Conference on Computer Vision and Pattern Recognition, IEEE, 2008, pp. 1–8. doi:10.1109/CVPR.2008.4587670.
[96] D. Gorissen, I. Couckuyt, P. Demeester, T. Dhaene, K. Crombecq, A surrogate modeling and adaptive sampling toolbox for computer based design, Journal of Machine Learning Research 11 (68) (2010) 2051–2055.
[97] A. C. Öztireli, M. Alexa, M. Gross, Spectral sampling of manifolds, ACM Transactions on Graphics (TOG) 29 (6) (2010) 1–8. doi:10.1145/1882261.1866190.
[98] Y. Marzouk, T. Moselhy, M. Parno, A. Spantini, Sampling via measure transport: An introduction, Handbook of Uncertainty Quantification (2016) 1–41.
[99] M. D. Parno, Y. M. Marzouk, Transport map accelerated markov chain Monte Carlo, SIAM/ASA Journal on Uncertainty Quantification 6 (2) (2018) 645–682. doi:10.1137/17M1134640.
[100] G. Perrin, C. Soize, N. Ouhbi, Data-driven kernel representations for sampling with an unknown block dependence structure under correlation constraints, Computational Statistics & Data Analysis 119 (2018) 139–154. doi:10.1016/j.csda.2017.10.005.
[101] P. Tsilifis, R. Ghanem, Bayesian adaptation of chaos representations using variational inference and sampling on geodesics, Proceedings of the Royal Society A: Mathematical, Physical and Engineering Sciences 474 (2217) (2018) 20180285. doi:10.1098/rspa.2018.0285.
[102] Y. Kevrekidis, Manifold learning for parameter reduction, Bulletin of the American Physical Society 65. doi:10.1016/j.jcp.2019.04.015.
[103] C. Soize, R. Ghanem, Data-driven probability concentration and sampling on manifold, Journal of Computational Physics 321 (2016) 242–258. doi:10.1016/j.jcp.2016.05.044.
[104] C. Soize, R. Ghanem, Probabilistic learning on manifolds, Foundations of Data Science 2 (3) (2020) 279–307. doi:10.3934/fods.2020013.
[105] C. Soize, R. Ghanem, Probabilistic learning on manifolds (PLoM) with partition, International Journal for Numerical Methods in Engineering 123 (1) (2022) 268–290. doi:10.1002/nme.6856.
[106] C. Soize, R. Ghanem, Physics-constrained non-gaussian probabilistic learning on manifolds, International Journal for Numerical Methods in Engineering 121 (1) (2020) 110–145. doi:10.1002/nme.6202.
[107] C. Soize, R. Ghanem, Probabilistic learning on manifolds constrained by nonlinear partial differential equations for small datasets, Computer Methods in Applied Mechanics and Engineering 380 (2021) 113777. doi:10.1016/j.cma.2021.113777.
[108] C. Soize, R. Ghanem, C. Desceliers, Sampling of bayesian posteriors with a non-gaussian probabilistic learning on manifolds from a small dataset, Statistics and Computing 30 (5) (2020) 1433–1457. doi:10.1007/s11222-020-09954-6.
[109] R. Ghanem, C. Soize, C. Thimmisetty, Optimal well-placement using probabilistic learning, Data-Enabled Discovery and Applications 2 (1) (2018) 4,1–16. doi:10.1007/s41688-017-0014-x.
[110] R. Ghanem, C. Soize, C. Safta, X. Huan, G. Lacaze, J. C. Oefelein, H. N. Najm, Design optimization of a scramjet under uncertainty using probabilistic learning on manifolds, Journal of Computational Physics 399 (2019) 108930. doi:10.1016/j.jcp.2019.108930.
[111] R. Ghanem, C. Soize, L. Mehrez, V. Aitharaju, Probabilistic learning and updating of a digital twin for composite material systems, International Journal for Numerical Methods in Engineering online. doi:10.1002/nme.6430.
[112] M. Arnst, C. Soize, K. Bulthies, Computation of sobol indices in global sensitivity analysis from small data sets by probabilistic learning on manifolds, International Journal for Uncertainty Quantification 11 (2) (2021) 1–23. doi:10.1615/Int.J.UncertaintyQuantification.2020032674.
[113] T. Duong, M. L. Hazelton, Cross-validation bandwidth matrices for multivariate kernel density estimation, Scandinavian Journal of Statistics 32 (3) (2005) 485–506. doi:10.1111/j.1467-9469.2005.00445.x.
[114] T. Duong, A. Cowling, I. Koch, M. Wand, Feature significance for multivariate kernel density estimation, Computational Statistics & Data Analysis 52 (9) (2008) 4225–4242. doi:10.1016/j.csda.2008.02.035.
[115] M. Filippone, G. Sanguinetti, Approximate inference of the bandwidth in multivariate kernel density estimation, Computational Statistics & Data Analysis 55 (12) (2011) 3104–3122. doi:10.1016/j.csda.2011.05.023.
[116] N. Zougab, S. Adjabi, C. C. Kokonendji, Bayesian estimation of adaptive bandwidth matrices in multivariate kernel density estimation, Computational Statistics & Data Analysis 75 (2014) 28–38. doi:10.1016/j.csda.2014.02.002.
[117] A. Bowman, A. Azzalini, Applied Smoothing Techniques for Data Analysis: The Kernel Approach With S-Plus Illustrations, Vol. 18, Oxford University Press, Oxford: Clarendon Press, New York, 1997. doi:10.1007/s001800000033.

[118] R. Coifman, S. Lafon, Diffusion maps, Applied and Computational Harmonic Analysis 21 (1) (2006) 5–30. doi:10.1016/j.acha.2006.04.006.

[119] S. Lafon, A. B. Lee, Diffusion maps and coarse-graining: A unified framework for dimensionality reduction, graph partitioning, and data set parameterization, IEEE transactions on pattern analysis and machine intelligence 28 (9) (2006) 1393–1403. doi:10.1109/TPAMI.2006.184.

[120] C. Soize, Polynomial chaos expansion of a multimodal random vector, SIAM-ASA Journal on Uncertainty Quantification 3 (1) (2015) 34–60. doi:10.1137/140968495.